Faculteit Industriële Ingenieurswetenschappen

master in de industriële wetenschappen: nucleaire technologie

Masterthesis

Developing low-energy Coulomb-excitation techniques for isomer power research

Yannick Ravert

Scriptie ingediend tot het behalen van de graad van master in de industriële wetenschappen: nucleaire technologie, afstudeerrichting nucleair en medisch

PROMOTOR :
Prof. dr. Wouter SCHROEYERS

PROMOTOR :
dr. AJ MITCHELL

Gezamenlijke opleiding UHasselt en KU Leuven

UHASSELT KU LEUVEN

Universiteit Hasselt | Campus Diepenbeek | Faculteit Industriële Ingenieurswetenschappen | Agoralaan Gebouw H - Gebouw B | BE 3590 Diepenbeek

Universiteit Hasselt | Campus Diepenbeek | Agoralaan Gebouw D | BE 3590 Diepenbeek
Universiteit Hasselt | Campus Hasselt | Martelarenlaan 42 | BE 3500 Hasselt

UHASSELT KU LEUVEN

2024
2025

Faculteit Industriële Ingenieurswetenschappen

master in de industriële wetenschappen: nucleaire technologie

Masterthesis

Developing low-energy Coulomb-excitation techniques for isomer power research

Yannick Ravert

Scriptie ingediend tot het behalen van de graad van master in de industriële wetenschappen: nucleaire technologie, afstudeerrichting nucleair en medisch

PROMOTOR :

Prof. dr. Wouter SCHROEYERS

PROMOTOR :

dr. AJ MITCHELL

UHASSELT KU LEUVEN

Preface

Standing at the end of my academic journey, looking back on the road I have walked, I realise the complexity of my study. In the thousand words and many pages, I want to pause and give thanks where due because each chapter is a story of support and collaboration.

Firstly, I want to express gratitude towards my external promoter, Dr. AJ Mitchell from the Australian National University, for allowing me to work on this subject at the ANU facility. Furthermore, his guidance and endless hours of work helped this project towards a feasible goal. My time at ANU has been priceless. I can only be thankful for the opportunities that arose with the exchange to ANU and would highly recommend it.

I also want to thank my internal promoter, Prof. Dr. Wouter Schroeyers. His knowledge and experience have brought tremendous help towards this common goal. My academic journey includes many classes in which he shared his wisdom.

I'm especially grateful to Dr. Ben Coombes, who spent many of his private hours explaining parts of the subject to me. The department does not feel the same without you. Your expertise was invaluable, and I'm appreciative of your support throughout.

A very honorable mention goes to my good friend Luke. Thank you for helping me in this project and making life in Canberra way more enjoyable. A thanks (or cheers) to all the PhD students at the nuclear physics department for giving me such a warm welcome. I sincerely enjoyed all the lunch times at noon sharp. I will cherish the time in spent in Canberra for the rest of my life thanks to you guys.

I want to say thank you to my family and friends for keeping me sane during this tough period. Thank you to my parents for allowing me this opportunity to fulfil a lifetime dream. I could not have done this without your support.

Contents

Preface **1**

Abstract **13**

Abstract in Dutch **15**

1 Introduction **17**

2 Background **21**

2.1 Nuclear Structure 22

2.1.1 Shell model 23

2.2 Collective Excitations 24

2.2.1 Vibrational states 24

2.2.2 Rotational states 25

2.3 Electromagnetic decay 26

2.3.1 γ-transitions 26

2.3.2 Transition rules 27

2.3.3 Transition probability 28

2.4 Nuclear Isomers 29

2.4.1 Isomeric states 29

2.4.2 Isomers types 30

2.4.3 Isomer Energy Storage 33

2.5 Experimental probes of nuclear structure 34

2.5.1 Coulomb Excitation 34

2.5.2 Particle spectroscopy 36

2.6 ^{155}Gd 37

2.6.1 Properties of ^{155}Gd . . . 37
2.6.2 Research on ^{155}Gd . . . 39

3 Instrumentation **41**
3.1 LIon . . . 42
3.2 GEANT4 simulation . . . 44
3.3 Simulation benchmarking . . . 47
3.3.1 Test one . . . 47
3.3.2 Test two . . . 51
3.3.3 Conclusion . . . 54

4 Coulomb-excitation setup **57**
4.1 Particle accelerator . . . 58
4.2 Target . . . 60
4.3 Enge . . . 61
4.4 Signal processing . . . 63
4.5 Coulomb excitations conditions . . . 64
4.5.1 Safe Coulomb excitation energies . . . 64
4.5.2 GOSIA . . . 65
4.5.3 Beam energy and scattering angle . . . 67

5 Results & discussion **71**
5.1 Data collection . . . 72
5.2 Spectra . . . 73
5.2.1 Position wire . . . 73
5.2.2 Scintillator . . . 78
5.2.3 GEANT4 spectra . . . 81
5.3 Yields . . . 83
5.4 Discussion . . . 85
5.4.1 Validation of GEANT4 model . . . 85
5.4.2 Discussion of results . . . 86

6 Conclusions **91**

List of Tables

2.1 Spectroscopic notation of quantum orbitals 23

2.2 Allowed transitions for E and M up to $L = 3$ 28

2.3 Weisskopf units estimates for E1, M1, and E2 transitions 29

2.4 Calculated Weisskopf units estimates for the first two excited levels of ^{155}Gd 38

3.1 The calculation of SRIM for a 70 MeV ^{16}O beam in isobutane with a gas density of 6.8×10^{-4} g/cm^3 47

3.2 The differences in track length between GEANT4 and experimental data . 55

4.1 The natural abundance of the stable gadolinium isotopes, in addition to the composition of the target used in the Coulomb-excitation experiment . . . 60

4.2 The properties of the beam particle and target 66

4.3 A excitation probability of exciting each certain level calculated by GOSIA 68

4.4 chosen energy levels and angles 69

List of Figures

1.1 An image of CAESAR with the HPGe detectors already placed in the BGO holes. There are three additional detectors in the array that are not shown in this image 18

1.2 The spectra generated by [6] with gamma-spectroscopy, a 52 MeV ^{16}O beam incident on a ^{155}Gd target. The red indicates the 46 MeV beam while the blue represents the 52 MeV oxygen-beam. The vertical lines indicate where the scale changes 19

2.1 Nucleon-nucleon potential energy as a function of their separation 22

2.2 The four vibrational modes of nuclei, each mode is a vibration about the spherical equilibrium 25

2.3 A level scheme of ^{164}Er where the excited state are a result from the rotation of the ground state. Energies are displayed in keV 26

2.4 The K-projection of the isomer is the total angular momentum onto the symmetry axis 31

2.5 Level scheme of ^{180}Hf showing the transition from K= 8 to K= 0 31

2.6 Double-hump-back model for shape isomers 32

2.7 Arbitrary level scheme with J_2^+ an isomeric state, by exciting the J_2^+ isomeric state a energy release to the J_0^+ is stimulated 33

2.8 Depiction of the Coulex mechanism between an accelerated beam nucleus and a target nucleus 34

2.9 A level scheme displaying the first levels of ^{155}Gd, all the level energies depicted are in keV 37

2.10 Nilsson scheme for N $\geq$ 82. The arrow is pointing to the excited state of the unpaired neutron 38

3.1 A frontal side view of the Light Ion detector in the test setup. The entrance window of the detector at the top indicated by an arrow 42

3.2 A cut-through of all the components inside the LIon detector 42

3.3 A lateral view of the GEANT4 model of LIon without casing, to view the interaction with the beam of each volume. The beam entering the detector volumes consists out of 10 MeV protons. The volumes from left to right: Mylar window, Pos 2, ΔE2, ΔE1, Pos 1, Aluminized Mylar wrapping, scintillator 44

3.4 A angled view of the final GEANT4 model of LIon with casing, a 10 MeV proton beam enters the detector 45

3.5 Energy deposition histogram of the scintillator with 10 MeV protons 45

3.6 A histogram to compare the mean energy deposition of 500 entries in all volumes in the detector for different particles and energies. The standard particle is the 10 MeV proton in orange, with a higher energy proton (20 MeV) in blue. Different particle types with the same energy display in grey as 10 MeV deuterons 46

3.7 GEANT4 simulation with a 50 MeV $^{16}0$ beam entering LIon 48

3.8 GEANT4 simulation of a 70 MeV ^{16}O beam entering LIon 49

3.9 A histogram to compare the average energy deposition of 500 entries with 50 and 70 MeV ^{16}O beam in GEANT4. The left bar is the 50 MeV ^{16}O while the right bar is the 70 MeV variant. Anode 1 and Position wire 1 are empty 49

3.10 GEANT4 simulation of a 10 MeV deuteron beam into LIon 50

3.11 A histogram made in ROOT from experimental data with 10 MeV deuterons entering LIon's scintillator 50

3.12 A histogram made in ROOT from simulation data with 10 MeV deuterons entering LIon's scintillator 51

3.13 The setup of the test chamber of the particle spectroscopy team with LIon inside. The test chamber is at vacuum pressure, and the magnet on top indicates the placement of the α-source 52

3.14 A average energy deposition of different gas densities with the triple α-source 53

3.15 GEANT4 simulation of a the triple alpha source beam into LIon. The entrance into the detector is not angled as the magnet indicating the source is in de middle of the detector 53

3.16 A histogram to compare the average energy deposition of different gas densities with the triple α-source accumulated in a simulation 54

4.1 Figure to show the working principle of a Van der Graaff accelerator 58

4.2 A structured view of the HIAF facility with all its beam lines 59

4.3 A picture of the ^{155}Gd target 60

4.4 The target chamber at beamline 5 with a plug to keep the Enge and LIon at vacuum 61

4.5 Figure to explain the mechanism of the Enge spectrometer, which aligns particles onto the focal plane detector 62

4.6 The Enge spectrometer at the HIAF facility. It is positioned on rails to rotate the spectrometer 62

4.7 A front view on the left and a side view on the right of the Pixie-16 digitizer 63

4.8 The calculation of Eq. 4.1 & 4.2 to visualize the safe energy per angle . . . 64

4.9 Relative cross sections calculated by GOSIA 69

5.1 The calibration of the time difference with the gyroradius executed by the known peaks of ^{54}Fe 74

5.2 The working principle of a TFA explained, in which a signal gets modeled down to a shorter signal. The original signal gets shortened to decrease the dead time 75

5.3 The spectrum for 12 MeV protons and a 20° scattering angle 75

5.4 The spectrum for 12 MeV protons and a 25° scattering angle 76

5.5 The spectrum for 12 MeV protons and a 30° scattering angle 76

5.6 A zoomed-in spectrum for 12 MeV protons and a 20° scattering angle . . . 77

5.7 A zoomed-in spectrum for 12 MeV protons and a 25° scattering angle . . . 77

5.8 A zoomed-in spectrum for 12 MeV protons and a 30° scattering angle . . . 77

5.9 The spectrum from the scintillator at 20 degrees with 12 MeV protons . . . 78

5.10 The spectrum from the scintillator at 25 degrees with 12 MeV protons . . . 79

5.11 The spectrum from the scintillator at 30 degrees with 12 MeV protons . . . 79

5.12 The spectra of a 12 MeV 20 degree scattering angle from both sides of the scintillator. On the right side the spectra of the high-energy side, while on the left the low-energy side 80

5.13 The spectra of a 12 MeV 25 degree scattering angle from both sides of the scintillator. On the right side the spectra of the high-energy side, while on the left the low-energy side 80

5.14 The spectra of a 12 MeV 30 degree scattering angle from both sides of the scintillator. On the right side the spectra of the high-energy side, while on the left the low-energy side 80

5.15 A 3D view of the GEANT4 simulated model of LIon with 10,000 entries of a 12 MeV proton beam and 25 degrees 81

5.16 The spectrum from the simulated GEANT4 model for a 12 MeV proton beam at a 20-degree scattering angle 82

5.17 The spectrum from the simulated GEANT4 model for a 12 MeV proton beam at a 25-degree scattering angle 82

5.18 The spectrum from the simulated GEANT4 model for a 12 MeV proton beam at a 30-degree scattering angle 83

5.19 A summation of the probabilities from the ground state and the first excited level for the 25 degree scattering angle with an equal amount of counts as the correlating experimental measurement 83

5.20 The combination of the probabilities of GOSIA (red) and the experimental data (blue) for a 12 MeV proton beam with a 25 degree scattering angle . 84

5.21 The relative cross section for the first excited state was calculated using GOSIA 87

5.22 The gas pressure in the detector affects the possible volts in the position wires 88

Glossary of symbols

A	number of nucleons, $Z + N$
α	the fraction of N_e on N_γ
$\alpha_{\lambda\mu}$	time-dependent amplitudes
ANU	Australian National University
BGO	bismuth germanate
B(L)	the so-called reduced transition probability
CAESER	compton suppressed array detector
Coulex	Coulomb excitation
cps	counts per second
ΔE	energy difference between initial and final state
DGF	digital gamma finder
e	elementary charge
E	electric transition
enA	attoampere
ENSDF	Evaluated Nuclear Structure Data File
ϵ_0	vacuum permittivity
fm	femtometers
GEANT4	GEometry ANd Tracking version 4
GQR	Giant Quadrupole Resonances
HIAF	Heavy Ion Accelerator Facility
HPGE	High-Purity Germanium
IC	internal conversion
ICC	internal conversion coefficient
I	total angular momentum
IT	internal transition
j	the total angular momentum
K	projection of the total angular momentum on the z-axis
L	angular momentum
L	angular momentum of the emitted photon
LDM	Liquid Droplet Model
LET	Linear Energy Transfer
LIon	Light Ion Detector
λ	multipolarity
ℓ	orbital angular momentum

MC	Monte Carlo
m_p	proton mass
MSPS	mega samples per second
η	
N	number of neutrons
N_e	amount of internal conversion electrons
NNDC	National Nuclear Data Center
N_γ	amount of internal transition gammas
p	linear momentum
π	parity quantum number
$\psi_{f,i}$	the initial and final quasi-stationary states of the system
Q_0	intrinsic quadrupole moment
q_p	charge of the proton
ρ	gyroradius of the magnetic field
$R(t)$	time-dependent radius of a vibrating nucleus
R_{av}	equilibrium radius of a nucleus in collective excitation
s	spin quantum number
SiPM	Silicon PhotoMultiplier
τ	mean half-life
τ_{coll}	collision time
TFA	Timing Filter Amplifier
TOF	Time Of Flight
T	Tesla, a unit of magnetic field strength
V	time independent model
V_c	Coulomb force
UD	units doubled
Y_{20}	spherical harmonic in rotational states
$Y_{\lambda\mu}$	spherical harmonic functions in collective excitation
Z	number of protons

Abstract

As global energy demand increases, nuclear batteries offer a promising solution due to their high power density and long operational life. Two main challenges must be addressed to achieve isomer power: identifying pathways by which their energy can be released, and mechanisms to do so safely and on demand. This thesis addresses the latter through low-energy Coulomb excitation.

Protons with 12 MeV were scattered from a ^{155}Gd target. A magnetic spectrograph selected particles of interest based on magnetic rigidity at 20°, 25°, and 30°. A search for the low-lying, first excited state in ^{155}Gd (60 keV) was performed. Out of 300,000 recorded entries for each angle, around 100,000 were found in the ground state. Theoretical modeling was conducted using GEANT4, a Monte Carlo toolkit, and the semi-classical code GOSIA.

Detailed data analysis showed overlapping peaks between ground and excited states at all angles, meaning that the 60-keV state of interest could not be resolved. The first excited state's transition probability was also predicted to be too low for a visible peak. Low-energy tails from straggling of intense elastic-scattering events, contaminants and a high level density further complicated the spectrum. The GEANT4 simulation validation agrees on the elastic peak but reveals inelastic discrepancies. Improved position resolution could be achieved with thinner targets and operating at lower beam energies. Gamma-ray spectroscopy also remains a viable alternative approach.

Abstract in Dutch

Naarmate de wereldwijde energievraag toeneemt, bieden nucleaire batterijen een veelbelovende oplossing vanwege hun hoge energiedichtheid en lange operationele levensduur. Twee vragen zijn resterend voor succesvolle isomeer-energie: het identificeren van een pad waarop deze energie kan worden vrijgemaakt, en mechanismen om dit veilig en op vraag te doen. Deze thesis focust op het tweede, via low-energy Coulomb-excitation.

Protonen van 12 MeV werden gericht op een 155Gd-target. Een magnetische spectrograaf focusseerde deeltjes bij 20°, 25° en 30° op basis van magnetische rigiditeit. De laaggelegen, eerste aangeslagen toestand in 155Gd (60 keV) werd onderzocht. Van 300.000 entries per hoek kwamen er 100.000 uit de grondtoestand. Theoretische modellering gebeurde met GEANT4 en de semi-klassieke code GOSIA.

Gedetailleerde data-analyse toonde overlappende pieken tussen de grondtoestand en aangeslagen toestanden bij alle hoeken, waardoor de onderzochte 60-keV-toestand niet kon worden geanalyseerd. De probabiliteit van de eerste aangeslagen toestand werd voorspeld te laag te zijn voor een zichtbare piek te doen ontstaan. Een staart van verstrooiing van intense elastische reacties, contaminaties en een hoge toestandsdichtheid bemoeilijkten het spectrum. De validatie van de GEANT4-simulatie komt overeen met de elastische piek, maar toont discrepanties bij inelastische verstrooiing. Een verbeterde positieresolutie kan worden bereikt met dunnere targets en lagere bundelenergieën. Gammaspectroscopie blijft een alternatief.

Chapter 1

Introduction

As society progresses towards increased need for electricity, the demand for high-capacity energy-storage solutions continues to grow. For example, batteries for electric vehicles need higher power and energy density to achieve greater driving distances. However, current lithium-ion battery technologies face limitations in both aspects; currently, a scarcity of lithium is also developing. Amid significant efforts to achieve net-zero CO_2 emissions, the goal of the Paris Agreement to reach this target by 2050 has made energy even scarcer [1].

Research into new energy technologies is prevalent, and nuclear technologies could play a vital role in modern energy solutions. The Australian National University (ANU) is undertaking a foundational program that investigates nuclear batteries with metastable excited states, known as nuclear isomers. These devices could potentially yield energy with densities ten times higher than that of hydrogen cells and even a thousand times more than that of an electrochemical battery. Furthermore, nuclear batteries produce no direct CO_2. Together with an extremely long half-life without the need to recharge, a nuclear battery could significantly disrupt global battery technologies [2].

The path to unlocking a nuclear battery with long-lived metastable states still faces issues. The two primary challenges involve; identifying the optimal depletion pathway within the metastable excited state, and ensuring on-demand energy release. Isomers are long-lived, or metastable, arrangements of nuclei that are excited states relative to their respective ground state, which can be seen as a state that traps energy. Isomers are long-lived as transitions are often prohibited [3]. However, this process takes place following an exponential decay law of physics that cannot be altered. Nevertheless, isomers can only be useful power sources if their energy can be released on demand. This thesis addresses the second of the two primary challenges in nuclear battery research: developing on-demand energy release mechanisms in nuclear isomers.

Many ways have been proposed to deplete the isomer of its excess energy. The ANU Heavy Ion Accelerator Facility (HIAF) has been doing research on this topic for many years and believe the next step forward is Coulomb excitation. In this method an inelastic interaction is used to excite the isomer, by entering a new excited state the transition to a lower lying state is promoted. Coulomb excitation research has until now included gadolinium (Gd), cadmium (Cd), and tin (Sn) [4]. To capture the energy when it is released from the isomer and transfer it into electricity, a distinction is made between thermal and non-thermal

conversion [5].

However, previous Coulomb-excitation research on gadolinium-155 was unable to succeed as too many levels were excited during the Coulomb excitation process. The experiment utilized a ^{16}O beam directed at a ^{155}Gd target, with data collected through gamma spectroscopy. It used the Compton Suppressed Array detector, commonly known as CAESER, which comprises three arrays of detectors: nine high-purity germanium (HPGe) semiconductor gamma-ray detectors, nine bismuth germanate (BGO) Compton-suppression shields, and eight particle detectors. The nine HPGe detectors fit into the BGO Compton suppressors through holes. These detectors are then arranged over a wide range of angles, as illustrated in Fig. 1.1.

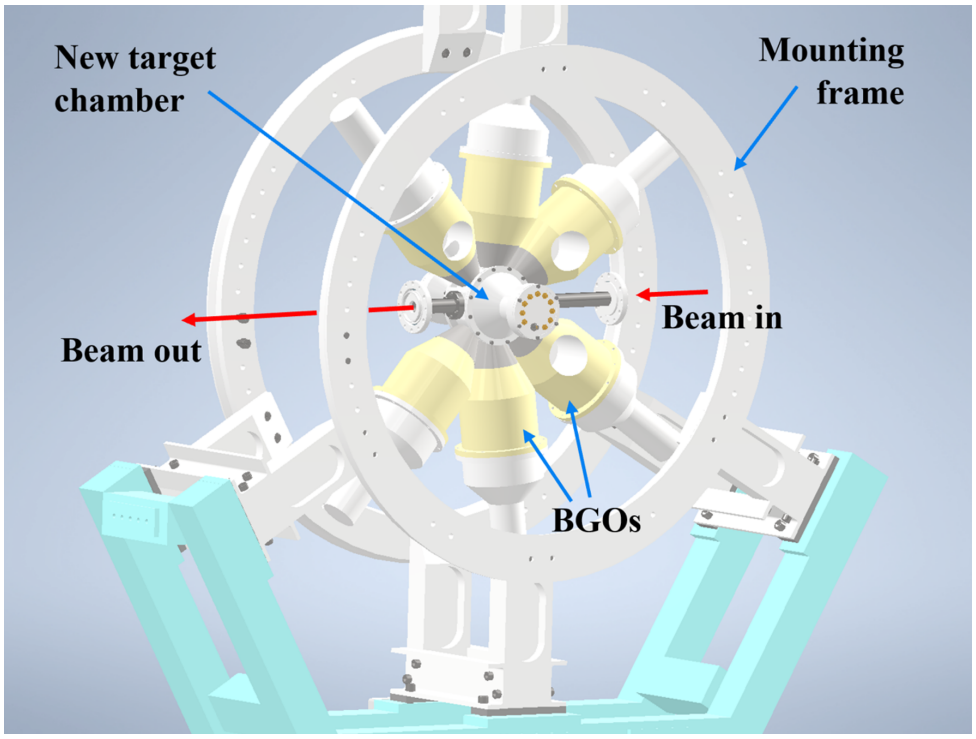

Figure 1.1: An image of CAESAR with the HPGe detectors already placed in the BGO holes. There are three additional detectors in the array that are not shown in this image.

Figure 1.1 shows only six of the nine HPGe detectors in the array. These detectors are cooled with liquid nitrogen, which requires refilling every few days. A large array of detectors is necessary for gamma spectroscopy because gamma rays, the particles of interest, are complex to measure. Consequently, this leads to low efficiency in the measurements.

A calibration of CAESER was performed by collecting data from two calibration samples. As a result, CAESER is now calibrated for energy and efficiency using the detected gamma rays from known transitions in these radioactive samples. Gamma spectroscopy offers excellent position resolution; however, analyzing the data involves multiple steps. Various corrections prone to human error are necessary to fully interpret a spectrum generated by gamma spectroscopy.

One reason corrections are needed is due to the movement of the nucleus in the target. When the target is excited by the scattering process, it can induce a slight movement of the target nucleus, causing an indirect γ-ray to be emitted from a different position. After implementing the required correction factors, Fig. 1.2 represents the spectrum of a 46 and 52 MeV ^{16}O beam on a ^{155}Gd target.

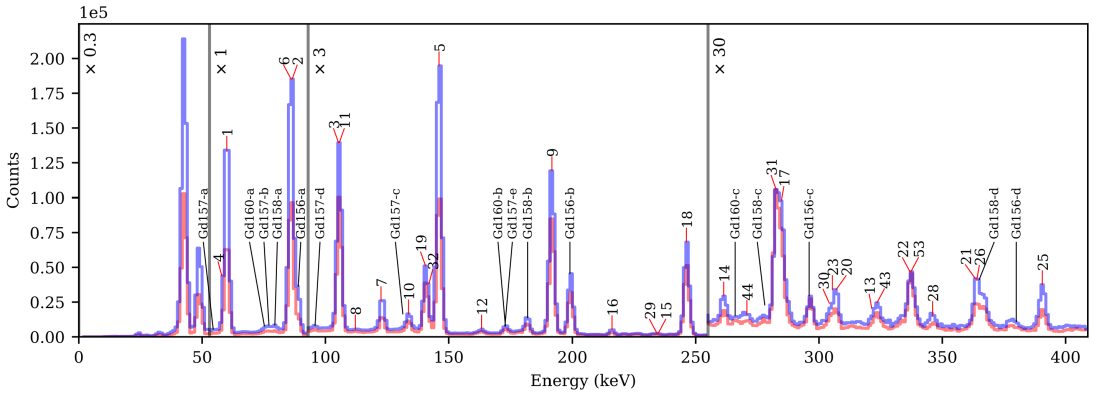

Figure 1.2: The spectra generated by [6] with gamma-spectroscopy, a 52 MeV ^{16}O beam incident on a ^{155}Gd target. The red indicates the 46 MeV beam while the blue represents the 52 MeV oxygen-beam. The vertical lines indicate where the scale changes.

A more straightforward approach to studying Coulomb excitation is particle spectroscopy. Instead of measuring γ-rays, this method involves measuring the projectiles after they interact with a target. This interaction causes an energy loss of the projectile that is characteristic of each scattering process. Particle spectroscopy was a widely used technique from the 1950s to the 1970s, but it became less common as the quality of HPGe detectors improved. However, a recent paper by [4] highlighted that particle spectroscopy still has applications in Coulomb excitation.

According to the statement from [4], due to unsuccessful gamma spectroscopy and an opportunistic approach to commissioning the Light Ion (LIon) detector at ANU, particle spectroscopy was selected as the preferred method. LIon is a focal plane detector recently developed at ANU for measuring light ions, particularly in Coulomb-excitation applications.

GOSIA, a semi-classical code, is utilized for designing and analyzing the experiment. It computes cross sections based on initial matrix elements that specify the appropriate beam energy and scattering angle. The extraction of data from the experiment remains unaffected by the type of spectroscopy used [7]. The abundance of states imposed a particular problem for GOSIA, as too many levels had unsolved variables in the research of [6]. To resolve this issue, a lighter particle and smaller scattering angles induces fewer excited levels. The GOSIA approach incorporates core assumptions not yet validated experimentally at lower energies [8]. This thesis establishes a framework to investigate these premises.

Understanding low-energy Coulomb excitation opens the door to exploring various nuclides. One noteworthy option is ^{242}Am, which possesses several characteristics that make it a promising candidate for isomer power. The isomer of ^{242}Am, located at 49 keV, has a remarkably long half-life of 141 years, especially when compared to the ground state's half-life of just 16 hours. Its favorable properties are significant because of the E2 γ-decay

pathway via a 53 keV state leading to the ground state [9]. However, a detailed analysis of this isomer is beyond the scope of this work.

To understand its performance, a simulation of LIon was made in GEANT4. This Monte Carlo (MC) code, written in C++, simulates the passage of particles through matter. The simulation model of LIon uses real-life geometries to simulate the output of the detector. This is especially useful for observing the reactions within the detector, which helps in selecting the appropriate beam energy. It also predicts the energy deposition of various particles with different energies in the various volumes of the detector [10].

This thesis presents the first Coulomb-excitation study with new research infrastructure at HIAF. The LIon detector was built to perform measurements of light ions from nuclear reactions. The project involves the use of HIAF's 15-million-volts tandem Van der Graaff accelerator, Enge magnetic spectrometer, and the LIon detector. It focuses on low-energy Coulomb excitation by exciting the isotope ^{155}Gd with an incident proton. The selection of beam energy and scattering angle is aided by GOSIA and GEANT4. This thesis paves the way for successful low-energy Coulomb excitation in nuclear batteries by doing research on ^{155}Gd, as this isotope could gain a lot of attention due to its first excited state at 60 keV.

Chapter 2

Background

This chapter offers a comprehensive exploration of several key aspects of Coulomb excitation. To fully understand Coulomb excitation involving isomers, it is essential to grasp the fundamental models in nuclear structure. Therefore, this chapter includes a detailed explanation of nuclear structure. The types of isomers are described and the theory behind isomer power is explained.

Subsequently, the chapter shifts its focus to more practical approaches. Particle spectroscopy and Coulomb excitation are crucial components of this research, and a complete understanding of these topics is necessary. Coulomb excitation is explained and previous research on the subject is revealed. The final subsection introduces the selection of ^{155}Gd and references previous research on this nuclide.

2.1 Nuclear Structure

For any nuclide, the total number of nucleons (A) is the sum of its protons (Z) and neutrons (N). It is denoted as ${}^{A}_{Z}\mathrm{X}_{N}$, with X being the chemical symbol of the element which is determined by its number of protons. Nuclei that have the same amount of protons but a different number of neutrons are called isotopes. The protons define the overall electrical charge of the nucleus, and the number of electrons present in the atom to give an atomic system that is electrically neutral. [11].

The nuclear core is governed by two principal forces: the strong nuclear force and the Coulomb force. Both forces exhibit significant range dependence. For short distances, on the order of 1-2 femtometres (fm), the nuclear force is attractive. Essentially holding nucleons together. However, at exceedingly short distances, less than about 0.5 fm, the force becomes repulsive. Figure 2.1 shows the potential of the force according to the distance [11], [12].

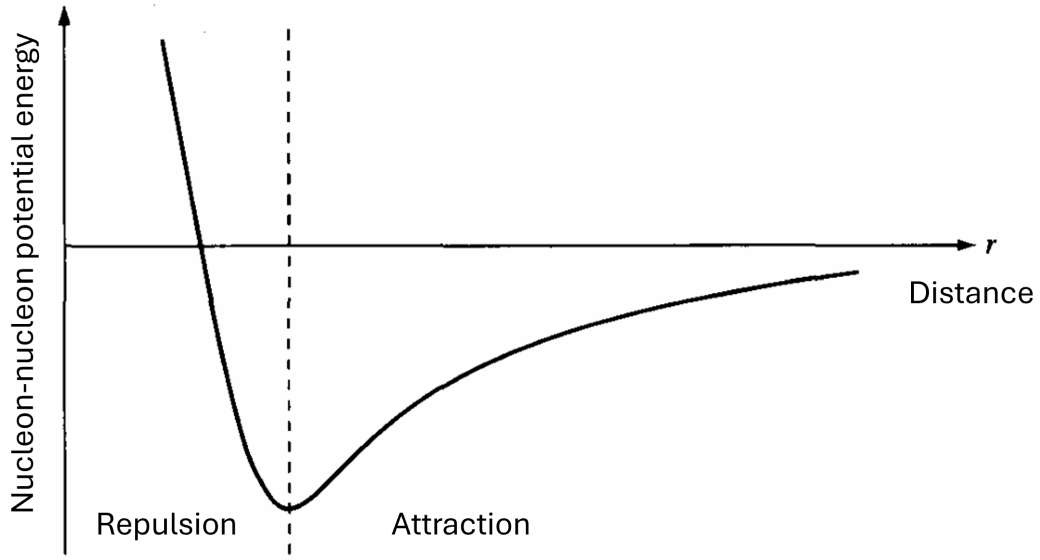

Figure 2.1: Nucleon-nucleon potential energy as a function of their separation [12].

The Coulomb force is weaker than the strong nuclear force at short distances. However, it dominates at larger distances. It provides a negative contribution, which arises from the long-range repulsive electrical force that exists between protons. The Coulomb force (V_c) increases with higher Z, this is due to [11]–[13]:

$$V_c(r) = \frac{-Ze^2}{4\pi\epsilon_0 r}. \tag{2.1}$$

In this formula ϵ_0 is the vacuum permittivity, e^2 displays the square of the elementary charge, and r is the distance. Together, the Coulomb force and strong nuclear force combine to form an attractive force which acts on the orders of fm to contain the nucleus. Due to the $\frac{1}{r^2}$ dependence of the Coulomb interaction, there is a repulsive barrier, known as the Coulomb barrier, that prevents nuclei from joining together. The Coulomb barrier is the force that is needed to bring two nuclei together until are touching [12].

2.1.1 Shell model

A commonly used model is the nuclear shell model, it assumes that there is an ordered structure within the nucleus, in which the neutrons and protons are arranged in quantum states in a potential well. Analogue to atomic shells filled with electrons in order of increasing energy, creating an inert core of filled shells and some valence particles that exist outside of them [12], [13].

Certain numbers of nucleons lead to enhanced stability and similar overal properties; these are known as the 'magic numbers'. These magic numbers, with Z or $N = 2$, 8, 20, 28, 50, 82 and 126, correspond to filled shells and represent one limit of nuclear behaviour, in that the available nucleus can often be described by the behaviour of a small number of valence particles. [12], [13].

A nucleus is a quantum-mechanical object, greatly restricting the number of possible nucleon-nucleon pairs due to the exclusion principle. Nucleons will occupy allowed energy states up to a specific energy, better known as the Fermi energy. In such a situation, there can be no transfer of energy or momentum between two colliding nucleons in filled states because all states lower in energy are occupied. Also, the energy of the nucleus is close to its respective ground state energy. Therefore will the nucleons move within the nucleus as if they were transparent to each other [12], [13].

Angular momentum

Solutions of the Schrödinger equation for a three-dimensional potential show that angular momentum plays a crucial role. Particles may move with orbital angular momentum with respect to the centre of the well in a three-dimensional potential. Unlike classical mechanics, in quantum mechanics, angular momentum occurs in discrete amounts. Orbital angular momentum is specified by a positive, integer quantum number ℓ, with $\ell \geq 0$. It is defined as [13]:

$$\vec{\ell} = \vec{r} \times \vec{p}, \tag{2.2}$$

where $\vec{r}$ is the position vector and $\vec{p}$ the linear momentum. The magnitude of the orbital angular momentum is given by [13]:

$$|\vec{\ell}| = \hbar\sqrt{\ell(\ell+1)}, \tag{2.3}$$

with $\hbar$ the reduced Planck constant. Angular momentum is a constant of the motion. Importantly, it is labelled using spectroscopic notation, which is summarized in Table 2.1 [13].

ℓ	Notation
0	s
1	p
2	d
3	f
4	g
5	h

Table 2.1: Spectroscopic notation of quantum orbitals.

For a complete description of a nuclear state, intrinsic angular momentum, or spin, must also be considered. Spin is a fundamental property of particles, with fixed values for each particle type. Protons and neutrons are fermions, as they have a spin quantum number, $s = \frac{1}{2}$. The spin vector can have two orientations, $+\frac{1}{2}$ or $-\frac{1}{2}$. The total angular momentum (j) is now expressed as [12], [13]:

$$\vec{j} = \vec{\ell} + \vec{s}. \tag{2.4}$$

As previously mentioned, the orbital angular momentum is usually written in subscript. Therefore, the solutions to j, for $\ell = 1$ and spin $= \frac{1}{2}$ are $p_{1/2}$ and $p_{3/2}$ [12], [13].

Parity

Mathematically, nucleons are described by a quantity known as the wave functions. This introduces an additional property known as parity; this operator causes a reflection of all of the coordinates through the origin. Meaning:

$$\vec{r} \rightarrow -\vec{r}. \tag{2.5}$$

This feature creates two classes of wave functions: ones that are invariant under this operator and the ones that are not. These are valued as positive and negative parity, respectively. A parity quantum number is assigned, $(\pm)\pi$. All states of a particle have a definite parity, which is negative where ℓ is odd and positive if ℓ is even. Parity is conserved when the total parity quantum number is unchanged after an interaction, which is the core in many nuclear reactions and decays [11].

2.2 Collective Excitations

The nuclear shell model has proved to be very successful in accounting for the ground-state properties and low-lying excited states of many nuclei. Nevertheless, there are certain modes of excitation, found in most nuclei, which are better described as collective vibrations and rotations of the nucleus. A collective model is born out of reconciling the shell model with the liquid drop model [11], [12].

This model states that the nucleus has a hard core of nucleons in filled shells, with outer valence nucleons. Such a nucleus can both rotate, and vibrate. From these new degrees of freedom, rotational and vibrational energy levels arise [11], [12].

2.2.1 Vibrational states

The liquid-drop model predicts that a nucleus will be spherical in its ground state. Vibrational excitations are described as oscillations in which the nucleon surface moves around a spherical equilibrium shape. Essentially, even though the average shape is spherical, the instantaneous one may not be. The shape of the vibrating nucleus is described by:

$$R(t) = R_{av}\left[1 + \sum_{\lambda=0}^{\infty}\sum_{\mu=-\lambda}^{\lambda}\alpha_{\lambda\mu}(t)Y_{\lambda\mu}(\theta,\phi)\right], \tag{2.6}$$

where $R(t)$ is the coordinate dependent on time, R_{av} is the equilibrium radius of the nucleus, $\alpha_{\lambda\mu}$ are time-dependent amplitudes, and $Y_{\lambda\mu}$ are the spherical harmonic functions. The first possible states at low-energies are monopole, dipole, quadrupole, and octupole vibrations shown in Fig. 2.2 [13].

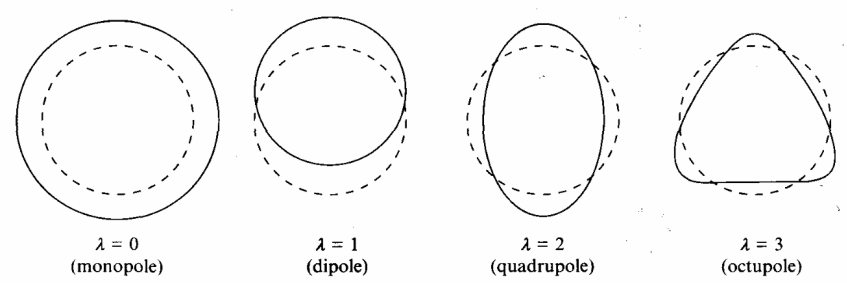

Figure 2.2: The four vibrational modes of nuclei, each mode is a vibration about the spherical equilibrium [13].

The monopole ($\lambda = 0$) is forbidden for low-energies because the nucleus is incompressible. The dipole ($\lambda = 1$) results in a shift in the center of mass and cannot result from internal nuclear forces. Consequently, the quadrupole ($\lambda = 2$) is the lowest state observed at low energies. There are two main types of quadrupole vibrations: Giant Quadrupole Resonances (GQR), which involves the entire nucleus, and vibrations of nucleons at the nuclear surface. The GQR occurs at energies above 10 MeV, while nucleons at the nuclear surface vibrate at low energies and in collective 2^+ states in spherical nuclei. An octupole, which carries three units of angular momentum ($\lambda = 3$), gives a 3^- state when coupled with a 0^+ ground state. Octupole vibrations usually occur at higher energy than the 2^+ vibrational state, however, at higher energies, the vibrational structure begins to dominate for particle excitation corresponding to the breaking of a pair in the ground state. The quanta of vibrational energy are called phonons [12], [13].

2.2.2 Rotational states

Collective rotational motion can only be observed in nuclei with a non-spherical shape. A spherical shape has no preferred direction in space, and a rotation does not lead to any observable change. These deformations are commonly seen in the rare-earth and actinides region, ranging from $150 < A < 190$ and $A > 230$. A common representation of the shape of these nuclei is that of an spheroid, the surface of which is described by:

$$R(\theta, \phi) = R_{av} \left[1 + \beta Y_{20}(\theta, \phi)\right], \tag{2.7}$$

R(θ, ϕ) is the coordinate dependent on two angles,R_{av} is the average spherical radius, and Y_{20} is the spherical harmonic. Both are independent of ϕ, which gives the nucleus cylindrical symmetry. The deformation parameter (β) indicates the magnitude of deformation and its sign the shape; when $\beta > 0$ the nucleus is prolate, and when $\beta < 0$ the nucleus is oblate. The increase in energy for rotational states is given by:

$$E = \frac{\hbar^2}{2\eta} I(I+1), \tag{2.8}$$

where I represents the angular momentum and η the moment of inertia. Increasing the quantum number I corresponds to adding rotational energy to the nucleus, causing the excited states to form a rotational band. The rotational band connects lower excited states with higher excited states. Equation 2.8 explains why the energy ratio $E(4^+)/E(2^+)$ equals 3.33 in the deformed region, compared to approximately 2 outside this region, serving as an indicator of nuclear deformation. Figure 2.3 illustrates a level scheme from a rotational state of the ground state in ^{164}Er [13]. This isotope shows an $E(4^+)/E(2^+)$ energy ratio of 3.28, a clear sign of deformation.

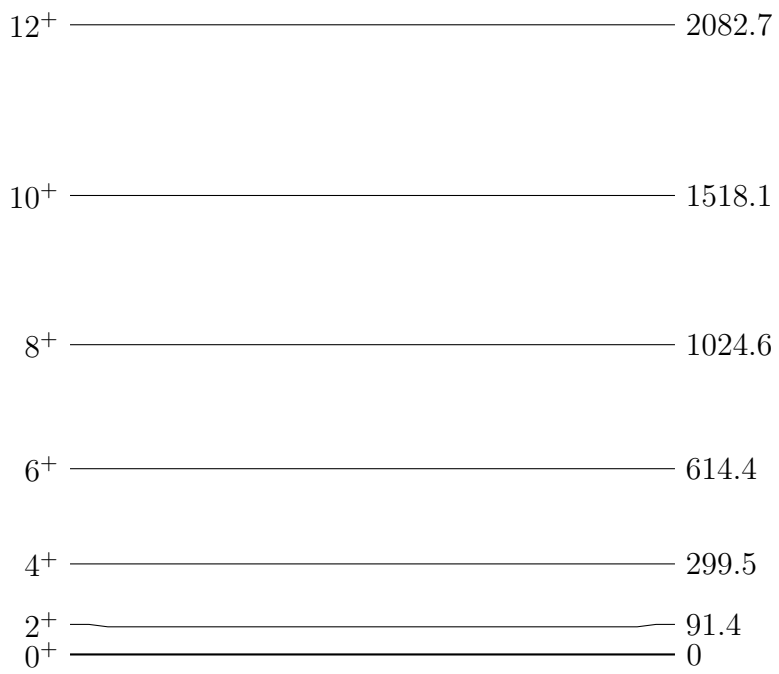

Figure 2.3: A level scheme of ^{164}Er where the excited state are a result from the rotation of the ground state. Energies are displayed in keV [13].

The coupling within the rotational band adds complexity to the analysis of ^{155}Gd, as discussed by [6]. The high level density of this isotope leads to significant coupling, complicating the analysis.

2.3 Electromagnetic decay

2.3.1 γ-transitions

Nuclei in excited states can transition to a lower-lying energy state or ground state by emitting energy in the form of one or more gamma rays. They are high-energy photons and carry no mass or charge, therefore not changing the chemical properties of the isotope. The energy of these photons is determined by the average energy level spacing in nuclei. In addition, its properties, such as the angular momentum and parity, correspond to the characteristics of the initial and final state. Even their lifetime is very sensitive to the amount of energy released in the transition [11].

Gamma decay is not the only electromagnetic mechanism available. The total transition probability is the sum of the gamma, internal conversion, and internal pair creation

probability. With internal conversion, the nucleus de-excites by ejecting an atomic electron. For internal pair creation the energy needs to be sufficiently high, a threshold of 1022 keV, to create an electron-positron pair [12]. While gamma transitions generally have the highest probability for most isotopes, this is not true for ^{155}Gd. As internal conversion can dominate the decay.

To address this, tables of branching ratios and internal conversion coefficients (BrIcc) are created to assist the analyzer in focusing solely on γ-ray examination. However, since this project utilizes particle spectroscopy, the specific type of transition is less significant. Nonetheless, the characteristic energy loss associated with gamma decay is important, as it depends on the selection rules and interaction.

2.3.2 Transition rules

There are selection rules based on parity and angular momentum for gamma decay. The most prevalent way of decay in isomers is internal transition, thus emitting a photon to lose energy. These rules originate from the conservation of angular momentum and parity during decay. The sum of angular momentum during the transition is given by: [13].

$$I_f = I_i + L. \tag{2.9}$$

Here, $I_{f,i}$ is the angular momentum of the final and initial state, where L equals the angular momentum of the emitted photon. This leads to the following constraints of angular momentum and spin coupling:

$$|I_i - I_f| \leq L \leq I_i + I_f. \tag{2.10}$$

To comply with the selection rule, parity needs to be conserved. A distinction is made between electric (E) and magnetic (M) transitions. The electric transitions arise from an oscillating charge which causes an oscillation in the external electric field. Meanwhile, the magnetic transitions come from a varying current or magnetic moment that sets up a varying magnetic field. Each transition has a 'multipolarity' which can be determined by studying states connected by a given transition [11].

To start, M1 transitions have no change in parity, while an E1 does. Fermi's golden rule defines the electric transitions. In case of the E1, the wave functions' matrix element can only be non-zero if the states have opposite parity. Therefore, E1 transitions demand a change of parity. If the initial and final state differ by more than one unit of angular momentum, it is called a higher-multipole transition. The options for a planar wave are seen in Figure 2.2. A higher multipole transition is less likely to occur, each multipole is determined by the vector of $\vec{r} \times \vec{p}$. Generally, a decay will proceed dominantly by the lowest order process permitted by angular momentum and parity. Table 2.2 shows the allowed transitions [11].

	Dipole	Quadrupole	Octupole
L	1	2	3
Type of transition	E1−M1	E2−M2	E3−M3
ΔP	Yes−No	No−Yes	Yes−No

Table 2.2: Allowed transitions for E and M up to $L = 3$

2.3.3 Transition probability

The transition probability is defined by the transition matrix element, which originates from Fermi's Golden Rule. The matrix element (V_{fi}) is the integral of the interaction V between the initial and final quasi-stationary states of the system ($\psi_{f,i}$), where the integral is carried out over the volume of the nucleus. V is the time-independent model [11].

$$V_{fi} = \int \psi_f V \psi_i dv. \tag{2.11}$$

Matrix elements enable the calculation of the mean life, or τ, which represents the average time a nucleus is expected to survive before it decays [13]. The emission probability per unit time, or emission rate can be obtained directly through eq. 2.12, where E_γ is the photon energy, E and M refer to electric and magnetic radiation [11].

$$T_{fi}^{E,M}(L) = \frac{1}{4\pi\epsilon_0}\frac{8\pi(L+1)}{L(2*L+1)^2}\frac{1}{\hbar}(\frac{E_\gamma}{\hbar c})^{2L+1}B_{fi}(L). \tag{2.12}$$

The function $B(L)$ is the so-called reduced transition probability and contains all the nuclear information, such as the multipolarity of the emitted photon and angular momentum. Moreover, it is the square of the modulus of the matrix element. Weisskopf has made simplifying assumptions so that a reasonable approximation for the single-particle reduced transition probability can be calculated. A distinction is made between electrical (E) and magnetic (M) transitions. The so-called Weisskopf estimates for an electric transition is given by: [11].

$$B^E(L) = \frac{e^2}{4\pi}(\frac{3R^L}{L+3})^2, \tag{2.13}$$

with R indicating the Rydberg constant. Whereas for a magnetic transition, it is:

$$B^M(L) = 10(\frac{\hbar}{m_p \mathrm{c} R})^2 B(L), \tag{2.14}$$

where m_p represents the mass of the particle and c the speed of light. Even though these are only predictions, they often agree well with values observed experimentally. For a given transition, there is a substantial decrease in decay rates with increasing multipolarity. Also, electrical transitions have decay probabilities about two magnitudes higher than the corresponding magnetic transitions. By evaluating the ratio of measured transition strength and Weisskopf single particle estimates, a transition strength with units of W.U. gives an indication of how many particles are involved e.g. single particle or collective model [11], [13].

To conclude, the Weisskopf units for the lowest multipole transitions are shown in Table 2.3.

Transition rate	Equation
$\Gamma_\gamma(E1)$	$0.068 E_\gamma A^{\frac{2}{3}}$
$\Gamma_\gamma(M1)$	$0.021 E_\gamma^3$
$\Gamma_\gamma(E2)$	$(4.9 \times 10^{-8}) E_\gamma A^{\frac{4}{3}}$

Table 2.3: Weisskopf units estimates for E1, M1, and E2 transitions.

2.4 Nuclear Isomers

2.4.1 Isomeric states

Isomers, represented by the symbol 'm', are excited states of atomic nuclei that contain the same number of protons and neutrons as their ground states. Still, they have longer half-lives compared to typical excited states. This phenomenon was first discovered in 1921 by the German chemist Otto Hahn during his research on uranium salts. A well-known example of an isomer is technetium-99m (^{99m}Tc), used in various medical diagnostic applications; its ground state is technetium-99 (^{99}Tc) [3].

There is no universally agreed-upon minimum half-life constraint for defining an isomer, as the ability to observe and separate isomers depends on the available techniques. Generally, these excited states last more than a picosecond relative to a typical decay on the order of femtoseconds [3].

Currently, 3437 isomers are listed in the most recent NUBASE evaluation, and 1318 have at least one metastable excited state with a half-life of 100 ns or longer. It is important to note that a nuclide can possess multiple isomeric states. For instance, ^{187}Hf has two known isomeric states known as ^{187m1}Hf and ^{187m2}Hf, each characterised by unique de-excitation energy and half-life [3]. Even in some cases, it is seen that the isomeric state has a longer half-life than its ground state. For example, the half-life of ^{242m}Am is 141 years while ^{242}Am is 16 hours. [9].

The primary decay is via internal transitions (IT). However, other decay mechanisms, such as beta or alpha decay, are also observed. Understanding and measuring the half-life of an isomer presents significant challenges due to the wide range of possible values, spanning from picoseconds to years. Theoretically, the gamma-ray partial half-life depends on the angular momentum, parity of the initial and final state, and the matrix element of the operator responsible for the transition between the two states. This relation is given by [3], [13]:

$$T_{1/2} \propto \frac{1}{|\langle f|T_\lambda|i\rangle|^2 (E_\gamma)^{(2\lambda+1)}}. \tag{2.15}$$

2.4.2 Isomers types

At first, it was believed that isomers formed due to a connection between a significant change in angular momentum and small decay energy during de-excitation. However, later a better prognosis formed since the creation of isomers depends on the individual nucleon orbits and the collective behaviour of the whole nucleus. Consequently, the three main types of isomers are outlined below [14].

Spin Isomers

The first and most dominant class of isomers are caused by significant spin changes, also called spin traps. The properties of the possible decay routes determine the lifetime of an excited nuclear state. Spin isomers are formed due to the significant change in spin, which results in a low electromagnetic transition rate and a long half-life [15].

For an isomer to internally decay, selection rules apply. The multipolarity determines the transition type as for large L it inhibits the decay. Also, E0 transitions, where $J_i = 0$ and $J_f = 0$, which requires an L= 0, are entirely forbidden from quantum mechanics since the photon must carry at least $L = 1\hbar$ [15].

While IT is often preferred, internal conversion (IC) competes with it, especially for low-energy isomers. IC is a process where an excited nucleus interacts electromagnetically with an atomic electron. As previously mentioned, E0 transitions are prohibited by the gamma selection rule. However, this is not true for IC. The competition between IT and IC is expressed by the conversion coefficient $\alpha = \frac{N_e}{N_\gamma}$, where N_e is the number of conversion electrons and N_γ is the number of gamma rays emitted [15].

The spin of an isomers depends on its structural properties in terms of the occupied orbitals and configurations, as well as other orbitals in their vicinity. Taking the shell model into account, the presence of unique parity intruder orbitals have high-j values, which fall at the top of each group after forming the shell just below the magic gaps. While all the orbitals in a shell belong to a given quantum number, the high-j orbital is of higher value. Thus, it has a different parity than the rest of the orbitals in the shell. This creates isomers near the magic numbers. Spin isomers are particularly prevalent near magic nuclei due to significant energy gaps with large angular momentum changes [15].

K-isomers

The second variant of isomers are called K-isomers and are typically seen in deformed nuclei. K represents the projection of the total angular momentum with respect to the Z-axis, illustrated in Fig. 2.4 [14], [15].

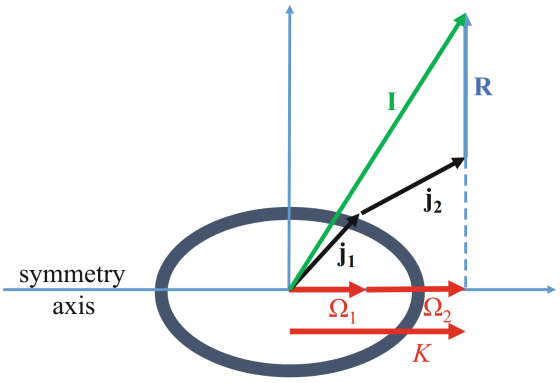

Figure 2.4: The K-projection of the isomer is the total angular momentum onto the symmetry axis [15].

Generally, transitions with significant changes in K are associated with long half-lives and K-isomers. It entails a significant change in the orientation of the angular momentum during the decay. Hence, a significant change in the wave function, which is not favoured by the nucleus. A transition is forbidden when the change in K, or ΔK, is bigger than the multipolarity of the gamma transition (λ). The selection rule is given by [13]:

$$v = \Delta K - \lambda, \tag{2.16}$$

where v defines the degree of forbiddenness. An example of these K-isomers due to high K-forbidden decays are ^{190}Os and ^{180}Hf, with Fig. 2.5 illustrating the ^{180}Hf hindered transition. For example, ^{180}Hf 8-, the K-value is 8; to become this the ΔK has to be 8. Meanwhile, the multipolarity becomes one, and therefore the degree of forbiddenness becomes 7. Giving rise to a long half-life of the isomeric state [15].

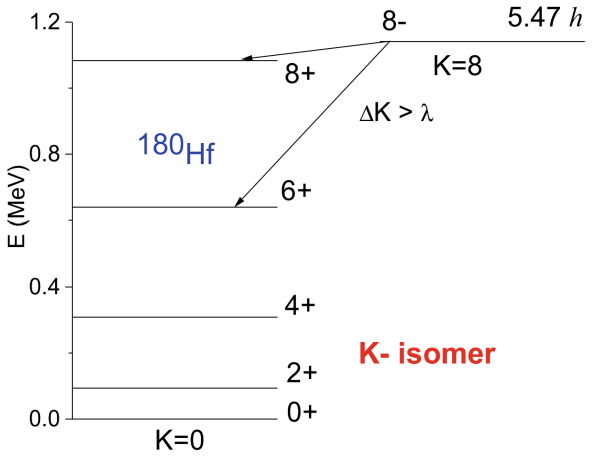

Figure 2.5: Level scheme of ^{180}Hf showing the transition from K= 8 to K= 0 [16].

While the Shell Model is crucial in understanding the spin isomers, the collective model is required to explain K-isomers. K remains a good quantum number if the axial symmetry in nuclear deformation holds. Therefore, the definition is limited to defining axial symmetry nuclei [15].

Shape (fission) isomers

The third and final class of isomers are called shape isomers. The shapes of nuclei are complex and depend on the N and Z configuration, excitation energy, angular momentum, etc. When a nucleus gets trapped in a secondary energy minimum, a gamma decay from the higher-lying state in the secondary minimum involves a significant shape change. This change hinders decay and gives rise to a longer half-life of the secondary minimum state or isomer. An example of a shape isomer is the 0^+ isomer in ^{72}Kr; this isomer exists as the $0^+ \rightarrow 0^+$ is hindered [15], [17], [18].

Like the two previous classes, shape isomers have their own properties. Firstly, its decay always involves shape deformation. Secondly, both the ground and excited shapes coexist with an energy barrier separating them [17], [18].

Another important class of shape isomers, called fission isomers, is found in heavier transactinides. Hence its name can decay due to spontaneous fission. Fission isomers have super-deformed shapes and represent super-deformation at very low spin. The fission isomer is formed because the nucleus gets captured in the second minimum at a super-deformed shape and can decay via either fission or gamma decay to the first minimum. The size and shape of the barrier decide the half-life of the fission isomeric state. An experiment by [18] in 1962 found isomeric fission from an excited state of ^{242}Am accidentally. Since 2002, 48 fission isomers have been known. Currently, 14 ms ^{242}Am is the longest-lived shaped isomer. The interest region for this class is very tightly located. It ranges from $90 \leq Z \leq 98$ and $141 \leq N \leq 151$ [17], [18].

The double-hump barrier model is shown in Figure 2.6 to understand whether the isomer's classification is shape or fission. This illustrates the effect of the Liquid Droplet Model (LDM) and shell corrections on whether a fission of shape isomer is formed [17], [18].

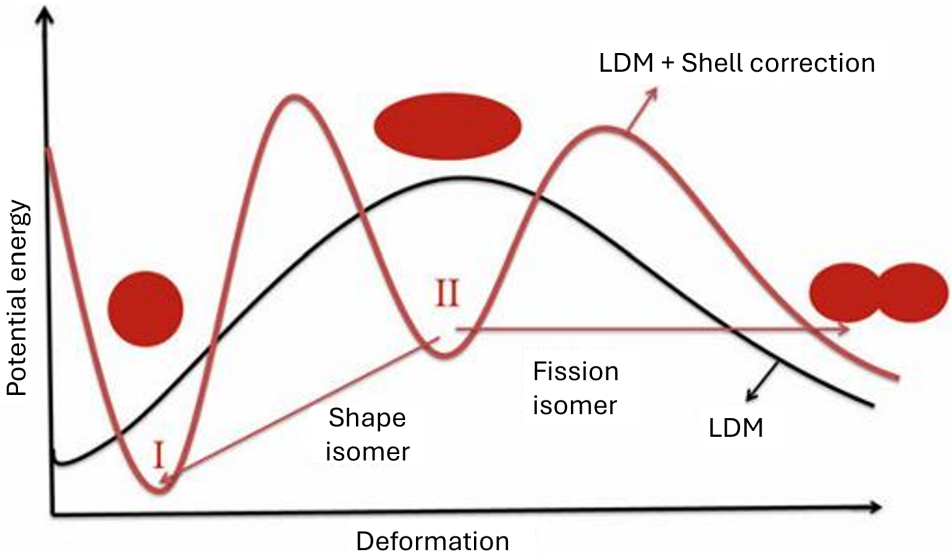

Figure 2.6: Double-hump-back model for shape isomers [17].

Figure 2.6 shows two potential energy barriers, and depending on the deformation, either a fission or shape isomer will be created. The shell corrections represent the quantum contribution to the nuclear potential energy that is missed in the potential energy of the classical LDM. The contribution of each depends on the deformation. The minimum value of this sum determines the equilibrium shapes of the nucleus [17], [18].

Half-life calculations of isomers are very difficult. The half-life depends on the overlap of the wave function of both states, the excitation energy of the isomeric state, and the height of the barrier for shape isomers [17], [18]. The complexity of the half-life calculation causes gaps in the half-life knowledge of isomeric states in ^{155}Gd.

2.4.3 Isomer Energy Storage

Isomers are formed when reaching a lower-energy state is challenging, effectively 'trapping' the nuclei in an excited state. This phenomenon has unique applications, such as batteries. However, the isomer can only be beneficial if it can be stimulated to release its energy on demand. Isomers, like any other nuclear state, have a decay probability based on their half-life, and there is no method to influence this. Exciting the isomer to a higher energy state can influence the transition strength to the ground state. Depending on the excited state, decay may occur through the emission of either multiple gamma rays or just a single gamma ray [11], [19].

Many studies have been performed in recent years seeking ways to deplete isomeric states to their respective ground state on demand, commonly referred to as isomeric triggering. This can be done in multiple ways, for example: photo-absorption; Coulomb excitation; or coupling to the atomic shells. By exciting the nucleus to a higher level, de-excitation can occur to a different lower-lying state. Therefore emitting a lot of energy on demand. Figure 2.7 displays how energy extraction works with Coulomb excitation [20].

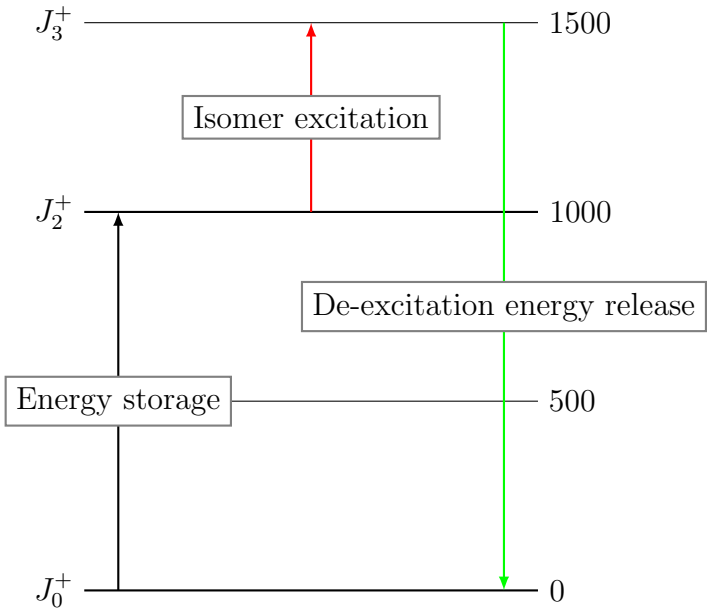

Figure 2.7: Arbitrary level scheme with J_2^+ an isomeric state, by exciting the J_2^+ isomeric state a energy release to the J_0^+ is stimulated.

This project contributes to a broader research initiative employing low-energy Coulomb excitation techniques to study the de-excitation of isomers.

2.5 Experimental probes of nuclear structure

2.5.1 Coulomb Excitation

Coulomb excitation, often referred to as 'Coulex', is a process in which a stationary nucleus is excited to a higher energy state by an energetic projectile. Energy loss is specific to each process and can be measured in two distinct ways. One method involves observing the gamma rays emitted as the excited state returns to a lower energy state. The other method measures the projectile after it has experienced energy loss. Both techniques are particularly valuable for studying isomeric de-excitation. It involves bombarding a target nucleus with an incident particle that has been accelerated to a specific energy using a particle accelerator, as illustrated in Fig. 2.8 [21].

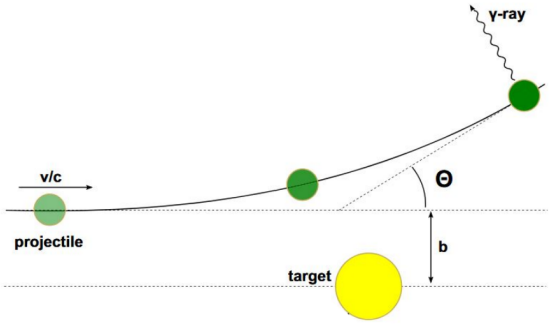

Figure 2.8: Depiction of the Coulex mechanism between an accelerated beam nucleus and a target nucleus [22].

Coulomb excitation is classified as an inelastic scattering process mediated by the electromagnetic force. The energy in centre-of-mass is carefully minimized to suppress strong-force contributions, isolating electromagnetic interactions during excitation [21], [23].

To ensure that excitation occurs without causing a nuclear reaction through the nuclear force, the energy of the incoming particle must be kept below the Coulomb barrier. This limitation prevents strong-force interactions between the incoming particle and the target nucleus, as the strong nuclear force operates only at very short ranges. Consequently, all observed gamma rays are solely a result of the electromagnetic de-excitation of the excited isomeric state [21], [23].

These experiments provide information through the direct observation of gamma-ray intensities resulting from the scattering of projectile particles. This observation requires detecting at least one of the collision partners within a specific angular and energy range. This method is widely regarded as one of the most reliable tools for accurately extracting essential nuclear information. Additionally, it is one of the few methods available for obtaining data on the static electromagnetic moments of short-lived excited nuclear states. This approach yields insights into the spin and parity of excited levels, as well as reduced transition probabilities or matrix elements [21], [23].

The probability of transitioning from a ground state to an excited state through more than one step, known as multi-step excitation, depends on the magnitudes of the involved matrix elements. Multi-step excitation can be limited by selecting smaller scattering angles and lighter masses for the collision partners [4].

Recent low-energy Coulomb-excitation studies have highlighted the importance of further research into the shell model. A study conducted by [4] employed similar instruments to those used at the ANU. It investigated super deformation in ^{42}Ca and the phenomenon of shape coexistence near the N=50 shell closure by measuring the excited states and determining the population of each state.

A study from [24] highlights the importance of high-precision experiments using Coulomb excitation. This technique enables a detailed analysis of E2 and E4 transitions in low-lying energy states, offering valuable insights into the shape of charge distributions. Coulomb excitation effectively links the two lowest excited states with the ground state in odd deformed nuclei. The study utilizes Coulomb excitation to compare Q_0 values obtained through transition moment measurements with those derived from other methods, such as conversion electron-yield determination. In conclusion, the authors find that while different methods produce comparable results, Coulomb excitation demonstrates greater accuracy overall.

For excitation to be viable, the perturbation of the electromagnetic potential experienced by the nucleus of interest needs to be sudden, i.e. the collision time (τ_{coll}) should not be longer than the fluctuation time of nuclear wave function given by:

$$\tau_{nuclide} = \frac{\hbar}{\Delta E}, \tag{2.17}$$

where ΔE is the excitation energy difference between the initial and final states. If $\tau_{\text{nuclide}} \gg \tau_{\text{coll}}$ then the changes of the electromagnetic field are too gradual for excitations to occur. For commonly used beam energies of a few MeV/A, it means an energy transfer cutoff of about 1-2 MeV. Additionally, the excitation process depends on the kinematics, the mass and atomic numbers of the target and projectile nuclei [23].

The contribution from short-range nuclear interactions can be neglected if the distance between the colliding partners is sufficiently large. This condition is met for all scattering angles when the total kinetic energy in the centre-of-mass is well below the Coulomb barrier. Typically, this corresponds to beam energies of a few MeV/A, commonly referred to as low- and intermediate-energy Coulomb excitation. High-energy Coulomb excitation, on the other hand, is applied to processes at ultra-relativistic energies, generally around a few hundred MeV/A or more. According to [25], the states observed during low-energy Coulomb excitation must be linked to the ground state through a series of E2 or E3 transitions. This is applicable to ^{98}Rb and enables low-energy Coulomb excitation experiments to reveal new states in nuclei. Data is collected comparing the number of excited states to ground states. In addition, are transitions strength between energy levels determined by matrix elements. GOSIA, a semi-classical fitting code, is the standard tool widely used to extract these matrix elements.

The cross section of the Coulomb excitation is energy dependent. Intermediate beam energy, around 30 MeV/A and above for exotic nuclei beams, increases the cross section compared to lower energy [26]. On the other hand, it makes the excitation prone to nuclear interaction processes. For example, the strong nuclear interaction comes into play. In some cases, it is favoured to use sub-barrier-energy Coulomb excitation. Especially for higher-order indicators of shape and collectivity. The Coulomb excitation is also target-dependent. Thus, different materials show different outcomes. To calculate the cross section, a semi-classical approach is employed to overcome difficulties arising from the long-range Coulomb interaction and complex level schemes of the colliding nuclei [4], [25].

Many applications are well-suited for low-energy Coulomb excitation, and measuring transition probabilities is certainly one of them. This study aims to evaluate the matrix elements by measuring these transition probabilities. Previous work on Coulomb excitation primarily relied on measuring γ-ray yields. By measuring the reduced transition probabilities and relating them to the intrinsic quadrupole moment (Q_0), we can obtain significant results that are model-independent [24].

2.5.2 Particle spectroscopy

As previously mentioned, gamma-spectroscopy is the standard in Coulomb-excitation experiments. Yet, because of the unsuccessful experiment by [6], statement of [4] and the commissioning of LIon is the chosen method particle spectroscopy. Figure 2.8 illustrates the principle of Coulomb excitation using particle spectroscopy. This method measures the energy loss of the projectile after elastic or inelastic scattering, which is characteristic of each scattering reaction product [24].

Signal processing in particle spectroscopy is straightforward and does not require corrections. In contrast, gamma spectroscopy, which involves measuring gamma rays emitted after the de-excitation of the isomer, necessitates numerous corrections for data processing. For example, the rates of conversion electrons must be considered when using gamma spectroscopy. Additionally, when the isomer is excited, the impulse of the projectile can move the isomer's nucleus, requiring an angular correction in gamma-ray spectroscopy [19].

In particle spectroscopy, various types of projectile particles can be utilized. For instance, [27] employs alpha particles to monitor nuclear tracks for radon applications, while [28] uses protons to gain a deeper understanding of properties in certain nuclides.

This project involves particle spectroscopy by measuring protons scattered from the target to excite the ground state to the first excited state at 60 keV. Although gamma spectroscopy is more commonly used, it can be argued that the required corrections are subject to user error [19].

2.6 ^{155}Gd

2.6.1 Properties of ^{155}Gd

The isotope ^{155}Gd is stable and consists of 64 protons and 91 neutrons, categorizing it as an even-odd or odd-A nucleus. The natural abundance is 14.8%. Figure 2.9 shows the first of many levels in the isotope of Gd. The first excited state lies at 60 keV, making it a excellent candidate for investigating low-energy nuclear transitions. However, as this isotope has many levels research becomes difficult, multi-step excitation is difficult to comprehend with levels being densely packed. The first excited state with lies $\frac{5}{2}^-$ at 60 keV, it decays via a mixed M1 & E2 transition to the $\frac{3}{2}^+$ ground state. Figure 2.9 shows that the first and eighth levels only differ by 154.3409 keV. In total, ^{155}Gd has over 60 known levels [29].

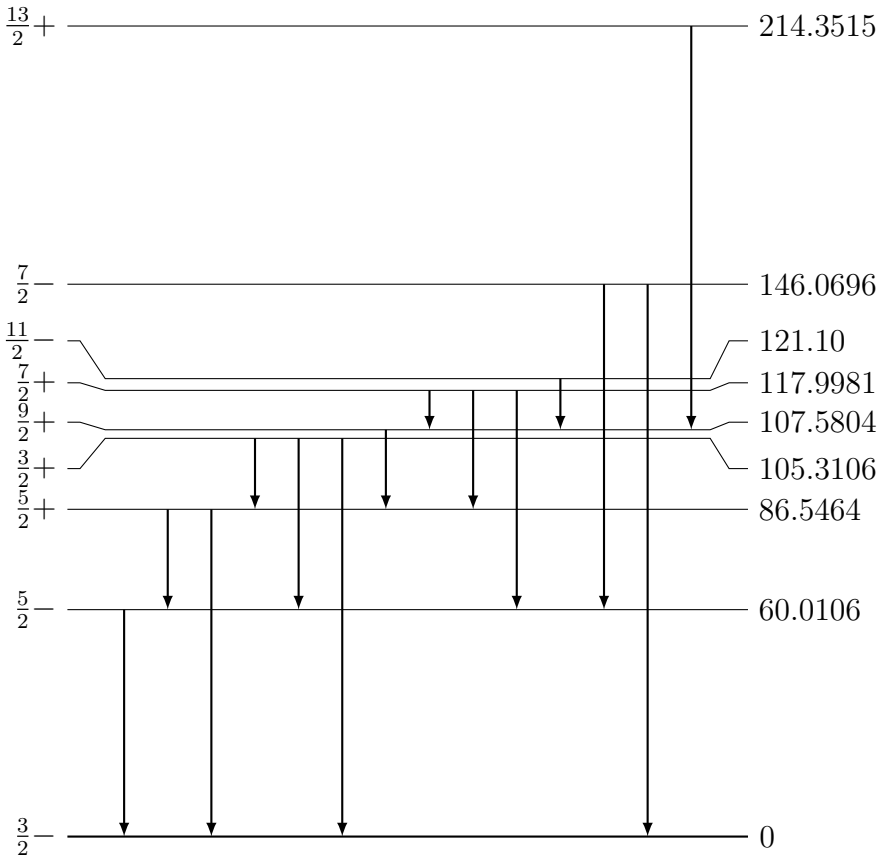

Figure 2.9: A level scheme displaying the first levels of ^{155}Gd, all the level energies depicted are in keV [29].

The ratio of measured electromagnetic transition strengths to Weisskopf units provides insight into the number of particles involved in either a single-particle or collective model. Consequently, the Weisskopf approximation serves as an indicator of nuclear deformation. Additionally, since transition strengths are related to the mean lifetime of the states, they offer valuable information in this context. The mean lifetimes of most energy states of ^{155}Gd are known, hence offer a method of comparison to experimental data. The calculations rely on the transition energy, type, and multipolarity [13].

Table 2.4 summarizes the estimates of Weisskopf Units for the first two energy levels. A higher value of the reduced transition probability, expressed in Weisskopf Units, signifies a transition that is less hindered or more probable, which is often associated with collective motion. Conversely, a lower value indicates a hindered transition [12].

Energy level transitions	Weisskopf Unit estimate
60 keV $\rightarrow$ 0 keV (E2)	2.448×10^{-6} B(E2)
60 keV $\rightarrow$ 0 keV (M1)	4.536×10^{-6} B(M1)
86 keV $\rightarrow$ 0 keV (E1)	0.1687 B(E1)
86 keV $\rightarrow$ 60 keV (E1)	5.102×10^{-2} B(E1)

Table 2.4: Calculated Weisskopf units estimates for the first two excited levels of ^{155}Gd.

Additionally, ^{155}Gd classifies as a rare-earth nuclei associated with nuclear deformation. In deformed nuclei K becomes meaningful, as ℓ and j are no longer 'good' quantum numbers. The energy levels in the deformed potential depend on the spatial orientation of the orbit. As nuclei have reflection symmetry, the components $+K$ and $-K$ will have the same energy. A Nilsson scheme, seen in Fig. 2.10, models level schemes from deformed nuclei [13].

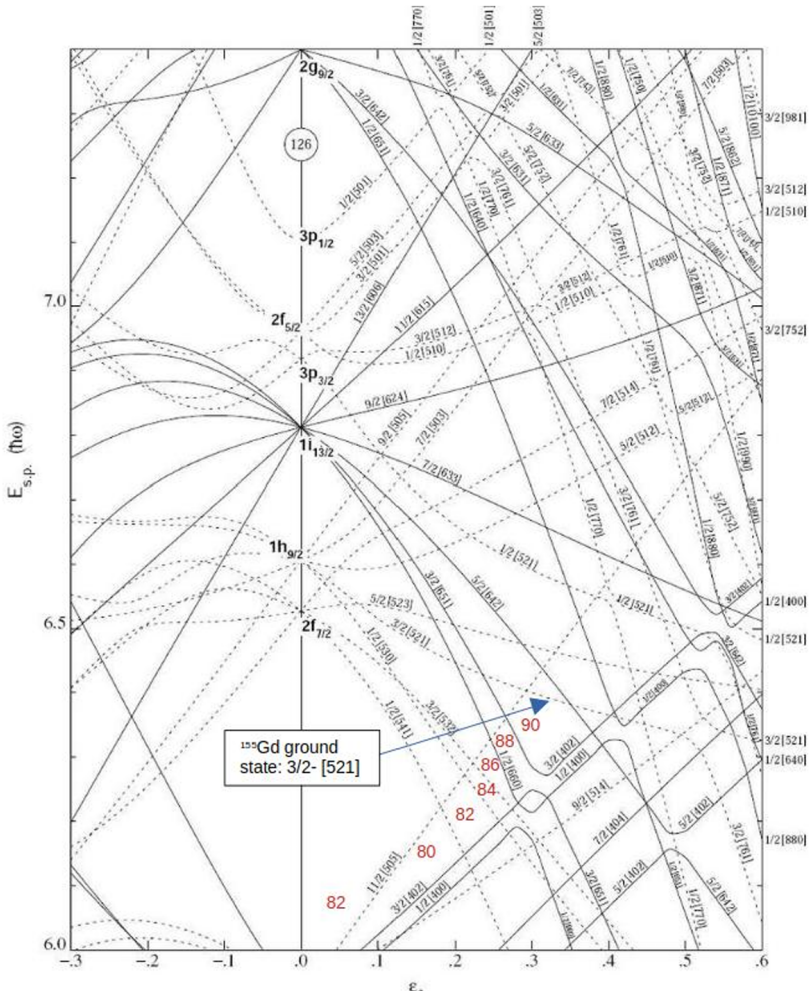

Figure 2.10: Nilsson scheme for N $\geq$ 82. The arrow is pointing to the excited state of the unpaired neutron [6].

From Fig. 2.10, the angular momentum of the ground state of a nucleus can be predicted given its e_2 value. The e_2 value, illustrated as the x-axis in Fig. 2.10, describes the degree of deformation and zero equals spherical. ^{155}Gd is prolate with $e_2 \approx 0.33$. Thus ^{155}Gd is quite deformed, enabling successful Coulomb excitation.

2.6.2 Research on ^{155}Gd

Previous research on low-energy Coulomb excitation on a ^{155}Gd target is sparse, with the motivation behind each experiment being fundamentally different. Most of the articles are from the National Nuclear Data Center (NNDC), which are reviewed by evaluators. Each article contains data about transitions strength, such as B(E2) values, useful for the NNDC to publish. Many of these articles on Coulomb excitation were published 50+ years ago to unravel nuclear structure. The newest report evaluated by the NNDC about ^{155}Gd Coulomb excitation was published in 1998 [29]. However, [30] encourages renewed interest in Coulomb excitation studies.

The nuclear reactions reported by the ENSDF datasheet are all projectile induced (in)elastically scattered. The projectile (x) after the scattering process is weakened (x') by the emission of energy by a gamma-ray, also noted as ^{155}Gd(x,x'γ). It is noted as x, since many articles use varying beam particles. The most common are a proton beam, an α-beam, and a ^{16}O beam. Even heavier particle beams are used between 1992 and 1997, such as ^{58}Ni and ^{90}Zr. To avoid nuclear reactions, the energy of the beam needs to be lower than the Coulomb barrier. The Coulomb force, explained in Eq. 2.1, is mostly dependent on Z and r. Therefore, varying energies are also used, ranging from 1.75 MeV to 390 MeV [29]. By varying the beam energy and particle type, the research focuses on many levels of the isotope ^{155}Gd.

A study by [31] in 1956 demonstrates the ability of Coulomb excitation to determine transition probabilities. This experiment uncovers previously unknown energy levels, such as the excited states at 131 keV and 145 keV in ^{155}Gd. Transition probability data from Coulomb excitation experiments are critical for validating nuclear structure models in the NNDC database.

[24] utilized an Enge split-pole spectrograph equipped with a position-sensitive detector to measure both elastic and inelastic scattering events. The experiments were conducted at a backwards scattering angle of 143°. The analysis involved determining the ratio of elastically scattered particles associated with the first and second excited states to the total number of elastically scattered particles. This ratio was then utilized, through a computer program, to extract the reduced transition probability. Notably, only 24 % of the detected states corresponded to the ground, first, or second excited states, leading to an 8 % variation in the data. This discrepancy was attributed to a large impurity of the target.

Research conducted in 1996 involved nuclear resonance fluorescence experiments on rare earth nuclei, specifically ^{155}Gd and ^{159}Tb, to investigate fragmentation in odd deformed nuclei. However, this research encountered challenges related to higher energies ($\geq$ 4 MeV) and increased E1 strength due to the influence of giant dipole resonance (GDR). This phenomenon is similar to GQR, where the entire nucleus vibrates rather than just

individual nucleons on the nuclear surface [32].

In 1998, spectroscopy on ^{155}Gd, conducted by [33], led to the discovery of states up to $23/2^-$. The Coulomb excitation of the ground state enabled accurate measurements of the B(M1) and B(E2) values. Additionally, correlating Coulomb excitation with the $3/2^+$ state, provides a direct indication to octupole correlations.

Previous research at HIAF

HIAF has been conducting Coulomb excitation studies for many years. For example, [33] calculated the g-factors of two energy levels in ^{155}Gd. Additionally, multi-step Coulomb excitation achieved the first successful measurement following the post-acceleration of an unstable isotope of a neutron-rich refractory element (^{110}Ru) by [34]. Illustrating the broad applications of Coulomb excitations and the expertise at HIAF for over 20 years.

A previous study by [6] exhibited Coulomb excitation on a ^{155}Gd target at HIAF in 2024, which yielded complex excitation patterns. Therefore, complicating efforts to construct a comprehensive level scheme and extract underlying physics information with GOSIA. The magnitude of levels and associated variables led to impossible fitting procedures. The study employed ^{16}O particles as incident particles, with multi-step excitation processes enhanced by heavier projectile masses, resulting in an abundance of energy levels. To address this problem, it is proposed to use lighter incident particles for Coulomb excitation, which should produce fewer excitations and simplify the resulting spectrum [4].

Furthermore, [6] used the Compton Suppressed Array (CAESAR) available at HIAF. The vital difference between CAESAR and LIon lies in the scattering angles: CAESAR measures the back-scattering angles, while LIon is not limited to this. A bigger scattering angle, such as backwards scattering, creates more multi-step excitation [4]. This work and the LIon detector try to limit the amount of multi-step excitation, therefore choosing smaller scattering angles.

In this study, employing ^{155}Gd helps validate the low-energy Coulomb-excitation model for nuclei with more complex structures and lower excitation energies and the properties of ^{155}Gd. This study uses a proton beam to promote low-level excitation and limit multi-step excitation. By this process, building a foundation of matrix elements of ^{155}Gd. This work contributes to the understanding of nuclear behaviour in systems that are far from closed shells and is a follow-up study of [6]. These insights are particularly important for future research on energy storage applications using isomeric states.

Chapter 3

Instrumentation

Chapter 3 provides a detailed explanation of the main components involved in this experiment: the detector, which was specifically designed and manufactured at HIAF for these applications. The chapter thoroughly describes all the functional parts that enable particle identification.

Next, the focus shifts to GEANT4, a Monte Carlo toolkit developed by CERN. A simulation of the detector is created to analyse its behaviour under various conditions. It is essential to take this step in order to understand the detector's performance at lower energy levels. Finally, this simulation is tested and benchmarked against two data sets: a year-old run and a triple alpha source. These comparisons help to quantify the output of the detector and evaluate it against the simulated data.

3.1 LIon

The LIon detector was specifically engineered at HIAF for precision measurements of light ions produced in nuclear reactions by the particle spectroscopy group. It is a gas-filled detector, typically 200 Torr isobutane, which leverages isobutane's high stopping-power-to-pressure ratio to minimize casing thickness while also reducing multiple scattering with its low effective atomic number [35]. The pressure inside LIon is selected to achieve high reaction yields in the gas and to distinguish between heavy and light ions [36]. The detector is to be paired with the Enge spectrometer, therefore requiring a method to identify particles with identical magnetic rigidity. Figure 3.1 shows a side view of the Light Ion detector, the top plate is the window for particles to enter. While Fig. 3.2 outlines all the functioning components of the LIon detector.

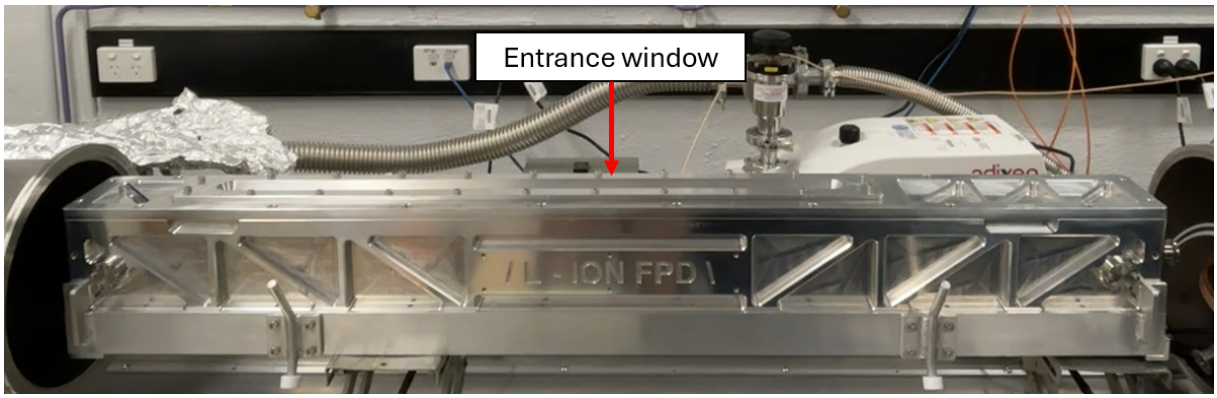

Figure 3.1: A frontal side view of the Light Ion detector in the test setup. The entrance window of the detector at the top indicated by an arrow.

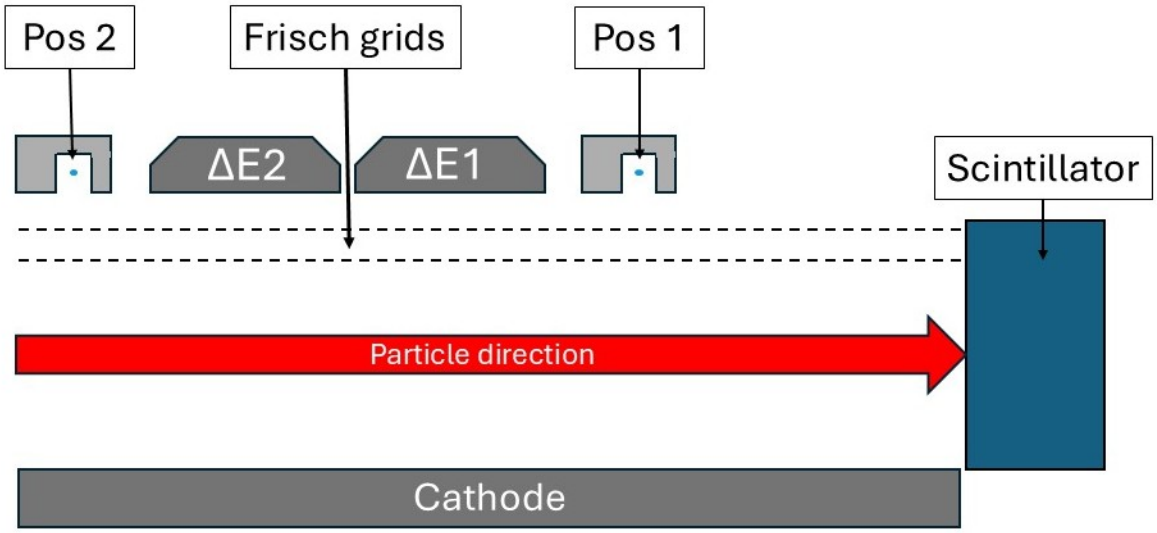

Figure 3.2: A cut-through of all the components inside the LIon detector.

A plastic scintillator is present to capture the residual energy of ions as they exit the gas counter. Each collision with the scintillator produces a light signal, which is collected by silicon photomultipliers (SiPM) [35]. SiPMs are able to detect single photons by micro-cells avalanche detectors and thus are smaller than standard conventional photomultiplier tubes, enabling high-resolution photon counting for precise low-light applications [37]. The LIon

system is designed to ensure that all particles come to a stop within the scintillator. It is constructed from plastic vinyltoluene and measures 85.8 cm, 2.66 cm, and 1.71 cm along the x, y, and z-axes, respectively. Plastic vinyltoluene (BC-404) was chosen due to its fast timing response of 1.8 ns decay time, which suits coincidence-timing signal processing with the other signals received for an event [38]. Its x-axis needs to be large, as the magnetic rigidity of the Enge will enforce two locations on the focal plane.

Two metal bars often referred to as the anodes, shown as 'ΔE1' and 'ΔE2' in Fig. 3.2 measure the rate of energy loss by the incident particle in the detector gas. A Frisch grid, consisting of two wires, is shown in Fig. 3.2 as two dotted lines that span the entire z-axis of the detector. The upper wire has a voltage of 200 volts, whereas the lower is neutral. A cathode is also present, which has a negative voltage of -600 volts. Particles traversing through the detector will decelerate and create electron-ion pairs. These secondary electrons will be accelerated towards the positively charged Frisch grid, while the negatively charged cathode will attract the ions. The metal bars, including the cathode, are individually connected to a charge sensitive preamp that allows reading out the charge of the particles.

To obtain position and angle sensitive data, LIon uses two resistive wires, made out of carbon-coated quartz with a resistance of 1700 Ω/mm. These wires are displayed on Fig. 3.2 as 'Pos 1' and 'Pos 2' and are detained in the metal slits running throughout the whole x-axis of the detector. The movement of the electrons up until the Frisch grid is identical to the anodes. After this point, the electrons will be accelerated again towards the resistive wires containing 2500 V. This creates an electron avalanche towards the high-voltage resistive wire, with the amplitude of the avalanche directly proportional to the number of electron-ion pairs generated in that region. A relation between the charge (C) of these electrons and the position is made with:

$$\frac{\mathrm{d}^2V}{\mathrm{d}x^2} - \mathrm{R}_0\mathrm{C}_0\frac{\mathrm{d}V}{\mathrm{d}t} = 0. \tag{3.1}$$

It should be noted that the position resolution is sensitive to the voltage (V) applied to the resistance (R) of the wires. As the voltage is increased, the resolution improves because of better signal to noise ratio. LIon operates at a voltage of 2500 V. A similar focal plane detector, which LIon is modeled after, obtained a position resolution of approximately 1.2 mm for 20 MeV protons [36].

The combined analysis of total energy deposition, energy loss in the gas volume, and spatial/angular trajectory measurements enables particle identification. Further on, spectra of different excited states compared to the ground state should be clearly observable. The ratio of the first excited state to the ground state is essential information obtained from LIon.

3.2 GEANT4 simulation

A key part of this thesis is to create a simulation of LIon using GEANT4. With this comprehensive simulation, the output and efficiency of the detector can be theoretically tested. The GEANT4 simulation was modeled and compared to a the real model, seen in Fig 3.1.

GEANT4 is a toolkit written in C++ to simulate the passage of particles through matter. It includes a comprehensive range of physics including electromagnetic, hadronic and optical processes, a large set of long-lived particles, materials and elements over a wide range of energies. The 'G4EmStandardPhysics_Option4' physics list was selected to implement a lower energy cut-off of a few eV for electromagnetic processes. The program is made to simulate the behaviour of various ions passing through the detector, where energy deposition or hits can be stored. The output of the simulation will be generated and analyzed in ROOT [10]. ROOT is also a C++ framework and is designed to analyze petabytes of data in an efficient way. Both are created by CERN [39].

The GEANT4 model uses all real-life geometries and functioning structures from the LIon detector. This includes two position-sensitive wires, two anodes, a cathode and a scintillator. Nevertheless, the model lacks an avalanche detector, as GEANT4 does not offer such applications. For that kind of measurements, other simulation software are more applicable [10]. Since the detector is made out of varying sensitive parts, the GEANT4 model comprises volumes with sensitive detector classes. It also includes the Mylar window and the Aluminized Mylar wrapping of the scintillator, as they both have an impact on the beampath. Figure 3.3 shows the final GEANT4 model made out of sensitive boxes without casing.

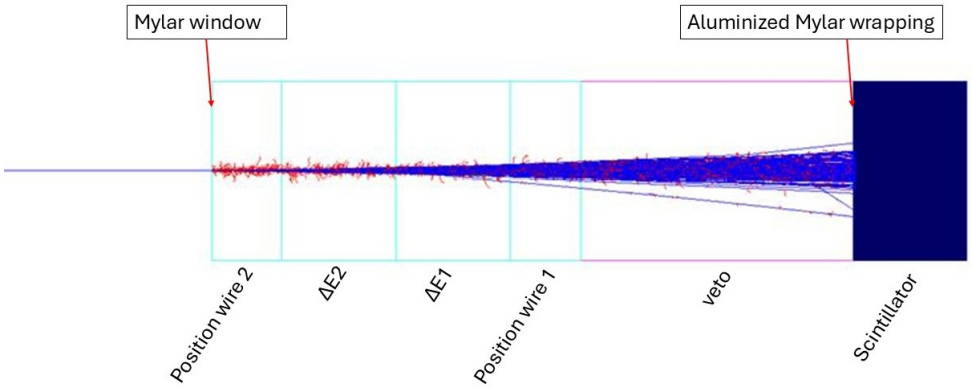

Figure 3.3: A lateral view of the GEANT4 model of LIon without casing, to view the interaction with the beam of each volume. The beam entering the detector volumes consists out of 10 MeV protons. The volumes from left to right: Mylar window, Pos 2, ΔE2, ΔE1, Pos 1, Aluminized Mylar wrapping, scintillator.

In GEANT4, all types of particles are color-coded. Within Fig. 3.3 the protons are blue, the electrons are red, and γ-rays are green. To make it more realistic, the entrance into the LION detector is angled by 45 degrees [10]. Changing the angle, will make the path longer, thus more energy deposition in the gas volume [12]. The entrance angle of LIon is fixed, while the Enge spectrograph can rotate to create different scattering angles [36]. Figure 3.4 illustrates an angled view of 10 MeV protons entering the detector with cosmetic casing.

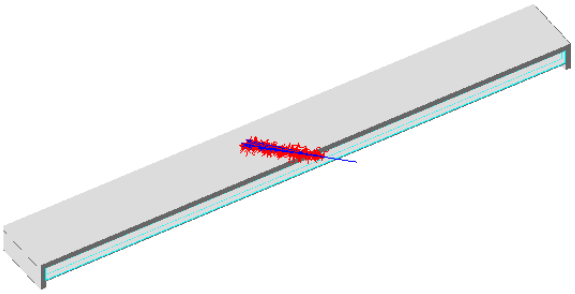

Figure 3.4: A angled view of the final GEANT4 model of LIon with casing, a 10 MeV proton beam enters the detector.

The simulation measures the energy deposited by each beam particle and outputs this value, which is stored in a ROOT file for each volume. The physical phenomena occurring inside the LIon detector are far more complex. When a particle enters the gas volume of the detector, it can interact with the gas molecules. If the particle's energy is high enough and the probability allows for a reaction, a gas molecule may be ionized by the beam particle, resulting in the formation of an electron-ion pair. The electron and ion are then attracted to electrodes of opposite charge, where their signals are read out by a preamplifier. The difference in processes can create a difference in output.

Each volume records deposited energy; the amount depends on the beam energy, the type of beam particle, and the surrounding material. To demonstrate the detector's response to charged particles, 10 MeV protons were chosen. Figure 3.5 shows the output of the scintillator in ROOT.

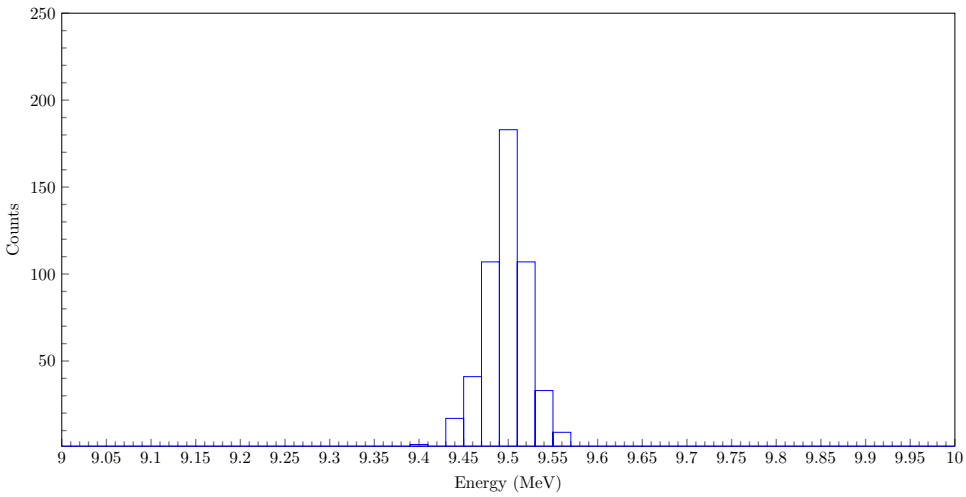

Figure 3.5: Energy deposition histogram of the scintillator with 10 MeV protons.

With 500 entries of 10 MeV protons, the energy deposition in the scintillator is $\approx$ 8 MeV, implying a $\approx$ 2 MeV energy loss in the gas volume. The standard deviation is small, at just 0.06962. Figure 3.6 shows the energy deposition for each volume for 10 MeV protons in the GEANT4 model in orange. Please note that the energy deposition in the scintillator is not included in the graph because it would make the entire visual unreadable. Since charged particles deposit most of their energy at the path's endpoint due to the Bragg peak, causing most of the beam energy to be deposited at the end of the detector [12].

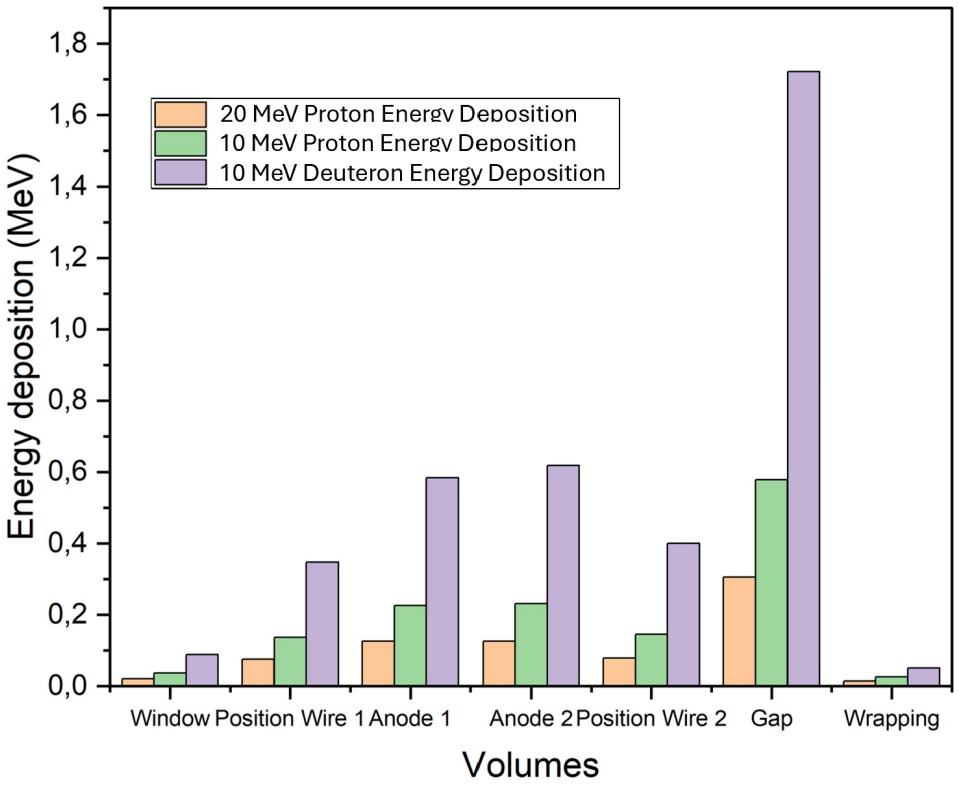

Figure 3.6: A histogram to compare the mean energy deposition of 500 entries in all volumes in the detector for different particles and energies. The standard particle is the 10 MeV proton in orange, with a higher energy proton (20 MeV) in blue. Different particle types with the same energy display in grey as 10 MeV deuterons.

Figure 3.6 illustrates the energy deposition of a 20 MeV proton beam in blue. Higher energy levels result in energy deposition occurring further into the material. This will also effect the Linear Energy Transfer (LET), which indicates the amount of energy deposition throughout its track. The higher energy protons have a lower LET, causing most of the energy of the 20 MeV protons to be deposited in the scintillator at the back. In comparison with 10 MeV protons, the energy deposition of the 20 MeV protons is halved.

Another example is the difference between particles. Protons are light particles, which means their travel is not significantly hindered. In contrast, the travel of a deuteron, a heavier particle, is more affected. Figure 3.6 illustrates the energy deposition of 10 MeV deuterons in purple. The proportion of each volume appears to be consistent, but the volumes experience significantly greater energy deposition indicating a higher LET value for deuterons. A deuteron induces a substantially higher energy release throughout its track compared to a proton [13]. So significant, that 5 MeV deuterons are unable to reach the scintillator, while 5 MeV protons can.

3.3 Simulation benchmarking

Benchmarking the output of the simulation against empirical data is a crucial step in validating the GEANT4 model. The benchmark involves using data extracted a year prior (test one) and one triple α-source (test two) to verify detector output agreement. The first test evaluates heavy-ion penetration depth, while the second assesses gas density effects on ionization.

The data from these tests are uncalibrated. In principle, if it is assumed that the particle beam does not reach the scintillator and that all energy deposition occurs in the cathode, calibration would be possible. This assumption is supported by SRIM calculations for a ^{16}O beam at 50 MeV or 70 MeV, which indicate that the beam does not reach the scintillator. SRIM, or Stopping and Range of Ions in Matter, is a program that calculates the energy loss of ions as they pass through matter [40]. Table 3.1 shows the results of the SRIM calculation.

Projected range	Longitudinal straggling	Lateral straggling
113.78 mm	4 mm	832.38 μm

Table 3.1: The calculation of SRIM for a 70 MeV ^{16}O beam in isobutane with a gas density of 6.8×10^{-4} g/cm^3.

The calculation shows that the beam will not reach the scintillator, most of its energy will be deposited in second position wire volume. However, mechanical and physics modeling limitations prevent calibration:

- A coupling between the anodes and position wires causes repetitive reading of the same signal. The high charge from the position wires is significantly high, which enables cross-talk between position wires and anodes.
- GEANT4 lacks avalanche physics modeling, so simulated position wire measurements are rendered inaccurate. Energy deposition profiles do not replicate or match avalanche-mediated signals.

Consequently, the data remains uncalibrated and cannot be used for quantitative analysis. Moreover, measurements of the position wires are highly sensitive to the detector gain. The data from the scintillator permits relative analysis. Nevertheless, the simulation provides more detailed insight of energy depositions in the detector, which enables the distinction of different particles based upon their track length.

3.3.1 Test one

Setup

Between August 2024 and September 2024 conducted the particle spectroscopy team an experiment at HIAF, first involving a 50 MeV ^{16}O beam onto a 200 μg/cm^2 thick ^{197}Au target and later on changing the energy to 70 MeV. The test continued in September 2024 with a beam of 10 MeV deuterons. Measurements of the reaction products were emitted through a combination of the Enge spectrograph and LIon at beamline 5. The data from this experiment was sorted by the PIXIE system into ROOT files.

Energy deposition of ^{16}O beams

In the experiments, two different energy levels were tested for the ^{16}O particle beams: 50 MeV and 70 MeV. The initial tests with the 50 MeV beam indicated that it was too heavy to reach the scintillator, leading to no data being collected. Consequently, both histograms lacked data, rendering the uncalibrated experimental results unusable. The simulation conducted in GEANT4 provided insights into energy deposition across various volumes, showing that the particle beam did not interact with the scintillator, and revealed the precise stopping position of the particles. Figure 3.7 shows the LIon simulation with a 50 MeV ^{16}0 beam entering.

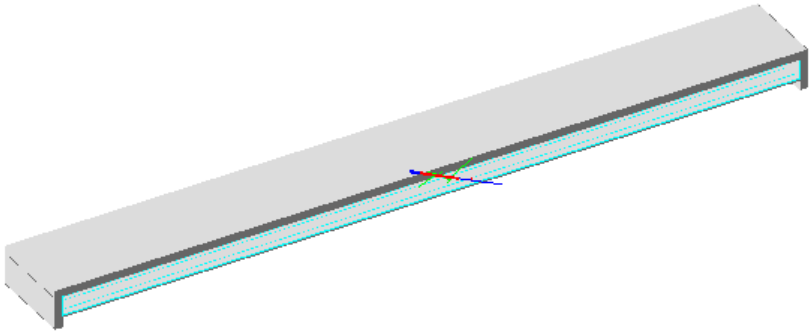

Figure 3.7: GEANT4 simulation with a 50 MeV ^{16}0 beam entering LIon.

The majority of energy deposition occurs in Position Wire 2, indicating that the Bragg peak occurs at this location. Minor energy deposition is also observed in the second anode. The GEANT4 models enable all volumes to be sensitive, providing deeper insight into the total deposition locations. Additionally, a significant amount of energy ($\approx$ 7 MeV) is lost in the window.

Subsequently to enhance penetration depth, was the beam energy increased to 70 MeV. Despite this adjustment, continued the particles to fail to reach the scintillator, as depicted in Fig. 3.8, which shows the particle beam disintegrating before reaching the scintillator. The 70 MeV beam achieves deeper penetration compared to the 50 MeV beam, resulting in most energy being deposited near the second anode. The higher-energy beam also loses less energy through the window.

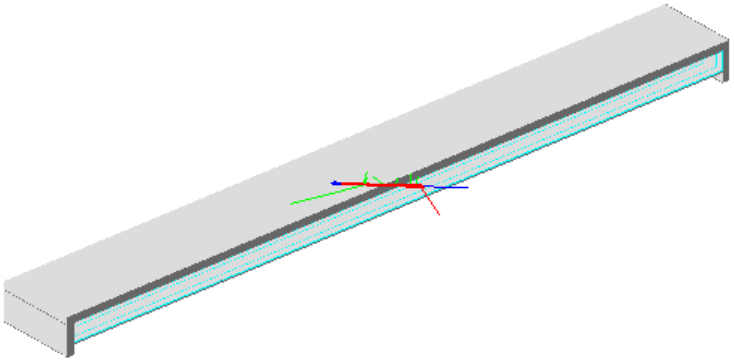

Figure 3.8: GEANT4 simulation of a 70 MeV ^{16}O beam entering LIon.

The 70 MeV beam penetrates deeper in the gas volume compared to the 50 MeV beam. Additionally, Fig. 3.8 illustrates a significant amount of gamma radiation emitted from the oxygen beam. Fig 3.9 compares the energy deposition in all sensitive volumes from both simulations.

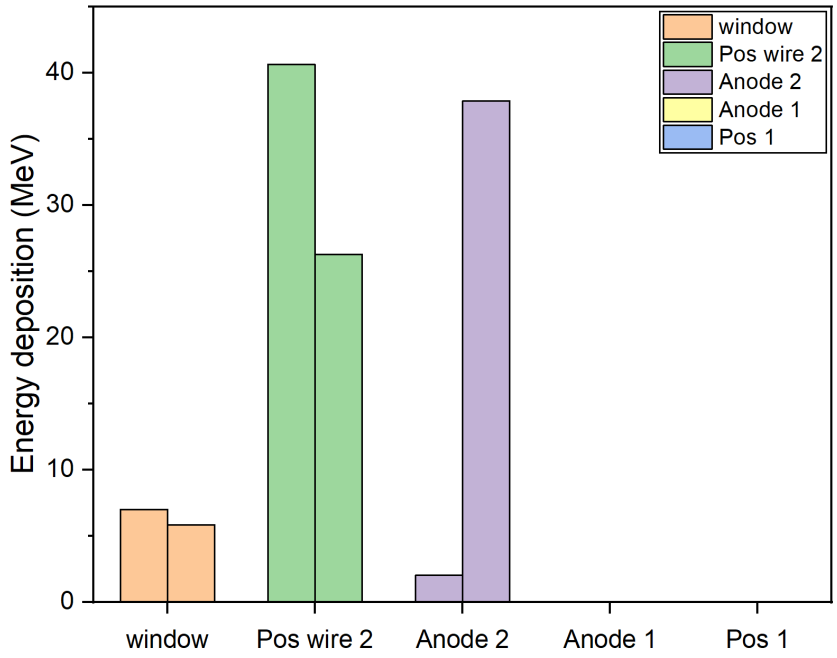

Figure 3.9: A histogram to compare the average energy deposition of 500 entries with 50 and 70 MeV ^{16}O beam in GEANT4. The left bar is the 50 MeV ^{16}O while the right bar is the 70 MeV variant. Anode 1 and Position wire 1 are empty.

The 50 MeV beam primarily deposits its energy within the second position wire volume, whereas the 70 MeV beam penetrates deeper into the detector volume, depositing most of its energy near the second anode. Notably, the higher-energy beam loses less energy into the window. Both phenomena are explained by Bragg peak behavior, where charged particles exhibit energy deposition peaks at characteristic depths determined by their initial kinetic energy [12].

A 10 MeV deuteron beam

A later test conducted by the nuclear structure group in September 2024 involved a beam of 10 MeV deuterons directed at the same target as the previous test. In the previous test, did the particles not reach the scintillator, due to too low energy with high mass. Deuterons and protons have lower mass than ^{16}O ions, and although a lower beam energy is used, these lighter particles are able to reach the scintillator. Due to technical limitations, only scintillator data is available for analysis in this test. Figure 3.10 shows the beam track from the simulation of a 10 MeV deuteron beam entering LIon.

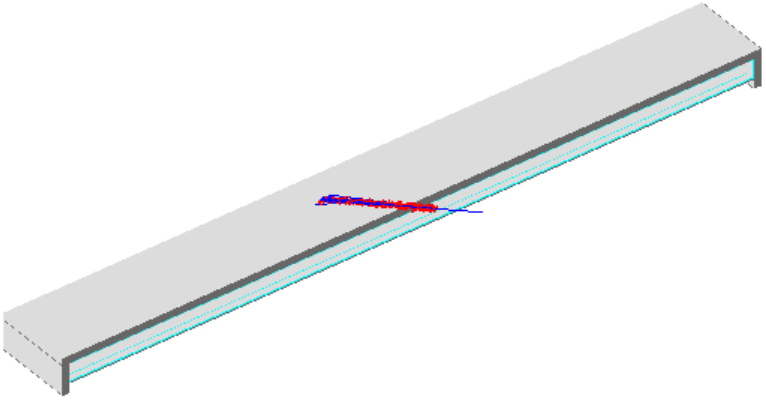

Figure 3.10: GEANT4 simulation of a 10 MeV deuteron beam into LIon.

The data from this experiment generates a spectrum in ROOT as seen in Fig. 3.11. A peak is shown at 10 MeV with 92,120 entries present. However, do note that the data is uncalibrated, thus the energy units are arbitrary.

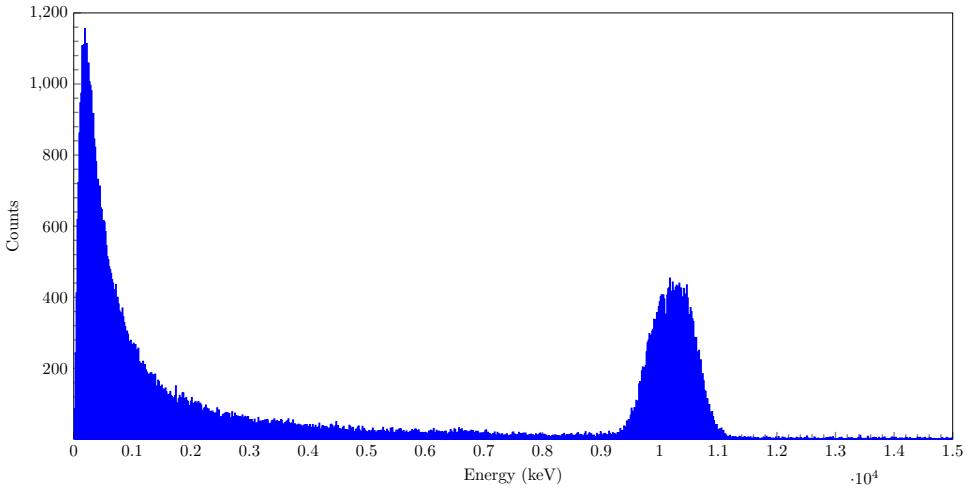

Figure 3.11: A histogram made in ROOT from experimental data with 10 MeV deuterons entering LIon's scintillator.

This peak is explained by the elastic scattering from the deuterons, hence its high energy. There is a high tail present at lower energies caused by inelastic scattering. In addition, the high peak around 50 keV is irrelevant. A (d,p) reaction within the target is not plausible, as the energy from the beam is below the Coulomb barrier. To compare the energy deposition between experimental and simulation data, a histogram, shown in Fig. 3.12 is made with the 10 MeV deuterons in GEANT4.

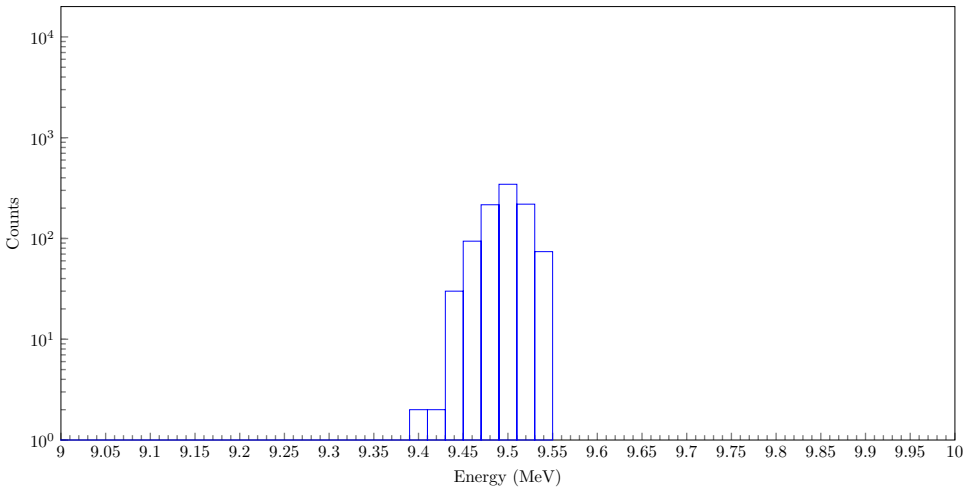

Figure 3.12: A histogram made in ROOT from simulation data with 10 MeV deuterons entering LIon's scintillator.

The GEANT4 model simulates the entry of a deuteron without a target present. Thus, is it impossible for the simulation to differentiate elastic and inelastic scattering from the target. Figure 3.12 shows a peak at ≈ 9,5 Mev. Since the data in the experiment is uncalibrated, a comparison between energy level in the scintillator is unfeasible.

3.3.2 Test two

Setup

The second test was conducted on April 30th in the particle spectroscopy team's test laboratory. LIon was placed inside a test chamber under vacuum conditions. The test included a triple α-source, tagged as 'ANU 120', containing ^{239}Pu, ^{241}Am, and ^{244}Cm.

The isotope ^{239}Pu has a half-life of 24 $\times 10^4$ years and its most common alpha energy is 5.156 MeV. The second isotope, ^{241}Am, has a half-life of 4.32 $\times 10^2$ years and an alpha energy of 5.4857 MeV. Finally, the isotope ^{244}Cm has a half-life of 18.1 years and an alpha energy of 5.8048 MeV. The triple α-source came into the office first around August 2005. To simulate this source, three independent α-beams are produced in GEANT4, with an energy of 5.156 MeV, 5.4857 MeV, and 5.8048 MeV.

The position of the triple α-source was adjusted using magnets located on both sides of the test chamber. For this particular test, the α-source was centered in the middle of the chamber. Figure 3.13 illustrates the setup for this test.

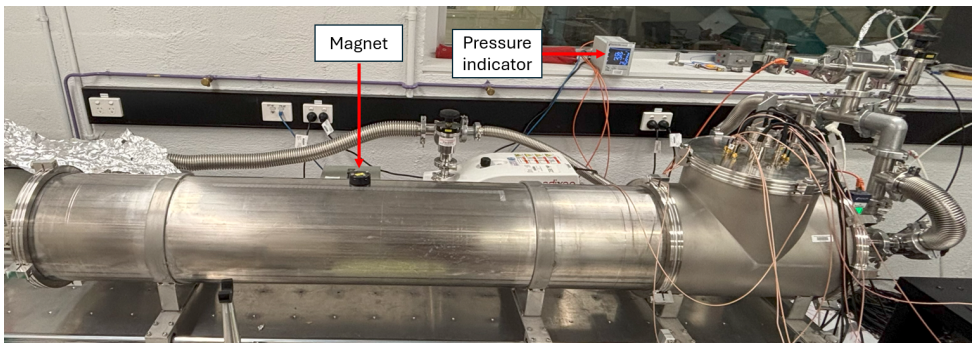

Figure 3.13: The setup of the test chamber of the particle spectroscopy team with LIon inside. The test chamber is at vacuum pressure, and the magnet on top indicates the placement of the α-source.

During the experiment, the cathode and two anodes were connected, but the position wires and scintillator were left unconnected. The position wires were turned off as they can spark when charged at lower densities. Additionally, the scintillator was not used since α-particles cannot pass through the Aluminized Mylar wrapping.

The triple α-source

The test involved varying the isobutane gas density to observe its effect on the particle track of the alpha source. Measurements began at 100 Torr and increased in $\approx$ 20 Torr increments up to 200 Torr, resulting in five measurements. Each measurement lasted five minutes, and density was monitored with a vacuum gauge. Throughout the test, the position of the source was fixed. However, the α-source is uncollimated and emits particles throughout the entire detector, meaning that some particle tracks are longer than others depending on their entrance angle.

In theory, an increase in density should enhance the ionization of the beam, leading to greater energy deposition within the volumes. However, a higher density also results in increased stopping power, which subsequently reduces the particle's trajectory within the detector. Figure 3.14 presents the data from the experiment.

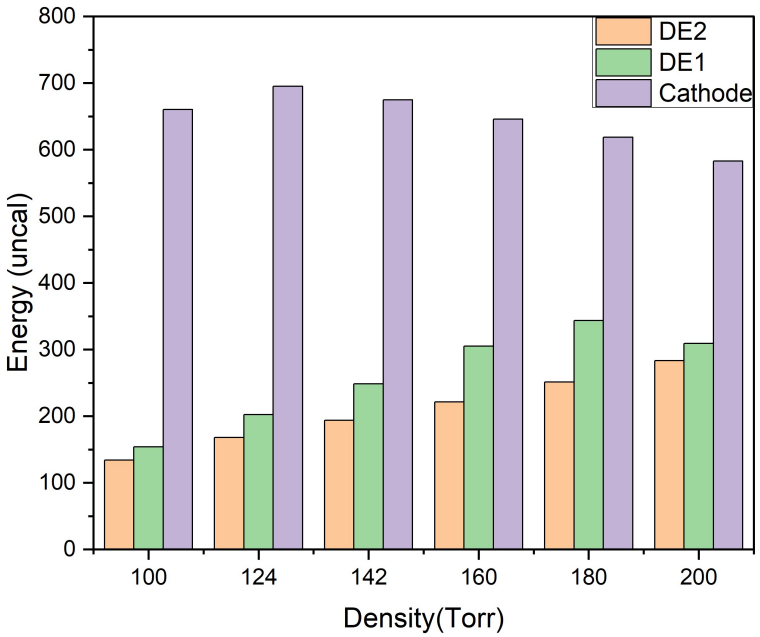

Figure 3.14: A average energy deposition of different gas densities with the triple α-source.

The second anode, $\Delta E2$, demonstrates a linear trend, indicating that a higher density is associated with increased ionization in the gas. The first anode, $\Delta E1$, follows a similar trend until the highest density is reached. While greater density results in more ionization, it also obstructs the particles, which leads to a shift in the Bragg peak and a reduction in the particle track. The placement of anode 2 is unfortunate for this triple α-source, as the Bragg peak moves away from it. The cathode initially shows an increase in response, followed by a decrease. Despite this fluctuation, the overall energy deposit remains constant. A small discrepancy in the average readings can be attributed to two factors. First, there may be a dead zone at the front of the detector. Second, charge recombination can occur, where charged particles revert to uncharged particles, resulting in a lack of attraction to the cathode.

Figure 3.15 shows the model with the alpha source in GEANT4. The simulation depicts the beam entering the gas volume, yet not making it far in the gas volume.

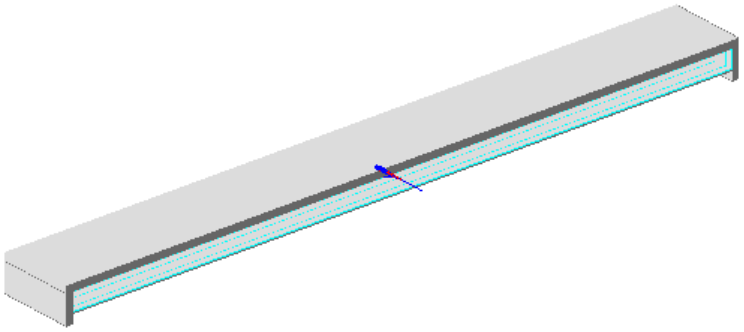

Figure 3.15: GEANT4 simulation of a the triple alpha source beam into LIon. The entrance into the detector is not angled as the magnet indicating the source is in de middle of the detector.

A simulation is conducted using GEANT4 at the same pressures previously mentioned. Since GEANT4 does not accept inputs in Torr, are values converted into atmospheres (atm), which are then used to calculate density with the ideal gas law. The results are obtained from both the anodes and cathode, with each simulation involving 1,000 entries. Figure 3.16 illustrates a histogram that is almost identical to the experimental data.

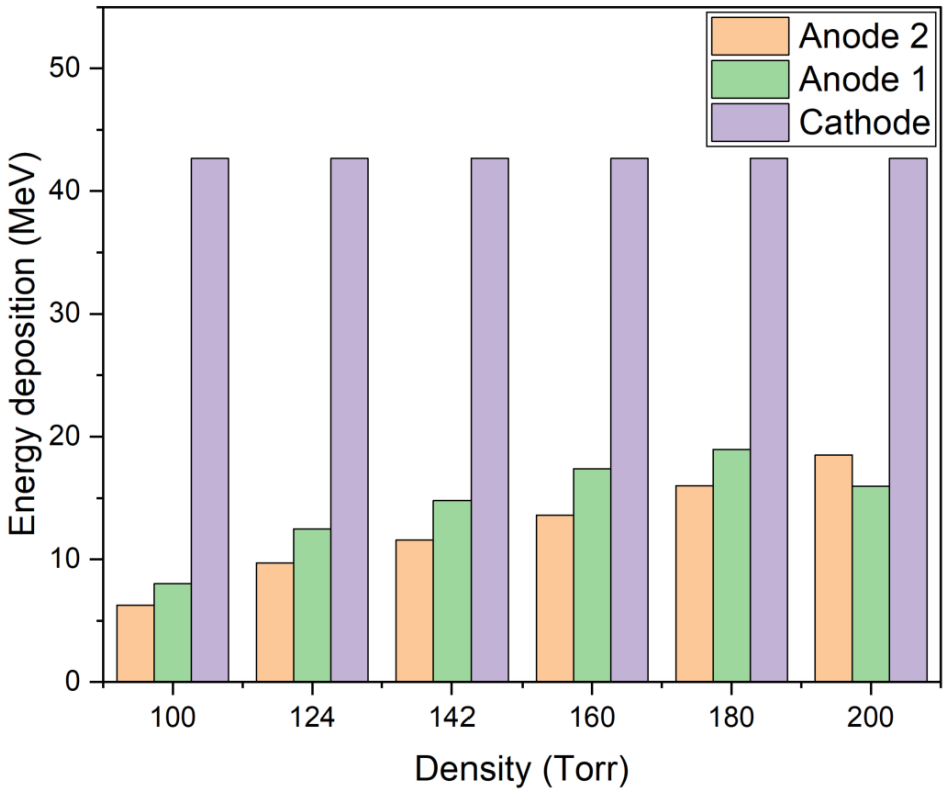

Figure 3.16: A histogram to compare the average energy deposition of different gas densities with the triple α-source accumulated in a simulation.

The simulation data shows linear growth for the anodes, which is consistent with the experimental data. Even the decrease of anode 1 in the final measurement is replicated in the simulation. The amount of energy deposition in the cathode is more stable in the simulation, yet both remain at the same level throughout the experiment.

3.3.3 Conclusion

Test one

Test one demonstrates strong agreement between experimental and simulation results, as neither 50 MeV nor 70 MeV ^{16}O particles reach the scintillator in either case. Variations in beam energy produce distinct depth profiles, with higher-energy beams (70 MeV) depositing energy at greater depths than lower-energy beams (50 MeV). This energy-depth relationship is consistent with Bragg peak phenomena.

Furthermore, the deuterons test shows agreement in the elastic scatter peak. The inelastic scatter peak, caused by collision with the ^{197}Au target, is impossible to simulate since there is no target present in the simulation. Since the data from the experiment is uncalibrated, there is no method to check the agreement in energy in the scintillator.

Test two

The results of the second test indicate a strong overall agreement between the simulation and the experimental data. The first anode displays an increase in measurements until the final point, where a decrease is observed at 200 Torr. In contrast, the second anode shows a consistent overall increase. Both the simulation and the experimental cathodes remain stable throughout the experiment.

Particle track

The results from both tests are shown in Table 3.2, which illustrates the differences in particle tracks between experimental data and GEANT4. There is a strong agreement on the designated location between the two methods.

Particle	Energy	Reaches in simulation	Reaches in experiment
Oxygen	50 MeV	Position wire 2	undetermined
Oxygen	70 MeV	Anode 2	undetermined
Deuterons	10 MeV	Scintillator	Scintillator
Triple $\alpha-$source	Average of 5.48 MeV	Anode 1	Anode 1

Table 3.2: The differences in track length between GEANT4 and experimental data.

Chapter 4

Coulomb-excitation setup

Chapter 4 provides a detailed explanation of the materials used in this experiment. The goal is to successfully identify the level of interest in the spectra of Coulomb excitation onto a ^{155}Gd target. Extracting the counts in the peak of interest is a crucial step in extracting the matrix elements with GOSIA.

Particles are produced and targeted by a tandem accelerator towards a target. Afterward, the particles are scattered off the target, and the Enge spectrometer focuses the particles onto the detector's focal plane.

The conditions of the test are broadly explained in this chapter. Choosing the correct beam energy and scattering angle is critical in achieving this common goal. Coulomb excitation requires a low energy to restrict the nuclear reactions. Excitation probabilities are calculated with GOSIA to choose the highest excitation probability possible. This seemed trickier than expected, since higher beam energies or scattering angles provide a higher probability of the 60 keV level, yet higher lying states profoundly excite more energy states. A correct balance needs to be found in this process. The required time for each different beam energy and scattering angle is also stated here.

4.1 Particle accelerator

The first particle accelerator was developed in 1927 by Wideröe, which accelerated sodium ions [41]. As of now, a wide range of particles have been accelerated, such as; electrons, positrons, protons, antiprotons, and heavy ions. Accelerators serve a multitude of motivations in general physics. Specifically, in nuclear physics, do accelerators provide great opportunities of investigating the nuclear structure away from the stable nuclei [21]. At the moment, the heaviest and largest accelerator is at CERN. Accelerators have seen many forms, for instance, drift tube, cyclotrons, etc. [41]. The HIAF facility has an FN tandem Van der Graaff accelerator. Which consists of a Van der Graaff accelerator combined with a boost accelerator. The basic principle of a Van der Graaff generator is seen in Figure 4.1 [42].

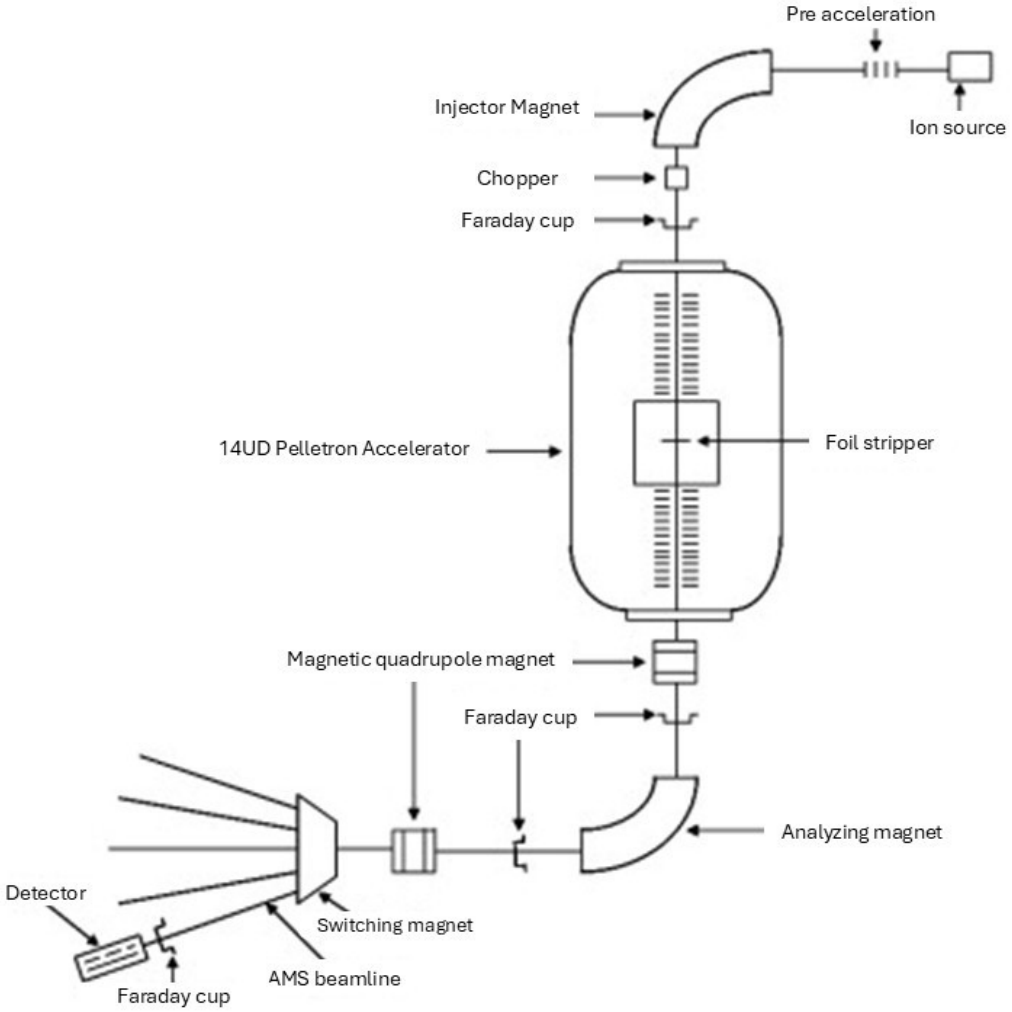

Figure 4.1: Figure to show the working principle of a Van der Graaff accelerator [42].

A Van der Graaff particle generator exploits Coulomb's law by placing a large metal surface with opposite sign near a charged particle, consequently are the charged particles attracted and accelerated towards the metal surface. This type of generator uses a chain to carry charge into the high voltage terminal until it reaches a potential of several MV. Furthermore, this group of generators has shown to be a useful source for low-energy particles, given its operating range is around 2 – 5 MV [43].

The tandem Van der Graaff accelerator employs a two-stage acceleration process, enabling the placement of the ion source outside the high-voltage terminal. This configuration significantly enhances accessibility and maintenance of the ion source. The ion source provides singly charged negative ions, such as; H^-, He^- or $^{16}O^-$. These charged ions get accelerated towards the positively charged terminal, where they will pass a stripper to remove two or more electrons. The particles are now positively charged and gain a final second acceleration [12]. Essentially, to avoid issues, such as colliding with atoms in air or slamming into the dome, it is crucial to use a vacuum tube for less beam deviation [43]. However, the particles will not be isotopically or chemically pure, an analyzing magnet with the correct strength is introduced to filter the wanted particles. Thus delivering a beam of energetic-identical protons [44]. A Faraday cup is installed in multiple places to measure the current of the charged particle beam. The Faraday cup will measure the current, indicating the correct strength of the analyzing magnet. The HIAF facility, shown in Fig. 4.2, hosts its own 15-million-volt 14UD tandem Van der Graaff accelerator, with a 6 million Volt-equivalent superconducting linear accelerator booster.

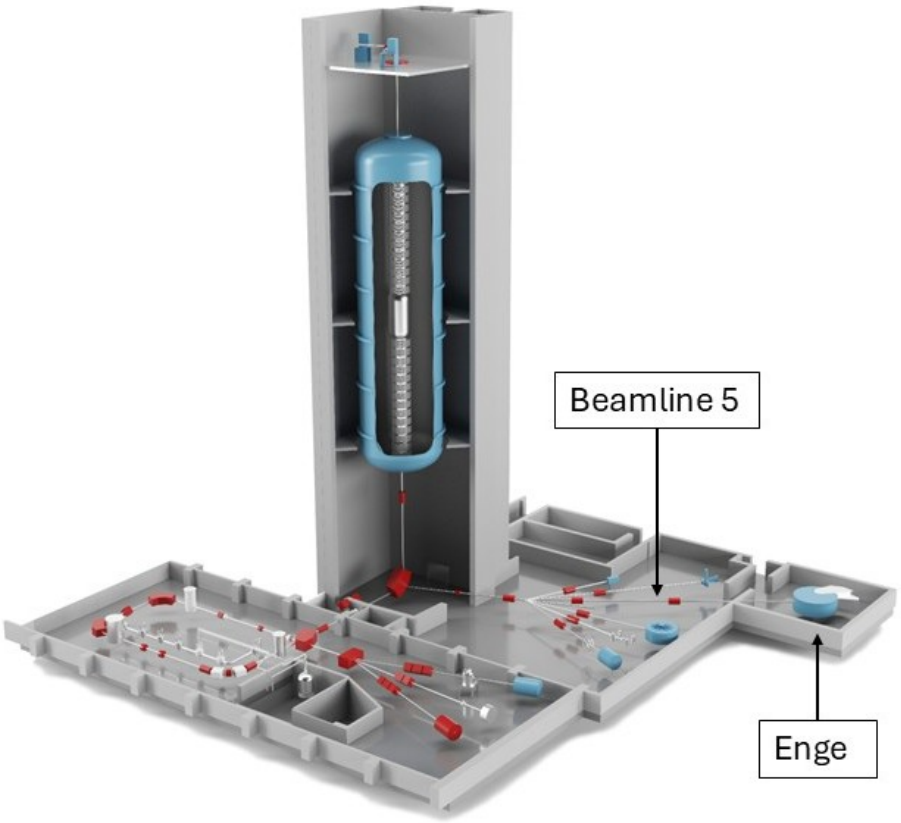

Figure 4.2: A structured view of the HIAF facility with all its beam lines.

This project involves using HIAF's tandem accelerator with beamline 5 to accelerate protons into the Enge and LIon. To produce protons the ion source will generate H^- particles, which will be accelerated towards the target. Subsequently, the stripper neutralizes the H-atom creating protons. The energy of the protons will be discussed in section 4.5.

4.2 Target

Natural gadolinium consists of a mixture of several stable isotopes, and is generally around 14.8% ^{155}Gd [45]. To get predominantly ^{155}Gd, an enriched target is obligatory. The final target, Gd_2O_3 in a solid form, was enriched to 90.53% of ^{155}Gd. However still trace amounts of other isotopes are present; a full breakdown of the isotopes present in the target is visible in Table 4.1. Isotopes present lower than 0.01% are not mentioned [46].

Isotope	Natural abundance	Abundance in target
^{152}Gd	0.20%	0.01%
^{154}Gd	2.18%	0.26%
^{155}Gd	14.8%	90.53%
^{156}Gd	20.47%	6.73%
^{157}Gd	15.65%	1.11%
^{158}Gd	24.84%	0.95%
^{160}Gd	21.86%	0.41%

Table 4.1: The natural abundance of the stable gadolinium isotopes, in addition to the composition of the target used in the Coulomb-excitation experiment.

High-resolution Coulomb excitation requires thin targets. Thicker targets lead to significant energy straggling. Hence thin targets are desired to perform high-resolution Coulomb excitation [8]. This project utilizes a 0.5 μg/cm^2 ^{155}Gd target, shown in Fig. 4.3. It was provided by the Centre of Accelerator Target Science at Argonne National Laboratory, USA.

Figure 4.3: A picture of the ^{155}Gd target.

The target will be positioned inside the target chamber on a target ladder, as shown in Fig. 4.4. The red arrow indicates the direction of the particles. The image displays an Au foil target located inside the chamber. When viewing inside the target chamber, the top is lifted, which allows for atmospheric pressure. To maintain a pressure of 200 Torr in both LIon and Enge, a plug is used to keep the Enge under vacuum.

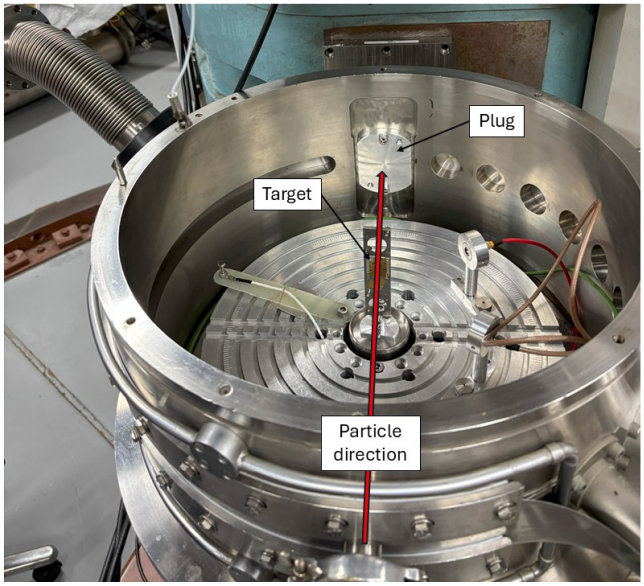

Figure 4.4: The target chamber at beamline 5 with a plug to keep the Enge and LIon at vacuum.

4.3 Enge

The Enge spectrometer is a 1.6 T magnet, that sits on a rotating platform that enables the study of charged particles with a high accuracy. When a charged particle enters the spectrometer, it will be separated and focused on the focal plane of a detector based on magnetic rigidity. By measuring the particle's position on the focal plane, can the energy of the ejected particle be determined. While the resolution of the excitation spectrum will depend on the projectile energy and reaction in question. The Enge spectrometer operates in a vacuum environment to minimize beam deviation. Figure 4.5 illustrates the operating principle of the spectrometer [47].

Further on, the split-pole design creates a magnetic field that provides second-order transverse and vertical focusing. This ensures that charged particles with a different angle but with the same magnetic rigidity will be focused at the same point on the focal plane. Also, Figure 4.5 illustrates a track on which the spectrometer is positioned. The Enge spectrometer can be rotated around the target from -60 to 60 degrees, enabling restriction of the scattering angle and thus the amount of excited states in the residual nucleus. Figure 4.6 shows the Enge spectrometer at the HIAF facility [47].

This thesis involves the Enge spectrometer, to focus protons on the focal plane based on energy. Moreover, the Enge can rotate enabling lower scattering angles to enhance the level of interest, which is crucial in validating low-energy Coulomb excitation.

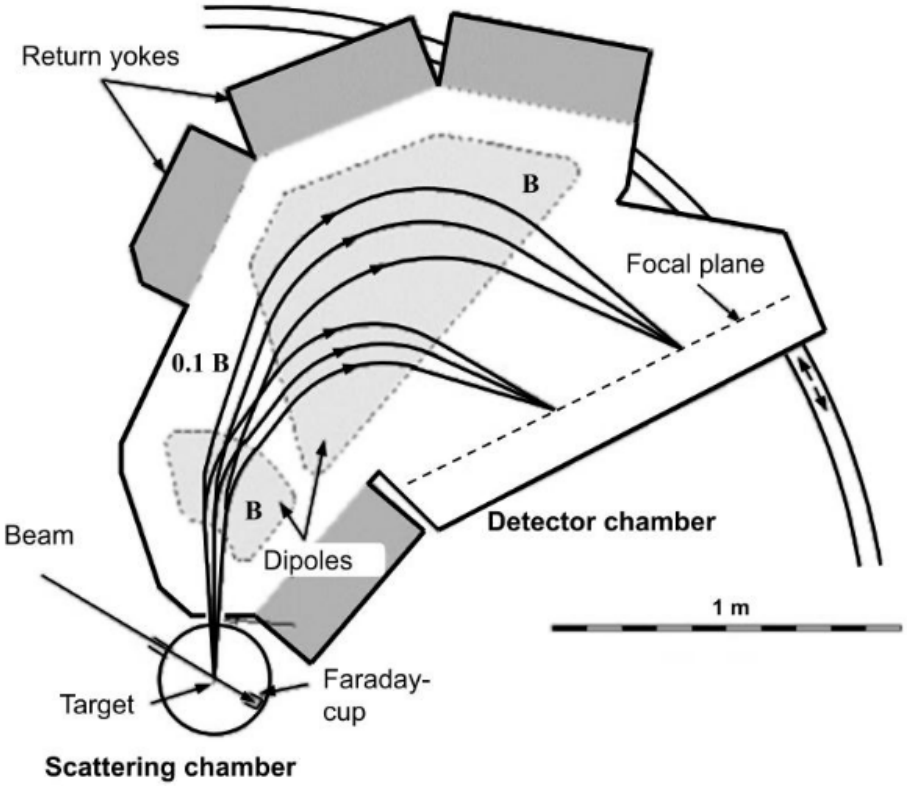

Figure 4.5: Figure to explain the mechanism of the Enge spectrometer, which aligns particles onto the focal plane detector [47].

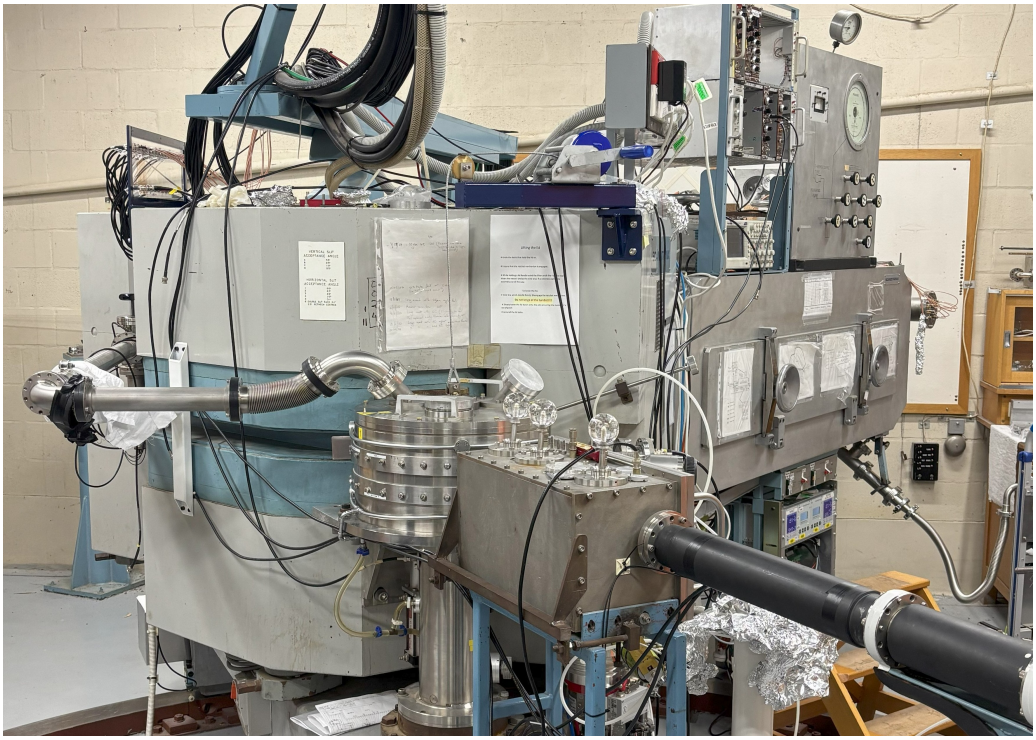

Figure 4.6: The Enge spectrometer at the HIAF facility. It is positioned on rails to rotate the spectrometer.

4.4 Signal processing

The output signals from the scintillators/SiMT combination and the detector preamplifier outputs were input into the XIA Pixie-16 Digitizer, often referred to as Pixie. It is capable of measuring both the amplitude and shape of pulses in nuclear spectroscopy applications, and additionally time of flight measurements. It is a 16-channel all-digital waveform acquisition and spectrometer card. It combines spectroscopy with waveform digitizing and the option of on-line pulse shape analysis. Pixie was originally developed for use with arrays of multi-segmented HPGe γ-ray detectors, however, it accepts signals from virtually any radiation detector. Figure 4.7 illustrates the Pixie-16 system [48].

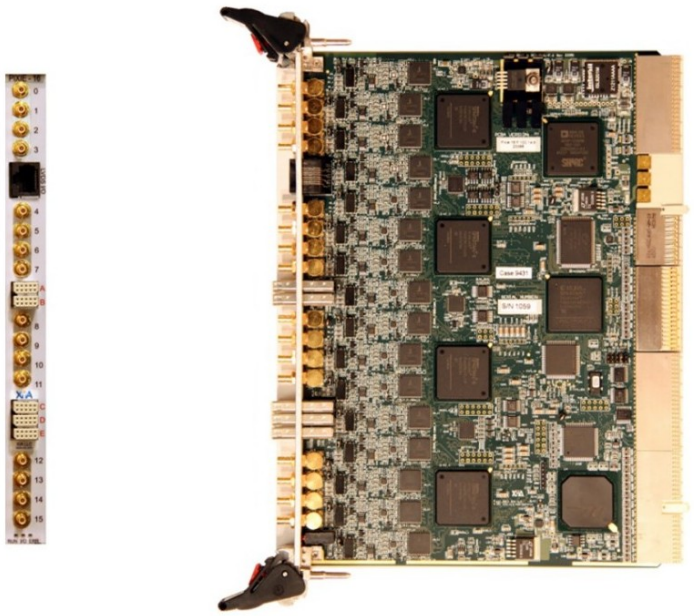

Figure 4.7: A front view on the left and a side view on the right of the Pixie-16 digitizer.

Pixie processes the pulses to determine the energy and time of detection events. This enables to save only the key properties of the event, rather than having to store the entire pulse. By only saving the relevant information, the Pixie system saves memory space. Incoming signals are digitized by 12-bit, 14-bit or 16-bit, 100 mega samples per second (MSPS), 250 MSPS, or 500 MSPS ADCs. The raw data is processed into 'events', containing the key properties of the signal and its origin [49].

The designated program to visualize events is ROOT. An initial sorting was performed, using a code 'pixie2root' developed by the tech group at HIAF, to sort the events into a ROOT tree [49]. ROOT is used to analyze and visualize the data.

4.5 Coulomb excitations conditions

4.5.1 Safe Coulomb excitation energies

The aim is to achieve 'safe' Coulex, where the projectile energy is carefully selected to ensure electromagnetic interactions dominate. This approach maximizes scattering via the Coulomb force while avoiding nuclear reactions. This 'safe' energy is dependent on; the angle of interaction, and the A and Z from both the target and projectile, i.e., the collision partners. The calculation of the 'safe' energy is done in two steps. The first step is calculating the minimum distance between the two particles with [30]:

$$D_{min} = 1.25(A_{projectile}^{\frac{1}{3}} + A_{target}^{\frac{1}{3}}) + D_{interaction}, \tag{4.1}$$

where $D_{interaction}$ is the distance between the collision partners. Afterwards, the second step is calculating the 'safe' energy of the projectile, by [30]:

$$E_{projectile} = \frac{1.44}{2} \frac{A_{target} + A_{projectile}}{A_{target}} \frac{Z_{target} Z_{projectile}}{D_{min}} [1 + (\frac{1}{\sin \frac{\theta}{2}})]. \tag{4.2}$$

If the distance between the collision partners is sufficiently large, the influence of the short-range nuclear interaction is negligible. It is standard practice to apply 5 fm as $D_{interaction}$, since at this distance the strong force accounts for less than 0.5% [4]. The representation of this Eq. 4.1 & 4.2 with angles ranging from 0 until 180 degrees, creates the plot shown in Fig. 4.8.

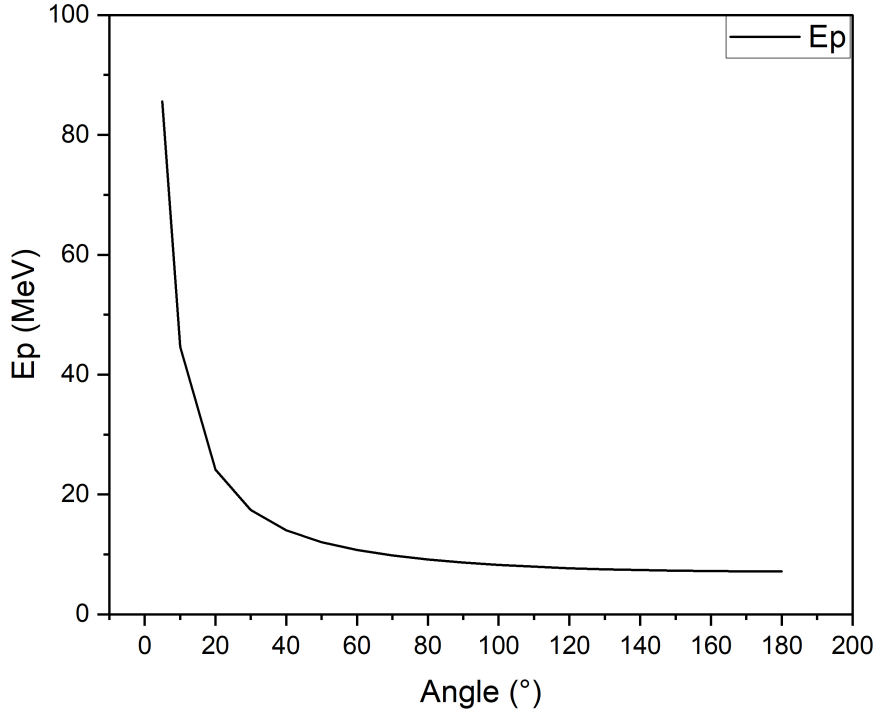

Figure 4.8: The calculation of Eq. 4.1 & 4.2 to visualize the safe energy per angle.

A ‘safe’ energy threshold of less than 14 MeV has been established. The selection of a ‘safe’ energy level is influenced by the collision partners, beam energy, and scattering angle. This project aims to reduce multi-step excitation by choosing collision partners with lower atomic mass numbers (A) and atomic numbers (Z), and by optimizing the scattering angle and energy. Using protons results in significantly lower A and Z compared to previous studies involving ^{16}O [6]. A ‘safe’ energy threshold of less than 14 MeV has been established for scattering angles up to 40 degrees.

4.5.2 GOSIA

GOSIA is a powerful semi-classical fitting code suite for Coulomb excitation experiments developed at the Nuclear Structure Research Laboratory of the University of Rochester in 1980, capable of both designing experiments and analyzing experimental yields through theoretical modeling. The software is based on the Winter-de-Boer code which calculates expected yields from matrix elements using a semi-classical theory of Coulomb excitation. It enables the fitting of matrix elements, such as E1, E2, E3, M1, and M2 transitions, by laying a connection between experimental yields and a theoretical model.

The input of GOSIA is extensive and more than a thousand matrix elements can contribute significantly to Coulomb excitation when using heavy beams to excite strongly-deformed nuclei. GOSIA is widely used in nuclear physics research to study the collective properties of atomic nuclei [8].

This study utilizes GOSIA to simulate and analyze the experiment. A simulation is conducted to calculate the excitation probabilities of each angle and energy. To conduct such simulations, GOSIA requires details about the experimental setup and nuclear data. Eventually, a graph illustrating the relative cross sections is generated based on the excitation probability sums obtained from GOSIA.

Next, GOSIA is employed to analyze the experimental data by recreating the ratio of peaks in the first excited level to the ground level. The matrix elements in the GOSIA calculations are adjusted to reflect the experimental ratio accurately. Because the matrix elements have been fitted to match the experimental data, a value of τ can be calculated using these adjusted matrix elements. This evaluation of τ allows for a meaningful discussion of the experimental results.

Experimental setup

GOSIA simulates experimental designs and requires detailed setup information to accurately fit the matrix elements from experimental yields. This information includes beam attributes, target details, and detector geometry [8].

To integrate the calculated yields over the solid angle of the scattered particles per particle detector, GOSIA demands the geometry of the Light-Ion detector. The input requires spherical coordinates with a list of θ coordinates of the detector placement. The thickness of the target is 0.5 μg/cm^2. The beam particle and target properties required by GOSIA are A and Z [8]. This experiment uses a proton beam onto a ^{155}Gd target, with the necessary properties of both shown in Table 4.2.

Particle	Atomic mass (A)	Atomic number (Z)
Proton	1	1
^{155}Gd target	155	64

Table 4.2: The properties of the beam particle and target.

A requirement for GOSIA is a set of energies around the incident beam energy that spans the range of possible interactions, this must be input to specify the points at which to perform the calculation. These properties will be discussed later on, since they require more in-depth review.

Nuclear data

Nuclear data is vital in enabling GOSIA to fit the matrix elements accurately. GOSIA requires specific nuclear data related to the beam hitting the target, including energy levels, matrix elements, mixing ratios, and branching ratios. This essential nuclear data can be found in the NNDC database [29].

An energy level scheme is needed to assist GOSIA in assessing the correct excited states. The energy levels, along with their associated parity and spin, are obtained from the NNDC [29]. [6] involved approximately 40 energy levels; however, since this is a case of low-energy Coulomb excitation, it is advisable to use a lower limit for the energy levels. Additionally, excited states with a spin greater than or equal to $\frac{13}{2}$ are excluded, as such excitations are unlikely to occur from the $\frac{3}{2}^-$ ground state.

Matrix elements contain information about nuclear structure related to the probability that a particular excited state will transition to another state, and they can be either electric or magnetic. When using GOSIA, it is essential to specify the type of transition involved in the excitation, such as E1, E2, E3, M1, or M2. For each possible transition, a corresponding matrix element will exist [8].

When entering matrix elements into GOSIA, defining a specific number and range for these elements is necessary. While GOSIA can improve the matrix elements, it is limited by the specified range given by the user; a larger range may increase statistical uncertainty. The range is chosen to be approximately an order of magnitude larger than the first transition.

Transitions with multiple matrix elements, for example both a B(E2) and B(M1), own a mixing ratio. These mixing ratios (δ) can be found from Evaluated Nuclear Structure Data File (ENSDF) data files. It is defined as:

$$\delta = \frac{\text{Amplitude of E2 transition}}{\text{Amplitude of M1 transition}}. \tag{4.3}$$

After declaring the mixing ratio of the transition, electromagnetic transitions also exhibit an internal conversion coefficient (ICC). This value, denoted by α, quantifies the probability that a de-excitation emits an internal electron instead of a γ-ray. It is defined as:

$$\alpha = \frac{\text{Number of internal conversion electrons}}{\text{Number of } \gamma\text{-rays emitted}} \tag{4.4}$$

When a particular level can decay to multiple lower energy states, there is a given probability of transition to each of the possible states. Such probabilities are referred to as branching ratios. Like the mixing ratio, branching ratios can be found in the ENSDF file [29]. Branching ratios and internal conversion coefficients are included in the BrIcc database.

Running GOSIA

Each iteration of GOSIA generates input and output files. The initial run to simulate the experiment utilizes matrix elements provided by the NNDC [29]. For higher energy states without specified values from the NNDC, these values are estimated using Weisskopf theory. Original matrix elements are seen as an initial guess by the user, as GOSIA will change them accordingly to match the experimental spectra within the given limits.

GOSIA approaches the fitting of experimental data with a χ^2 function arising from various subsets of data. This fitting routine iterates varying matrix elements within the allowed ranges defined by the user. A χ^2 parameter is calculated from the difference between the calculated yields, branching ratios, mixing ratios and lifetimes given in the input. The fitting procedure stops once a value is locally minimised.

GOSIA calculates the excitation cross section of the excited states given the input using the initial matrix elements. It calculates more than just excitation cross sections, also expected γ-ray yields. However, the excitation cross section is the most relevant to this case. In cases of gamma spectroscopy would this be very applicable.

4.5.3 Beam energy and scattering angle

The choice of beam energy and scattering angle is critical in Coulomb excitation experiments, as these parameters determine which nuclear states are excited and the overall success of the measurement. Figure 4.8 illustrates the boundaries required to achieve safe Coulomb excitation. Higher beam energies allow access to more highly excited nuclear states. However, this increases the number of populated states, complicating the data analysis and potentially reducing the precision of extracted matrix elements. In contrast, too low a beam energy suppresses Coulomb excitation, resulting primarily in Rutherford scattering and low cross sections. The scattering angle is also crucial: smaller angles restrict the number of excited states, whereas larger angles increase the excitation probability for higher-lying levels [4]. This thesis aims to constrain the number of excited energy levels by carefully selecting the beam energy and scattering angles.

GOSIA calculates the effects of both beam energy and scattering angle and determines the excitation probability of each to ensure optimal experimental conditions [8]. The input in GOSIA, such as the beam energy and angle, must be carefully chosen. For example, the particles need to reach the scintillator at low energies. To determine this minimal energy, a GEANT4 simulation was conducted, indicating that a proton threshold of approximately 2 MeV is effective.

Matrix elements were calculated for each transition between the first 15 energy levels. At first, a limit of 10 levels was used. However, the upper few levels of those 10 were yielding excitations similar to the first excited state, indicating that the limit was unjustified. A

new limit of 15 energy levels was used, and results were obtained. Since energy levels are coupled by rotational band coupling, a sensitivity arises from different energy levels. The goal is to use different angles and energies to single out each excited level. GOSIA allows simulation of matrix elements and calculates excitation probabilities for each state. By doing this, a foundation of low-energy levels is established with known matrix elements. Changing the sign of the matrix element in GOSIA clarifies the sensitivity of each level.

The excitation probability associated with the 60 keV energy level was found to have several nearby levels with similar probabilities. As a result, a data sheet was created to compile various energies measured at different angles. Table 4.3 summarizes two examples and displays the excitation probability of exciting that level normalized to one, each corresponding to various energies and angles.

	20 degree & 5 MeV	25 degree & 10 MeV
ground state	9.99×10^{-1}	9.99×10^{-1}
60.0106 keV	5.70×10^{-6}	9.42×10^{-5}
86.5464 keV	4.15×10^{-7}	3.89×10^{-5}
105.3106 keV	4.23×10^{-7}	3.89×10^{-5}
107.5804 keV	1.01×10^{-19}	2.55×10^{-16}
117.9981 keV	4.95×10^{-11}	4.09×10^{-9}
121.10 keV	8.26×10^{-36}	6.80×10^{-32}
146.0696 keV	3.57×10^{-6}	5.42×10^{-5}
230.1286 keV	1.05×10^{-17}	1.65×10^{-14}
251.7056 keV	4.95×10^{-7}	3.88×10^{-5}
266.6474 keV	2.04×10^{-11}	3.45×10^{-9}
268.6238 keV	8.97×10^{-6}	4.97×10^{-5}
287.0041 keV	3.95×10^{-7}	3.29×10^{-5}
321.3793 keV	5.21×10^{-7}	3.91×10^{-5}
326.0881 keV	2.58×10^{-11}	6.48×10^{-9}

Table 4.3: A excitation probability of exciting each certain level calculated using GOSIA. [8]

Different beam energies and scattering angles result in significant variations in excitation probabilities, also referred to as relative cross sections. For example, the ratio between the ground and the first excited states demonstrate a substantial difference in excitation probability magnitude. Furthermore, as shown in the left column of Table 4.3, there are fewer probabilities of the same magnitude. Figure 4.9 shows the relative cross section calculated by GOSIA.

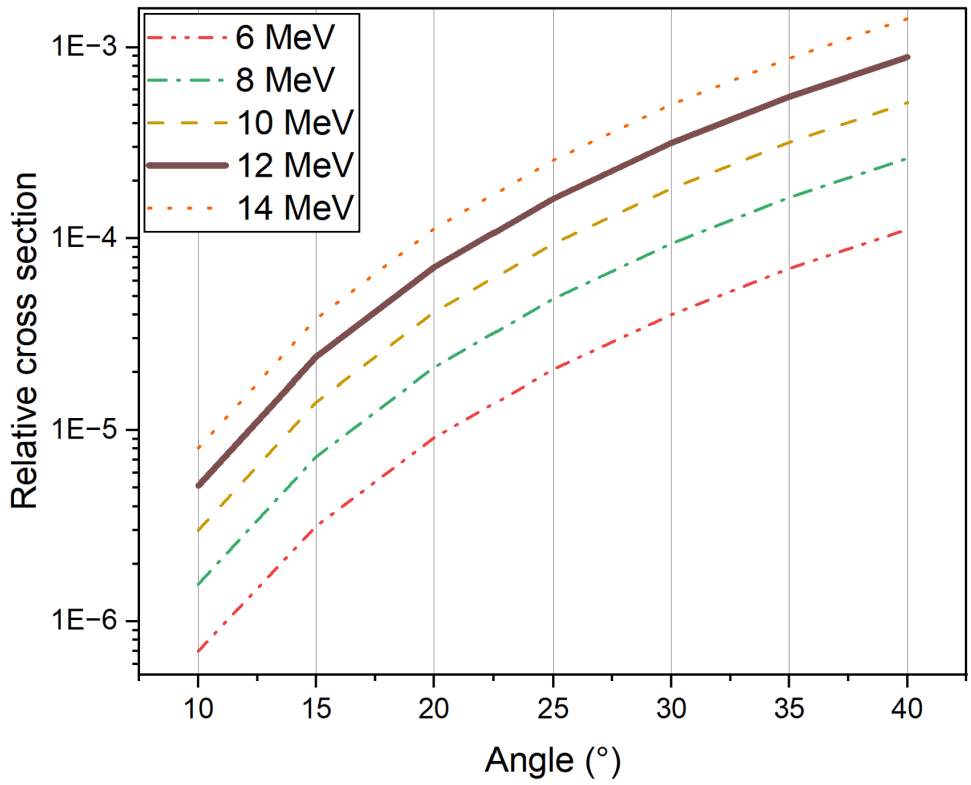

Figure 4.9: Relative cross sections calculated by GOSIA.

Increasing the beam energy excites more energy levels, and a larger scattering angle has a similar effect. Higher energies and greater angles lead to a higher excitation probability [8]. However, as both parameters increase, the excitation probabilities for closely spaced energy levels become similar, making it more challenging to distinguish between them.

1000 counts of the 60 keV level is taken as a threshold to achieve a statistical uncertainty of 3 %. 100 counts would attribute to a statistical uncertainty of 10 %. A constraint on excitation probability arises to ensure an efficient and not overly time-consuming experiment. cross sections on the order of 10^{-3} to 10^{-5}, is required. Hence, energies under 5 MeV are excluded, since they exhibit probabilities of 10^{-6} to 10^{-8}. Ultimately, three beam energies and three angles were selected based on the highest yield for the first excited state and low sensitivity to coupling with higher-lying states. One measurement intersects these selected components' varying energy and angle, resulting in five measurements. Table 4.4 summarizes the chosen energies and angles.

Angle (degrees)	Energy (MeV)
25	5
25	11
25	12
15	12
20	12

Table 4.4: chosen energy levels and angles.

A count rate of 11,000 counts per second (cps) or higher significantly saturates the detector. Moreover, a combination of higher beam energy and a lower scattering angle results in even greater saturation of the detector, as the lower scattering angle and increased beam energy

both contribute to a higher number of counts in the detector. Modifying the horizontal slit size in the Enge apparatus limits the count rate entering LIon, while the vertical slit size affects the resolution. However, this adjustment results in longer measurement durations. For instance, at a scattering angle of 15 degrees and an energy of 12 MeV, the count rate is around 39,000 cps, which would require approximately 1 hour for measurement. By limiting the count rate through slit size adjustments, the measurement duration will increase to around 3 hours, making it three times longer.

The total duration of the experiment is estimated to be 9 hours, excluding the time required to change the angle or the beam energy. During this period, a count criterion of 1,000 counts is expected to be reached for the low-energy Gd^{155} 60 keV state. Changing the beam energy is anticipated to take 20 minutes, while adjusting the angle will require 10 minutes.

Chapter 5

Results & discussion

Chapter 5 provides a thorough interpretation, discussion, and evaluation of the results obtained from the beam run conducted between May 15 and May 22, 2025. Firstly, all the spectra from this run are presented and described. Additionally, the spectra offer another opportunity to test and benchmark the GEANT4 simulation. Since each functional component of the detector is fundamentally different, two distinctions are made: the position wire and the scintillator are discussed separately. Finally, suggestions for improving excitation probability and energy resolution are provided and discussed.

5.1 Data collection

The nuclear particle spectroscopy group scheduled a beam time run from 15-22 May 2025 to investigate three projects: the ^{56}Fe(d,p) reaction, Coulomb excitation of protons on ^{155}Gd, and a small experiment for an undergraduate student to benchmark the GEANT4 simulation even further. The run encountered several technical challenges, but was ultimately successful. Initial beam tuning issues with ^{16}O delayed data collection until Friday, May 16. That same day, in an attempt to speed up the run, a deuteron beam was suggested for Coulomb excitation. Although the deuteron beam presented fewer operational challenges, its low resolution did not improve experimental outcomes. A cathode replacement, necessary for investigating the ^{56}Fe(d,p) reaction, was scheduled for Friday afternoon. The cathode replacement enabled the first measurements. However, analysis revealed unexpected spectral features from the iron target, later attributed to insufficient iron on the target. The issue was alleviated by switching to an older iron target; however, this target has a hole in the middle, complicating data analysis. To produce protons, the old cathode was reinstalled on Tuesday, May 20, at noon.

Coulomb-excitation data collection occurred at HIAF from 8 p.m. on Tuesday, May 20, to 1 p.m. on Wednesday, May 21. The run was intended to continue until 7 a.m. on May 22; however, an issue arose. During the final angle measurement, a position wire sparked, leading to the termination of the entire run. The spark was likely caused by a minor drop in gas density, which resulted in the position wires, charged with 2000 volts, sparking. As a result of the premature ending, only three datasets were successfully obtained. Therefore, no measurements were taken with varying beam energies.

To ensure accurate data collection, certain detector components were turned off. Position wire one was disabled due to coupling with the other position wire, allowing reliable data from the remaining wire. Both anodes were also switched off because of coupling with the Frisch grid and position wires. The cathode was partially deactivated and did not produce a detectable signal.

The high count rate induced by the low scattering angles was more difficult than initially expected. A count rate that high could damage the detector, hence many steps were taken to lower the count rate. A 1 mm x 3 mm aperture was inserted to lower the flux. Furthermore, the Enge slit size was adjusted to a smaller size. The beam current at the last Faraday cup measured 1.5 attoampere (enA). To calculate the particle flux, a conversion of enA to Cs^{-1} must occur:

$$1\text{enA} = 1 \times 10^{-9}\ Cs^{-1}. \tag{5.1}$$

Now it can be converted to the number of particles in the beam per second by:

$$\begin{aligned} N_{particles} &= \frac{\text{enA} \times 10^{-9}}{q \times C}, \\ N_{particles} &= 9.375 \times 10^{9}. \end{aligned} \tag{5.2}$$

Here, q denotes the charge state of the beam, which is one for protons. Thus, 9.375×10^9 particles per second were delivered during the experiment. The slit size of the Enge spectrograph further limits the particles per second to a moderate amount. The dataset

includes three distinct angles, with position wire 2 and the scintillator, focusing on 12 MeV protons at scattering angles of 20, 25, and 30 degrees. Changing the scattering angle took about 20 minutes.

5.2 Spectra

The LIon device has several functional components, each serving a specific purpose. In this experiment, only wire position two and the scintillator were turned on. The spectra reveal 12 MeV protons scattered at angles of 20°, 25°, and 30°, which lasted for 105, 240, and 420 minutes, respectively. Considering 9.375×10^9 particles per second, 1.62×10^{-4} excitation probability of the first excited state for a 12 MeV proton and 25° scattering angle and the measurement time, the threshold of a 1,000 counts in the first excited state was not achieved. Since these measurements quantify distinctly different mechanisms, they will be discussed separately.

5.2.1 Position wire

The position of a signal in the wire is measured from both ends of the wire. As a result, the difference in time enables a time-of-flight (TOF) measurement. This process effectively indicates the position of the particle on the focal plane. The Enge spectrograph is capable of distinctly focusing both high-energy and low-energy particles onto the focal plane. The particles of interest are in focus, while the scattered products are found off-center. During the beam run, a calibration of the time scale to energy was performed. Since the position wire measures the time difference rather than the energy of the protons, an indirect relationship is established between proton energy and position on the focal plane. The gyroradius (ρ) is proportional to the position on the focal plane and is indirectly dependent on the proton energy. The relationship between the gyroradius in the magnetic field and the proton energy is given by:

$$\rho = \frac{\sqrt{2m_p E_p}}{q_p B}. \tag{5.3}$$

Where m_p, E_p,q_p are the mass, energy and charge of the proton, respectively, and B is the magnetic field in the spectrometer. Given the energy of the first excited state, the energy of the proton is:

$$\begin{aligned} E_p &= E_{beam} + Q_{value} - E_{level}, \\ E_p &= 12 \text{ MeV} + 0 - 60 \text{ keV}, \\ E_p &= 11.94 \text{ MeV}. \end{aligned} \tag{5.4}$$

Since the energy of the proton is now known, the gyroradius can be calculated with:

$$\begin{aligned} \rho &= \frac{\sqrt{2 \times 1.67353 \times 10^{-27} \times 11.94 \times 10^6 \times 1.602 \times 10^{-19}}}{1.602 \times 10^{-19} \times 0.7985} \times 100, \\ \rho &= 62.5501 \text{ cm}. \end{aligned} \tag{5.5}$$

The times a hundred is to transfer m into cm. A calibration of the gyroradius to the proton energy occurred with the isotope ^{54}Fe, since previous work conducted by [50] identified significant peaks at the expected energy levels in this isotope. This gave the quadratic relationship seen in Fig. 5.1.

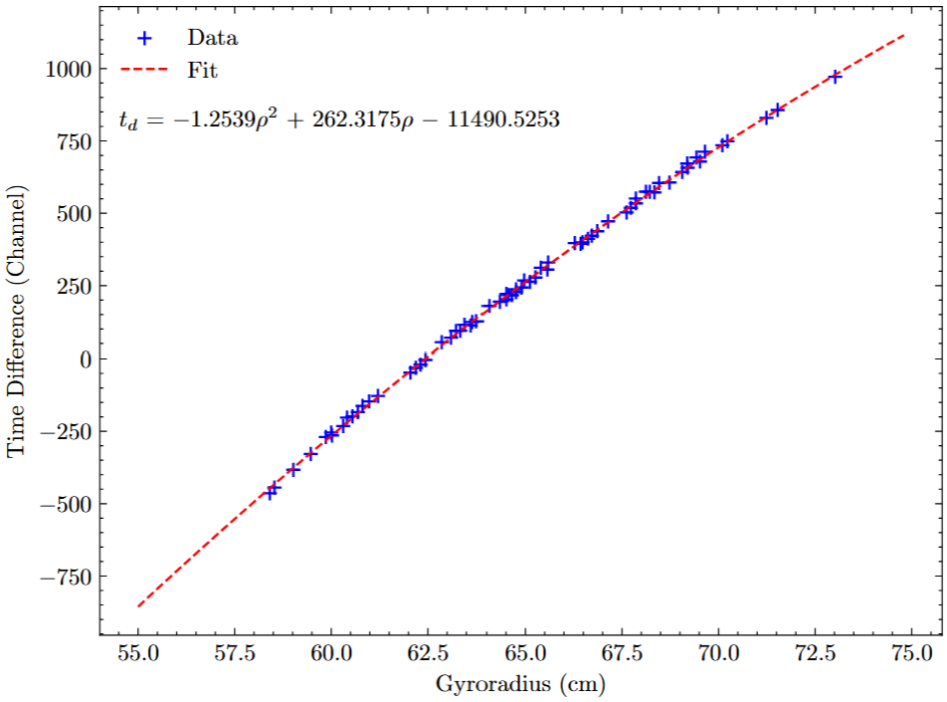

Figure 5.1: The calibration of the time difference with the gyroradius executed by the known peaks of ^{54}Fe [50].

Given the fitting equation shown in Fig. 5.1, which has a R^2 of 0.998. The time difference can now be calculated with:

$$\begin{aligned} t_d &= -1.2539(62.5501)^2 + 262.3175(62.5501) - 11490.5253, \\ t_d &= 11.558 \text{ ns}. \end{aligned} \tag{5.6}$$

Hence, the 60 keV level is 11.558 ns distanced from the center of the elastic scattering peak. The count rate from the Coulomb-excitation experiment was too high for the PIXIE detector to handle, thus a Timing Filter Amplitude (TFA) was employed to interpret the signal. A TFA reduces the tail of the signal, shortening its duration and limiting it to specific boundaries. Figure 5.2 illustrates how a TFA works [51].

In Fig. 5.2 the top line represents the original signal, while the bottom line is the final form of the original signal. The use of such tools causes changes in the signal spectra, which can lead to inaccuracies in calibration. The exact center of the overall spectrum is shifted [51], while the inter-spacing remains precise. Therefore, the elastic scattering Gaussian curve should still be approximately 11.6 nanoseconds away from the 60 keV peak.

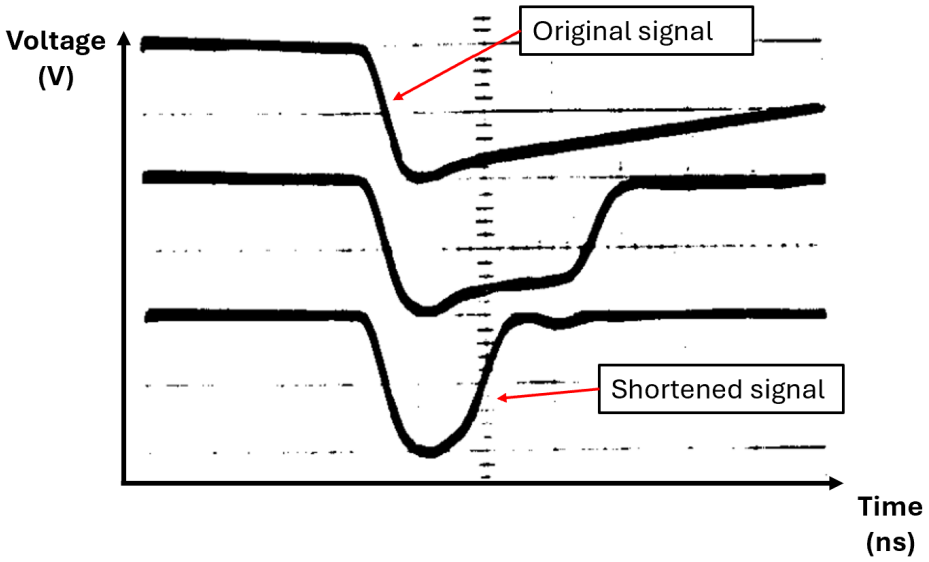

Figure 5.2: The working principle of a TFA explained, in which a signal gets modeled down to a shorter signal [51]. The original signal gets shortened to decrease the dead time.

As previously mentioned, the experiment utilizes only one position wire due to coupling effects between the wires. In this setup, position wire 2 is activated, which is the closest to the entrance window. The Enge spectrograph is focusing 12 MeV protons at the center of the focal plane, which corresponds to 0 ns, while the reaction products are located off-center. The inelastic scattering products lose energy and, as a result, do not get focused by the Enge to the same location as the elastic scattering products. Figures 5.3, 5.4 and 5.5 show the spectra from the second position wire.

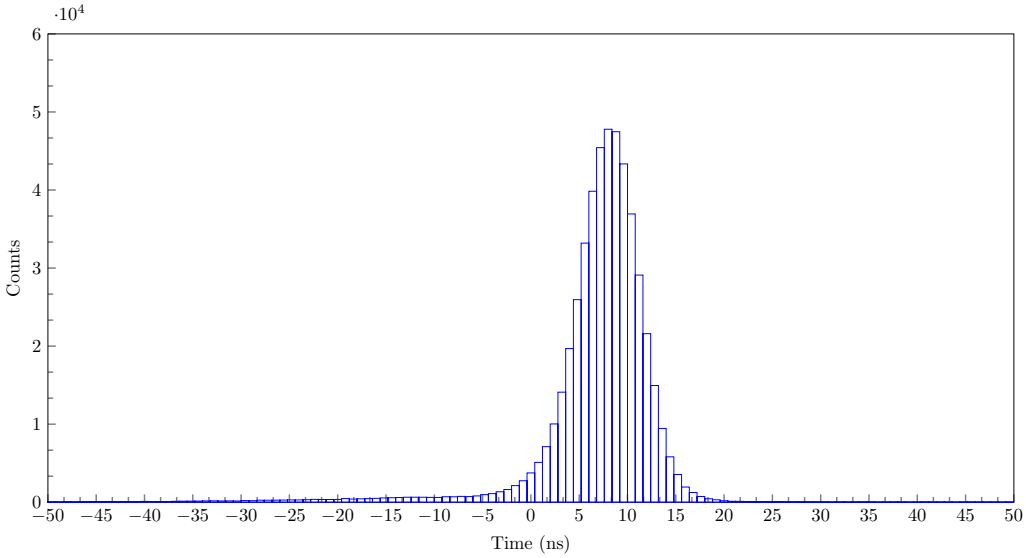

Figure 5.3: The spectrum for 12 MeV protons and a 20° scattering angle.

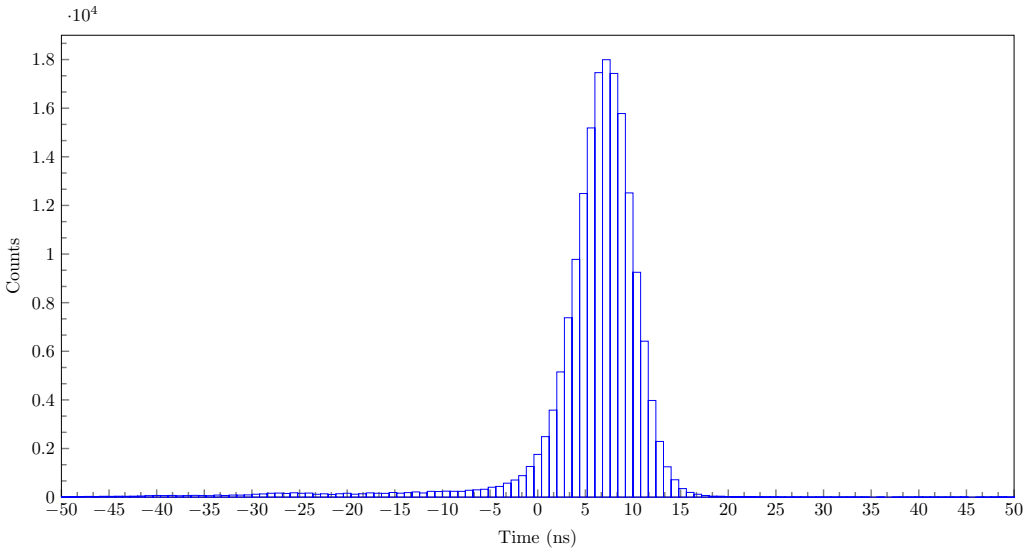

Figure 5.4: The spectrum for 12 MeV protons and a 25° scattering angle.

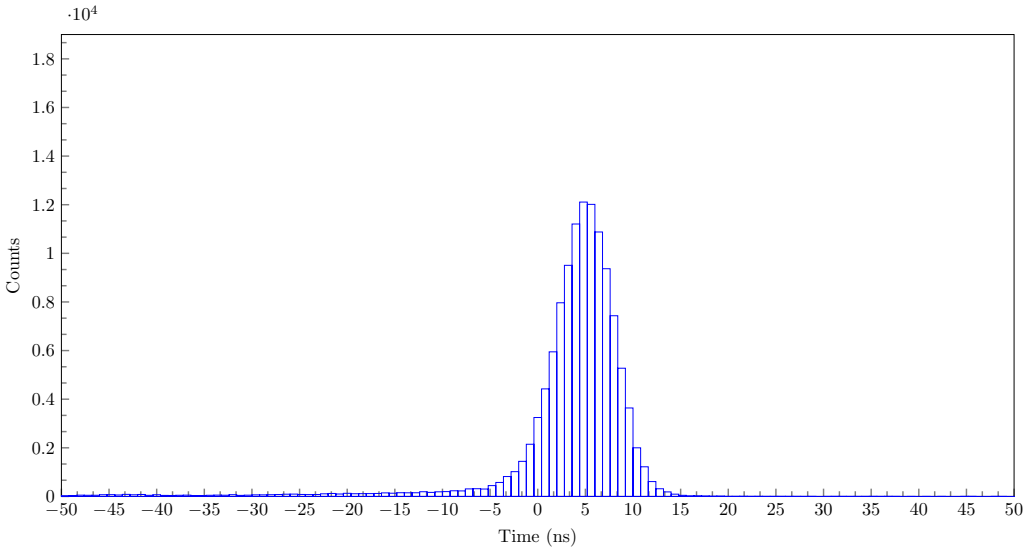

Figure 5.5: The spectrum for 12 MeV protons and a 30° scattering angle.

All figures have a linear y- and x-axis. A total of approximately 780 k, 235 k, and 300 k entries are recorded, respectively. The biggest peak is for each spectrum in the order of $\approx 10^4$.

The largest peak near five ns is associated with the elastic scattering of the ground state. The Full Width Half Maximum or FWHM is 7.36, 6.7, and 6.95 ns, respectively. Additionally, all graphs display a left shoulder, which can be attributed to the tail of elastic scattering, inelastic scattering, and contaminants. Each graph exhibits an overall background of fewer than ten counts. Figures 5.6, 5.7 and 5.8 show a zoomed-in version on the left shoulder.

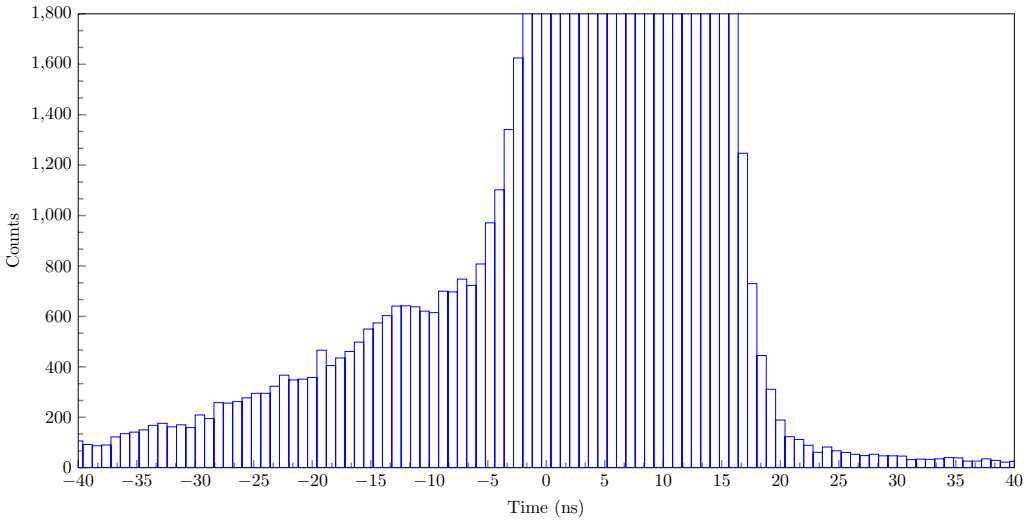

Figure 5.6: A zoomed-in spectrum for 12 MeV protons and a 20° scattering angle.

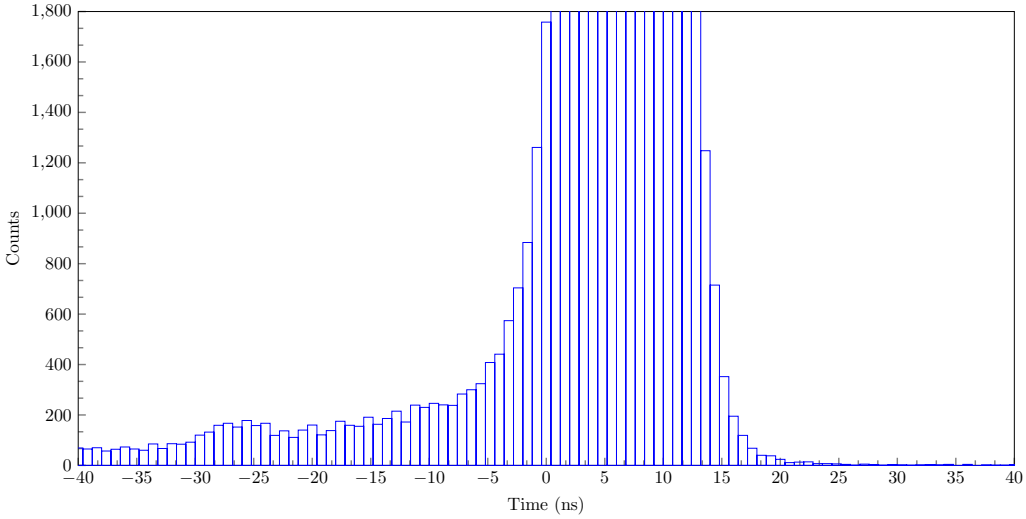

Figure 5.7: A zoomed-in spectrum for 12 MeV protons and a 25° scattering angle.

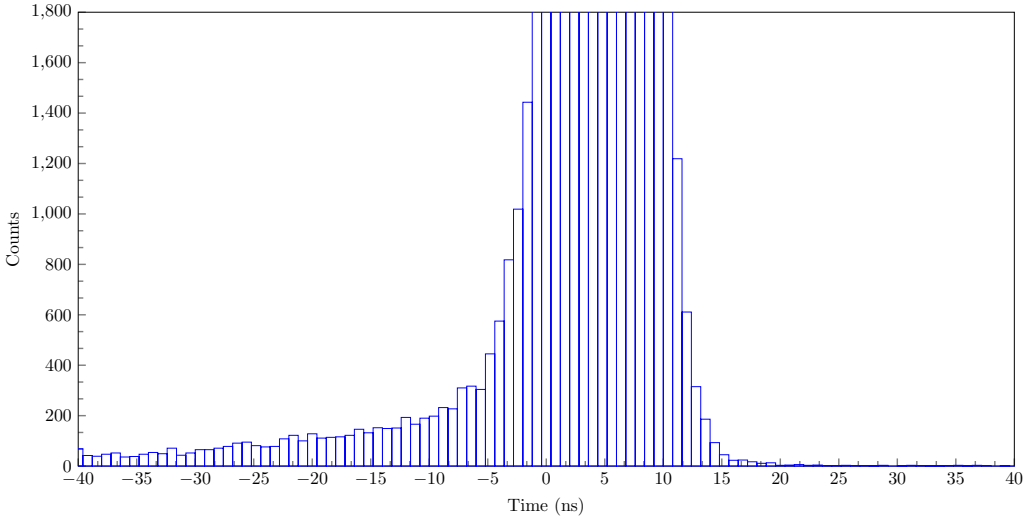

Figure 5.8: A zoomed-in spectrum for 12 MeV protons and a 30° scattering angle.

First of all, all figures display a broader left shoulder compared to their right shoulder. The zoomed-in spectra show a series of insignificant peaks. Each figure contains a small peak at the 60 keV level. The location of the peak varies and the height too. Figure 5.8 illustrates a peak from the 60 keV state at -6 ns.

The significant, albeit still minor, peak observed at -13 ns in Fig. 5.6 correlates with the excitation of closely lying states. In Fig. 5.7, there is a broad peak at -28 ns. Although this could indicate the excitation of a state, it is highly unlikely. The 28 ns timing corresponds to 120 keV, and the excitation of the 121 keV state in Gd is improbable due to its spin of $\frac{11^-}{2}$. This is true for the Fig. 5.8 at -41 ns. The peaks correspond to kinematics of the carbon and oxygen contaminants, since the peaks match the energy loss attributed from oxygen and carbon.

5.2.2 Scintillator

The scintillator output is collected from both ends, and the resulting spectra are summed to improve signal statistics. Compared to the position wire, the scintillator readout is more straightforward, as it does not require time-of-flight measurements or position calibration. Furthermore, a calibration of the scintillator did not occur. Figures 5.9, 5.10, and 5.11 show the spectra of the scintillator.

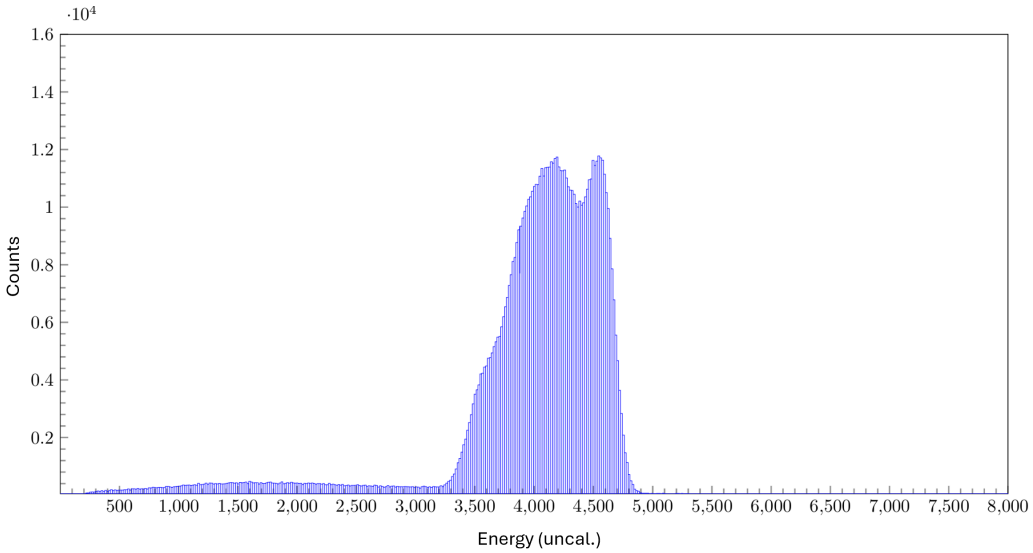

Figure 5.9: The spectrum from the scintillator at 20 degrees with 12 MeV protons.

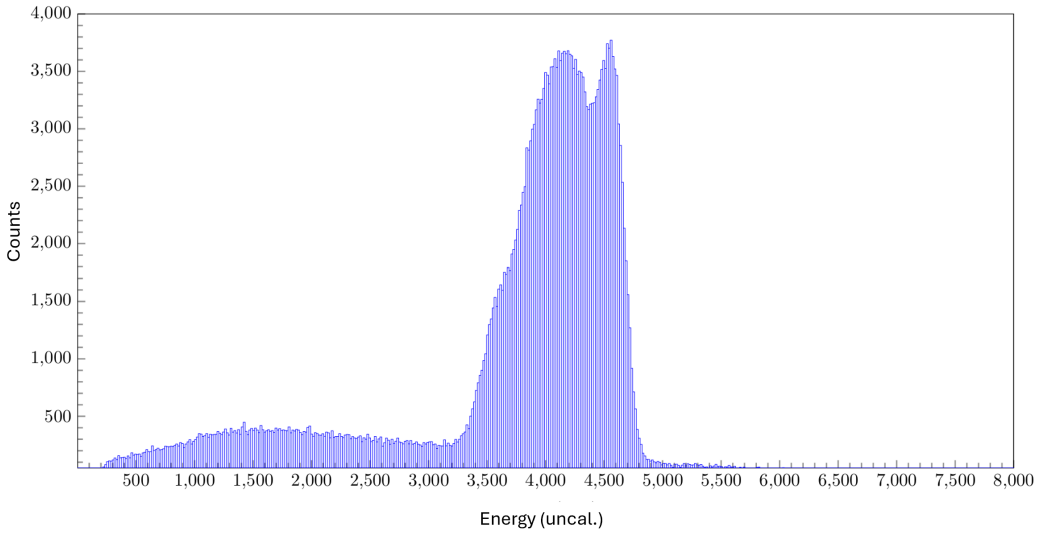

Figure 5.10: The spectrum from the scintillator at 25 degrees with 12 MeV protons.

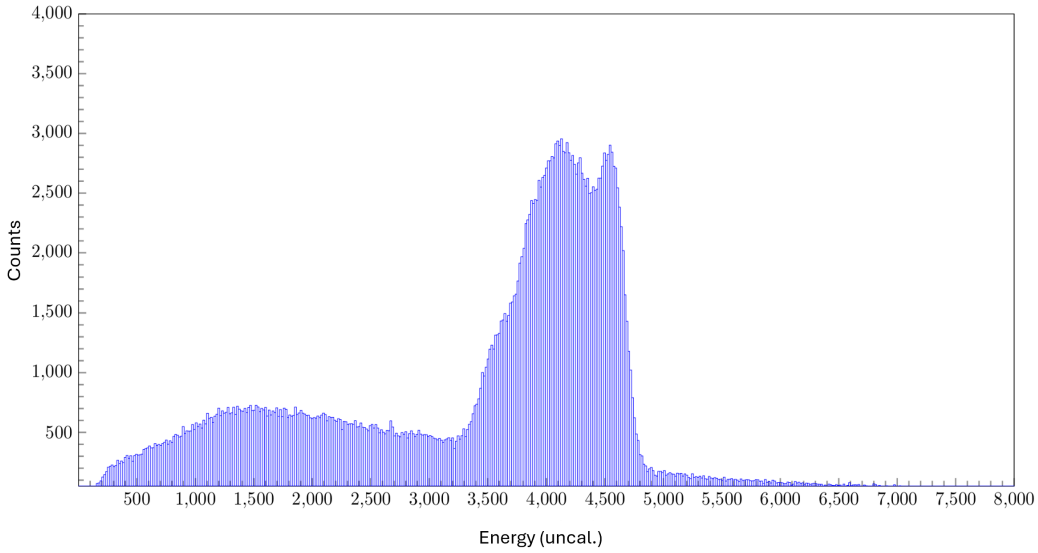

Figure 5.11: The spectrum from the scintillator at 30 degrees with 12 MeV protons.

Figure 5.9, 5.10, and 5.11 show the spectrum from the scintillator with $\approx$ 320 k, $\approx$ 240 k, $\approx$ 800 k entries, respectively. Do note that the x-axis is uncalibrated.

The scintillator is read out at two sides. The Enge will focus the particles of interest at the middle of the position wire, yet, this will create a separation of signal at the scintillator. In the scintillator, a distinction is made between left and right. Due to the focus on the position wire resulting in a de-focus on the scintillator, one signal is shifted relative to the other. Figure 5.12, 5.13 and 5.14 show the spectra separately for each angle.

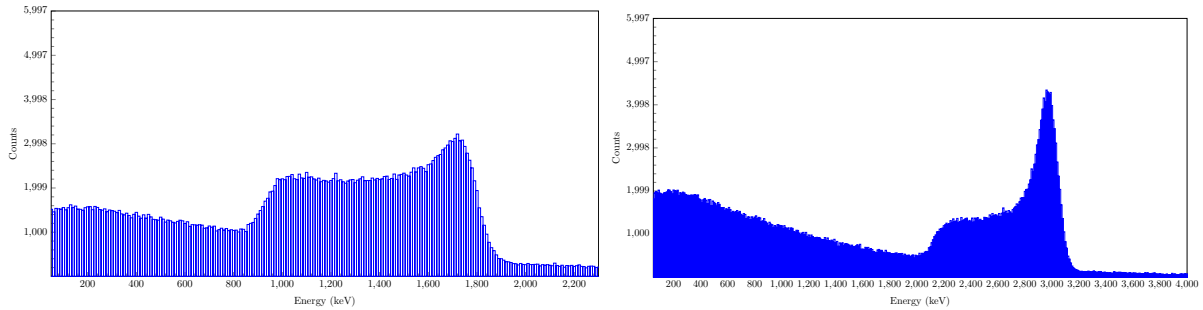

Figure 5.12: The spectra of a 12 MeV 20 degree scattering angle from both sides of the scintillator. On the right side the spectra of the high-energy side, while on the left the low-energy side.

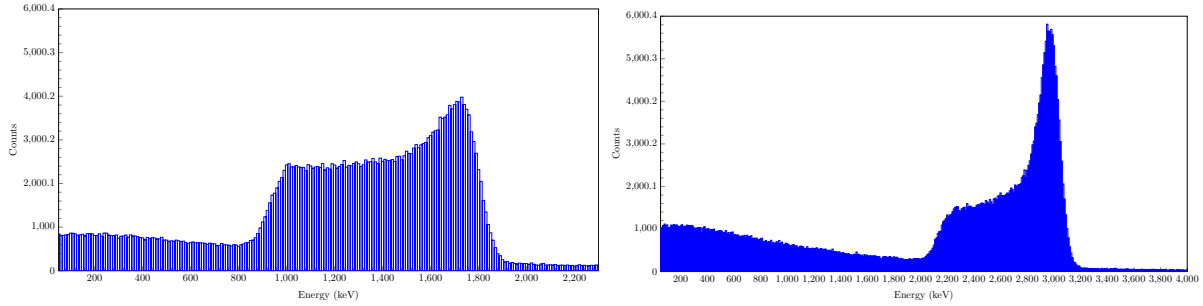

Figure 5.13: The spectra of a 12 MeV 25 degree scattering angle from both sides of the scintillator. On the right side the spectra of the high-energy side, while on the left the low-energy side.

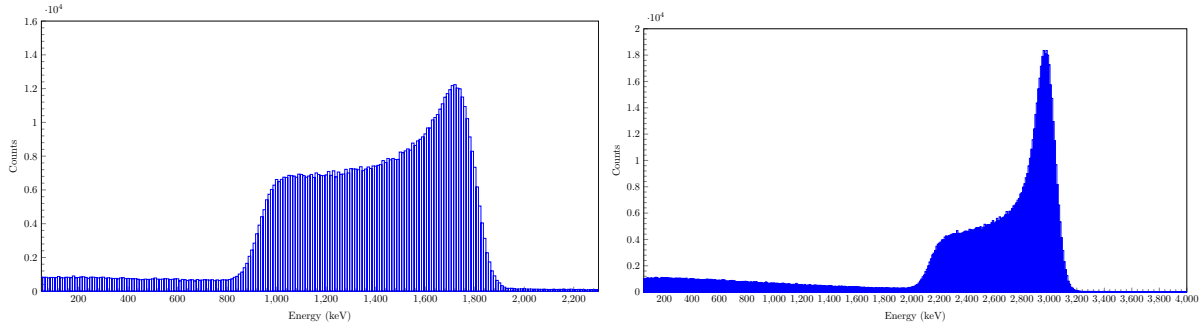

Figure 5.14: The spectra of a 12 MeV 30 degree scattering angle from both sides of the scintillator. On the right side the spectra of the high-energy side, while on the left the low-energy side.

The x-axis of these graphs represents uncalibrated energy. However, it is impossible to calibrate this axis because the total energy remains unknown. Particles may elastically scatter off the target while retaining their energy, but they could lose some energy as they travel further. These losses prevent accurate calibration of the x-axis.

The spectra are shifted along the x-axis due to the focus onto the position wire. To identify each energy side, one can examine the ratio of the peak to the shoulder and compare the total counts within the peak. The right side exhibits a higher ratio and contains a substantially larger number of counts, and consequently is the high-energy side. This high-energy side shows a significant peak, correlating to elastic scattering, around 3000 energy (uncal).

Energy straggling can cause particles to lose energy, leading to a shift of the Bragg peak to the left. This shift creates a broad shoulder on the left side of the peak. However, parts of this band are also excitation losses from the protons or even contaminants. However, the location of the 60 keV peak is unknown because the x-axis is not calibrated; thus, analysis is not feasible.

5.2.3 GEANT4 spectra

The simulation model showed promising results in the benchmark, and hence was used to design the experiment. One of the objectives of generating spectra with GEANT4 is to validate the simulated model even further. To achieve this, spectra with identical parameters are created using GEANT4. Simulations are conducted for 12 MeV protons at scattering angles of 20, 25, and 30 degrees, each comprising 10,000 entries. Figure 5.15 illustrates the GEANT4 model containing all 10,000 entries for a 12 MeV proton beam at 25 degrees.

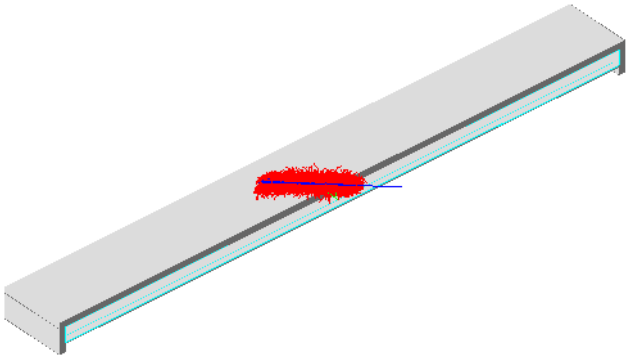

Figure 5.15: A 3D view of the GEANT4 simulated model of LIon with 10,000 entries of a 12 MeV proton beam and 25 degrees.

As stated earlier, GEANT4 does not support avalanche applications. Therefore, the position wire data should be considered unavailable, with only the scintillator data available for discussion.

GEANT4 simulates a proton with a specific energy. However, since the simulation does not account for interactions with the target, an energy distribution is not automatically generated, resulting in a perfect Gaussian distribution each time. To address this issue, a imitation energy distribution was developed. The target is seen as a complex structure with multiple layers, where at each layer the excitation probability calculated by GOSIA is sampled. This approach makes the GEANT4 simulation sensitive to scattering angles, which it was not previously.

The distribution is based on sampling the energy of the projectile 1500 times, with probabilities calculated using GBOSIA for 15 energy levels. Several sampling amounts were tested, including 1, 10, 25, 50, 75, 100, 500, 1000, 1500, 2000, and 5000 times. Ultimately, 1500 samples were chosen, as this amount was the most similar to the experimental spectra.

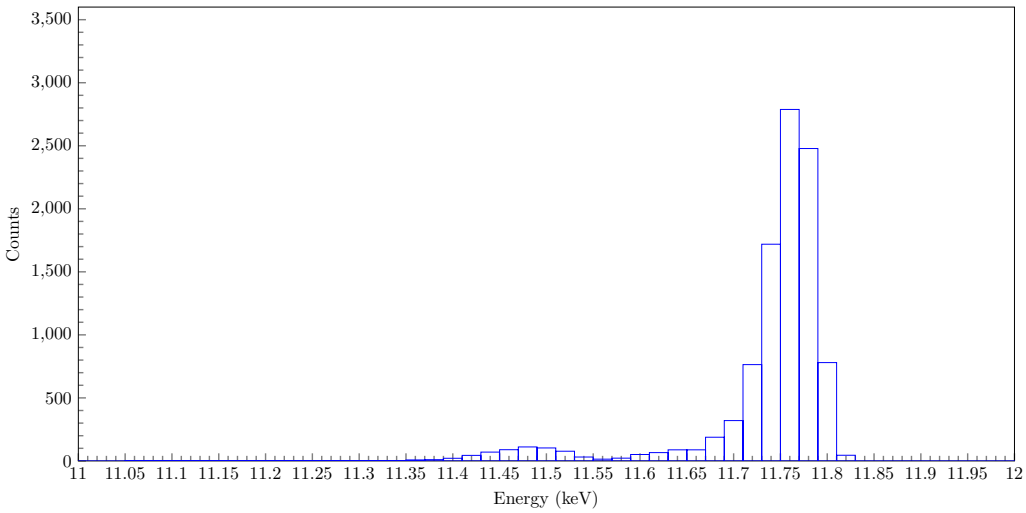

Figure 5.16: The spectrum from the simulated GEANT4 model for a 12 MeV proton beam at a 20-degree scattering angle.

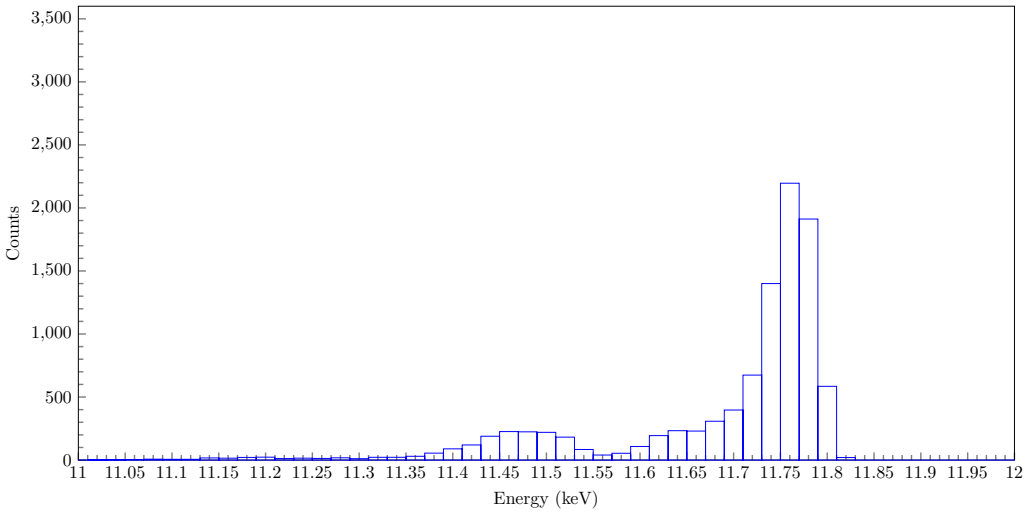

Figure 5.17: The spectrum from the simulated GEANT4 model for a 12 MeV proton beam at a 25-degree scattering angle.

Figures 5.16, 5.17, and 5.18 display the spectra for the 20-degree, 25-degree, and 30-degree simulations, respectively. The spectra are quite similar, each showing at least two distinct peaks. The tallest peak, which corresponds to elastic scattering, appears in every spectrum at approximately 11.7 MeV, indicating that most energy deposition occurs within the scintillator.

A weaker peak is also visible, which aligns with energy loss due to energy straggling, as indicated by the GOSIA probabilities. The sensitivity to scattering angles is evident, as larger scattering angles excite more energy levels. While a broader peak for the excited levels was generally expected, the significantly low probabilities for some levels resulted in the formation of only a narrow peak. Additionally, a final third peak is clearly shown in Fig. 5.18 and can be observed as a hint in Fig. 5.17. Larger scattering angles excite higher energy states, resulting in a more pronounced third peak.

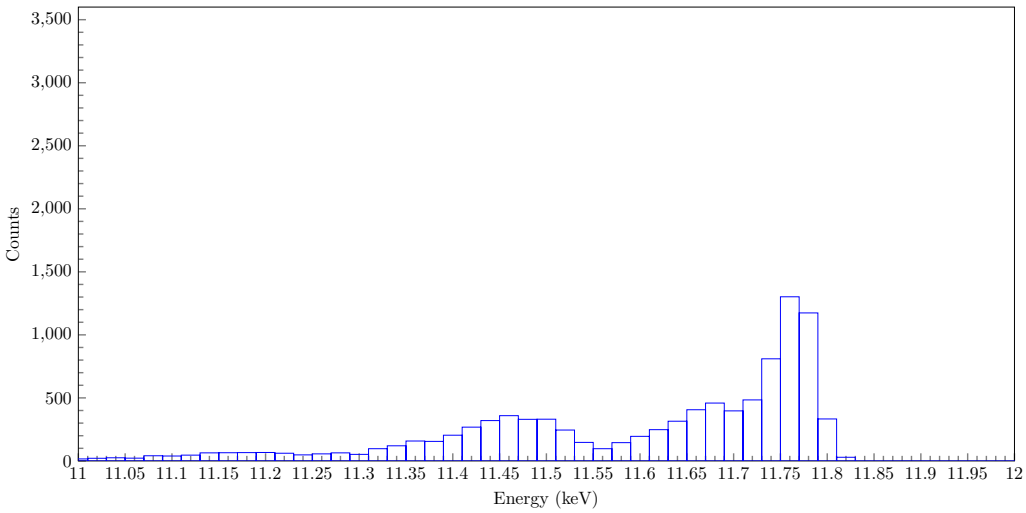

Figure 5.18: The spectrum from the simulated GEANT4 model for a 12 MeV proton beam at a 30-degree scattering angle.

5.3 Yields

To extract vital information from the experiment, it is necessary to determine the number of counts at the 60 keV excitation level. By plotting the GOSIA probabilities, an indication of the peak characteristics is revealed. Since the ground-state peak is clearly visible in experimental spectra, was its height used for normalization. Figure 5.19 displays the resulting probability distribution for the 25-degree measurement.

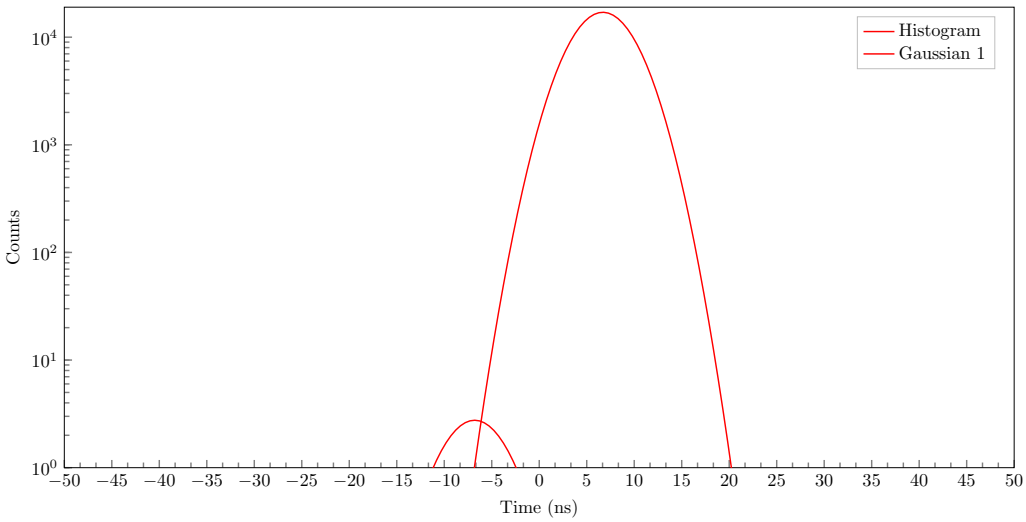

Figure 5.19: A summation of the probabilities from the ground state and the first excited level for the 25 degree scattering angle with an equal amount of counts as the correlating experimental measurement.

GOSIA analysis indicates a very low excitation probability for the 60 keV level, complicating to distinguish the elastic scattering and the first excited inelastic state peaks. This phenomenon is also seen in the experimental spectra. As shown in Fig. 5.7, zooming in reveals only a slight enhancement at 60 keV at 10 ns. This is primarily due to the significant tail from elastic scattering, which arises from energy loss as particles traverse the relatively thick target. The resulting energy spread produces a tail that overlaps the

region of interest, making it difficult to resolve the 60 keV peak. Consequently, attempts to fit this peak using tools such as the gf function from ROOT were unsuccessful.

The enhanced view of the 25 degree scattering angle does not show only one peak. The spectra has significant peaks around 40 and 25 ns. The calibration of the time axis enables a search for the identity of these peaks. A search was conducted to reveal the origin of the peaks. It was initially believed that these peaks originated from contaminants in the target, such as ^{156}Gd. However, this did not appear to be the case. However, the kinematics of carbon and oxygen match the peaks perfectly. Therefore, these peaks correspond to carbon and oxygen.

Combining the simulated and experimental data, as shown in Fig. 5.20, illustrates the effect of the low probability, which complicates efforts to clearly visualize the 60 keV level. Furthermore, with regard to the GOSIA probabilities, the expected number of counts at the 60 keV level is approximately three. This very low count rate explains the difficulty in observing and fitting the peak in the experimental spectra.

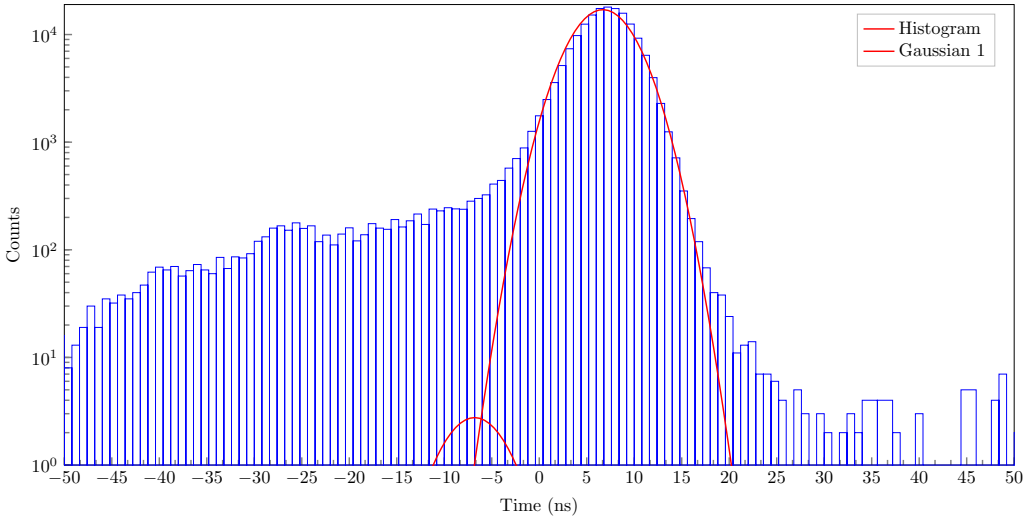

Figure 5.20: The combination of the probabilities of GOSIA (red) and the experimental data (blue) for a 12 MeV proton beam with a 25 degree scattering angle.

In summary, although a small peak corresponding to the first excited level is visible in the experimental spectra, the low statistics and significant background prevent reliable extraction of its counts. Without this information, it is not possible to perform a precise GOSIA analysis of the experiment to extract the matrix elements.

5.4 Discussion

The discussion of results is separated in validating the GEANT4 model and the discussion of the results from the position wire and scintillator data. A validation of the GEANT4 model is done by comparing the experimental data to simulated data. Afterwards, the spectra from the three datasets are further explained and discussed as to why the experiment failed.

5.4.1 Validation of GEANT4 model

The validation of the simulation requires a deep understanding of how both the experimental and simulated systems acquire their results. The objective here is to compare the GEANT4 simulation outcomes with those obtained from the LIon detector system.

In the LIon setup, the plastic scintillator transfers the energy deposited by incoming particles into a light signal, which is subsequently enhanced and read out by the SiPM. In contrast, GEANT4 records the energy deposition directly, without any processing steps. Practical limitations affect the experimental spectra, including decay time, dead time, relative light output, and de-focusing of the particles.

The elastic peak observed in the simulated spectra appears to correspond with the experimental data. However, the height of the peak differs, which is understandable given the significant difference in the number of entries. GEANT4 was unable to process the total entry count of 10^7 from the experimental data in the scintillator. The exact location of the peak cannot be discussed as the experimental spectra are not calibrated.

The characteristics of the shoulder of the inelastic peaks are fundamentally different. The simulated spectra display distinctive peaks, while the experimental spectra show a continuous shape that appears as a shoulder. Several factors could contribute to this discrepancy: contamination in the experimental spectra, insufficient levels implemented in the GOSIA calculations, or inaccuracies in the reproduction of the energy distribution.

Contaminants such as carbon and oxygen are commonly observed in experimental spectra. The distinction between these two spectra can be enhanced as the proton beam passes through the Enge spectrograph following target scattering. However, this specific step is not represented in the GEANT4 simulation. Since the kinematics of carbon and oxygen are known, they could be implemented similarly to the energy distribution created using GOSIA's excitation probabilities.

A continuous spectrum from the simulated data could be missing if not enough energy levels and their respective probabilities are used. Additionally, using more energy levels might alter the GOSIA probabilities for lower-lying states. A definitive answer on the number of levels is difficult to provide. The highest implemented energy level should have a negligible excitation probability, which is achieved in the implemented energy levels.

Finally, the imitation of energy distribution is completely inaccurate because cross sections depend on energy. The cross section varies with energy, meaning that lower-energy particles interact differently than higher-energy particles. In the GEANT4 simulation, this distinction is not taken into account in the energy distribution, leading to a bias in the

results.

5.4.2 Discussion of results

This experiment demonstrated that it was not possible to extract the number of counts from the experimental spectra for two main reasons: the low probability of exciting the 60 keV energy level and the limited position resolution of the position wire. Additionally, the high density of closely lying states complicates the experiment. Improvements in both position resolution and excitation probability are necessary to extract the amount of counts in the level of interest. The methods to resolve these main problems are discussed separately.

Low probability of the 60 keV level

The first issue encountered in the experiment is the low number of counts at the 60 keV level. The probability of exciting the state of interest is notably small, even with the carefully selected beam energy and scattering angle. The high count rate in the detector proved to be a larger problem than initially anticipated, causing the threshold of 1,000 counts in the first excited state to not be achieved.

To address this high count rate, changing the aperture and slit size significantly reduced the number of beam particles. However, this adjustment resulted in a substantial increase in the measurement time. For instance, the original measurement for the 25-degree scattering angle with a 12 MeV proton beam was estimated to take 30 minutes. With the new settings, this duration extends to more than a day.

The probability of exciting the 60 keV level is primarily determined by the atomic mass number and the atomic number of both the projectile and target. While both of these parameters are fixed for the target, using a slightly heavier projectile can lead to a higher probability of exciting the first excited state. Deuterons, which have a slightly greater mass than protons, result in increased excitation probabilities. Figure 5.21 illustrates the relative cross sections associated with exciting the first state using deuterons.

Deuterons at 25 degrees and 12 MeV exhibit an excitation probability of 3.25×10^{-4}, compared to protons, which have an excitation probability of 1.62×10^{-4}. Despite the higher excitation probability of the deuterons for the level of interest, the position resolution was unexpectedly worse. Possibly because of a low lifetime of the signal. A FWHM of 12 ns was achieved. This positional resolution continues to hinder the success of the experiment.

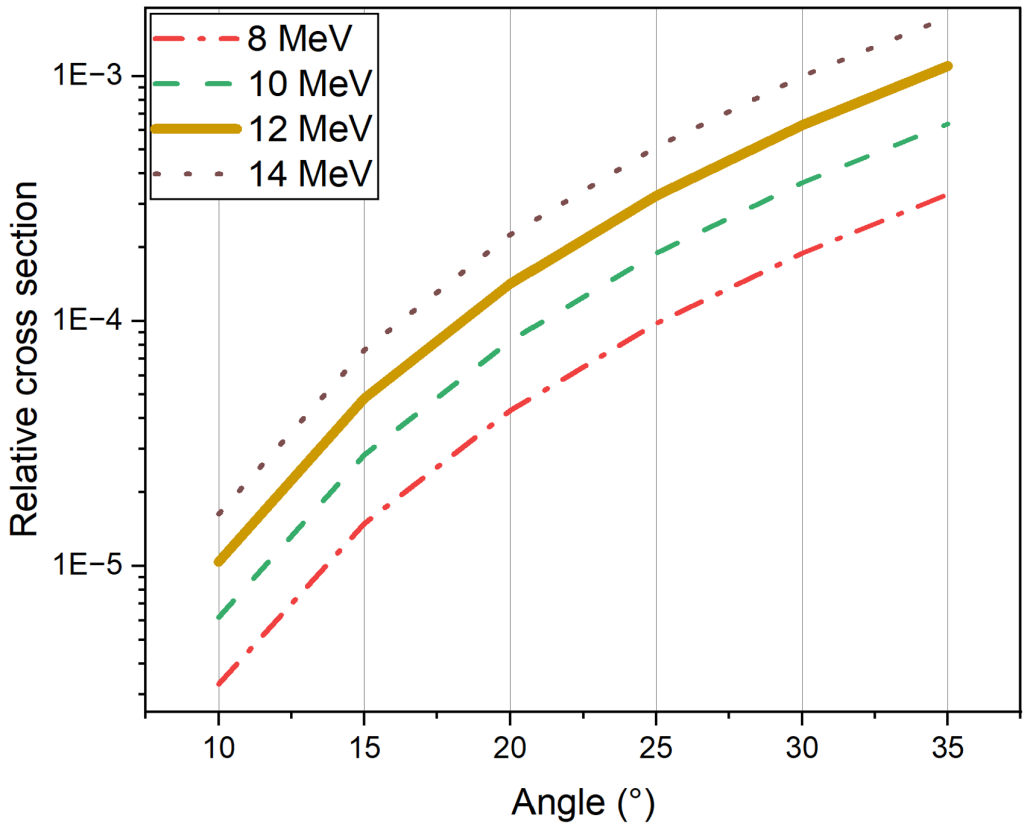

Figure 5.21: The relative cross section for the first excited state was calculated using GOSIA.

Position resolution

The position resolution is defined as the smallest time difference that can be measured [36]. A theoretical position resolution reported by [35] for a similar wire ranges from 20 to 80 keV, depending on the type of particle. However, because of the finite thickness of the target, which impedes on the position resolution, is the real position resolution higher than the theoretical value. The position wire in LIon has a position resolution of approximately around a FWHM of 7 ns.

A higher resolution would enhance the identification of closely spaced energy states. For instance, the 86 keV level, despite having a lower excitation probability, increases the number of detected counts for excited states that are near the level of interest. According to the GOSIA estimates, the second excited state would add approximately one-tenth of a count to the first excited state's total count. This complicates the analysis even further. There are several suggestions for improving the intrinsic position resolution of the position wire.

One potential solution is to increase the density of isobutane gas. The initial gas density was selected to provide sufficient position resolution for distinguishing ions of varying masses [36]. However, this application is not relevant. Higher gas density enhances ionization, resulting in a stronger signal for the position wire and potentially better resolution. Especially, since the GEANT4 simulation indicates only 300 keV energy deposition in the whole gas volume. Another important relationship, shown in Fig. 5.22, is the connection between gas pressure and the voltage in the position wires.

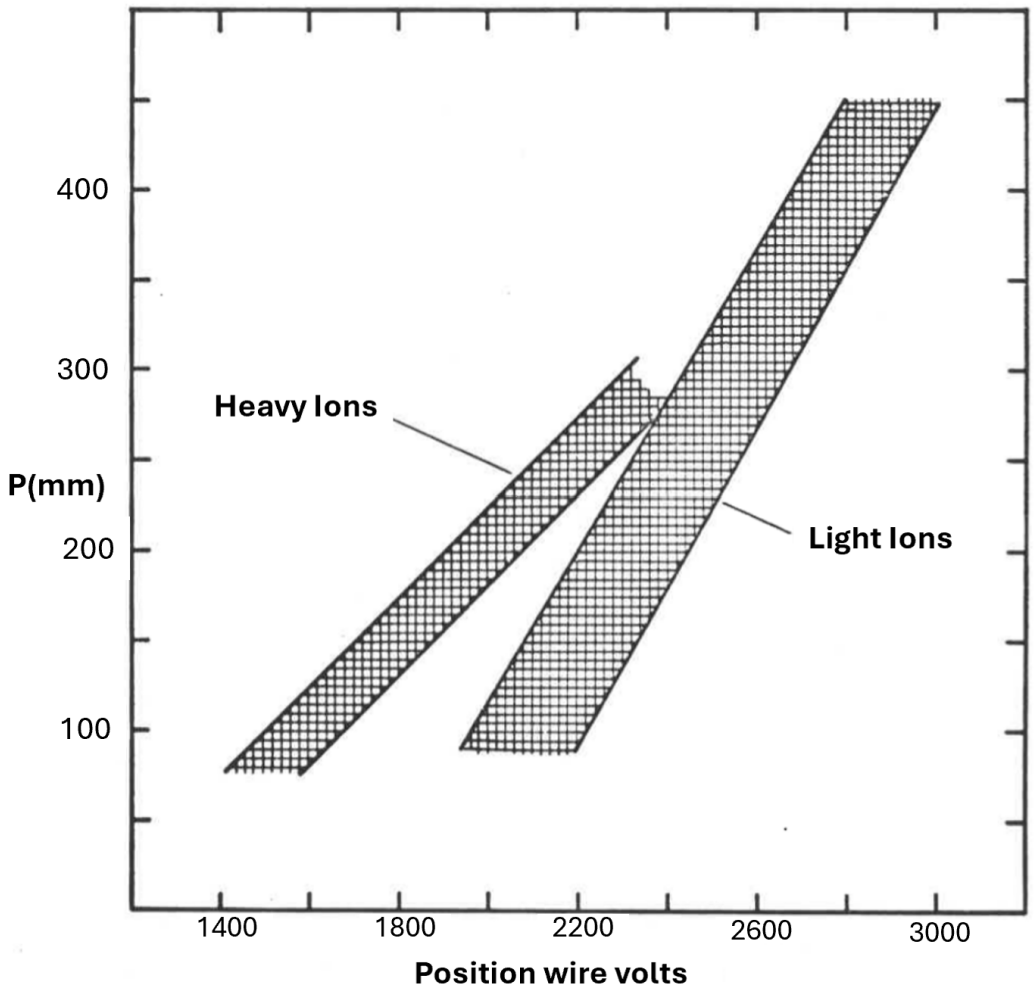

Figure 5.22: The gas pressure in the detector affects the possible volts in the position wires [36].

Thus, a higher voltage is possible by choosing a higher gas density. In addition, according to Eq. 3.1, equals a higher voltage in a higher position resolution. Although a consequence of this approach is that the Bragg peak will be shortened, however, this wouldn't impact protons with energies above 3 MeV.

A significant factor limiting the experimental resolution is the considerable tail observed in the elastic scattering spectra. This tail is primarily caused by energy straggling of the particles of interest, which can occur within the target material. It is important to note that neither the Enge spectrograph nor the detector contributes to this energy straggling, as they operate in a vacuum.

In this experiment, the target has a thickness of 0.5 μg/cm^2. Although this is considered a thin target, its thickness still complicates the analysis. As protons, the particles of interest, strike the target, they undergo predominantly elastic scattering. Due to the target's thickness, these protons interact with multiple target atoms before exiting. Consequently, a single proton experiences several scattering events rather than just one. This multiple scattering results in significant energy loss and broadening of the proton energy distribution before the particles enter the Enge spectrograph, ultimately affecting the accuracy of the measured energy.

Despite these challenges, the detector's position wire achieved a Full Width Half Maximum (FWHM) of 6.7, one of the best values reported for the LIon system. However, the small energy separation between the ground state and the 60 keV level causes overlapping spectra, which limits the experiment's resolving power. To improve spatial resolution and eliminate this overlap, several approaches can be considered, one of which is to use lower energies.

The incomplete data set from the LIon beam run leaves unanswered questions about the sensitivity to lower beam energies. Lower energies increase energy deposition within the gas, boosting the signal strength in the position wire, but also decrease the probability of excitation. Reexamining the gyroradius equation, Eq. 5.3, both the mass and charge remain constant, allowing for simplification of the equation.

$$\rho = \frac{\sqrt{E_p}}{B}, \tag{5.7}$$

the relationship between proton energy and magnetic field strength is quadratic. A lower proton energy necessitates a weaker magnetic field strength to maintain focus on the focal plane. However, since the gyroradius is proportional to the square root of proton energy, a decrease in proton energy results in a larger gyroradius. This increase in gyroradius will cause the elastic scattering peak and the 60 keV level to become more widely spaced.

Additionally, lower energy may cause less energy straggling. Lower energies lead to lower excitation probabilities in the target. It is speculated that a lower probability of excited states results in less energy straggling, as more of the beam would elastically scatter. This could further help sharpen the resolution. However, the excitation probability for the level of interest would even be lower.

If these suggestions do not help, a final solution is gamma spectroscopy, which offers significantly higher energy resolution on the order of a few keV [52]. Particle spectroscopy was chosen for this experiment for many discussed reasons.

In particle spectroscopy, a particle is directed at a target, causing an energy loss characteristic of the excitation reaction, and the same particle is measured afterwards. In contrast, gamma spectroscopy involves measuring the gamma rays emitted during the de-excitation of the isomer after the particle strikes the target. This method is more complex, requiring multiple corrections for the gamma rays. For example, when the isomer is excited, the impulse from the incoming particle causes the isomer's nucleus to move, necessitating a correction for this movement.

Previous research by [6] describes gamma spectroscopy with CAESER, which failed for different reasons. The large data set, due to the high excitation of ^{16}O, was too vast, and the required corrections made it impossible to achieve a correct fit with GOSIA. Possibly, would a lower beam energy, and particle mass ensure a successful ending. Do note that CAESER, at HIAF, only allows backwards scattering which complexes the search again to the 60 keV state.

Chapter 6

Conclusions

This work assessed low-energy Coulomb excitation to verify the validity of Coulomb excitation at low energies. Theoretical modeling was conducted with GOSIA and GEANT4. HIAF's 14 UD 15 MV focused protons at a ^{155}Gd target to gain experimental spectra. The goal was to validate low-energy Coulomb excitation for isomer-power research.

Theoretical modeling was conducted to achieve a deeper understanding of LIon and low-energy Coulomb excitation. The semi-classical code GOSIA was utilized to investigate the probabilities of excited states. Additionally, GEANT4, a Monte Carlo toolkit created by CERN, was employed to simulate the interaction of particles with matter. A model of the detector incorporating real-life geometries was developed and rigorously benchmarked multiple times.

To conduct particle spectroscopy, 12 MeV protons were directed at a ^{155}Gd target at various scattering angles. The elastic and inelastic scattered protons were focused using an Enge spectrometer onto the focal plane of LIon. This detector employs its second position wire and scintillator to measure the particles of interest. Scattering angles of 20°, 25°, and 30° were utilized during the experiment.

GOSIA demonstrated that the probability of exciting the level of interest, specifically the first excited state, is low. For a proton with an energy of 12 MeV and a scattering angle of 25°, the probability of exciting the 60 keV level is 1.62×10^{-4}. Furthermore, the high density of excited states may complicate the analysis even more.

The GEANT4 simulation model underwent benchmarking on three occasions: once with data from a run conducted nearly a year ago, another with a triple alpha source, and a third during the Coulomb-excitation run. The first two benchmarks showed great similarity. A comparison between the simulated spectra and the experimental spectra in the final benchmark revealed significant discrepancies, particularly in the shape of the inelastic peaks. These differences were attributed to several factors, including experimental contamination, incomplete modeling of energy levels, and the absence of energy-dependent cross sections in the GEANT4 framework.

The goal of the experiment was to determine the number of counts in the first excited state. However, despite optimizing the experimental parameters, the count rate for the state of interest was still inadequate. The small energy separation between the states resulted in overlapping spectra, complicating the analysis. The experiment encountered two main challenges: the low probability of exciting the 60 keV state and limited positional resolution.

Strategies for improvement were identified and categorized to enhance the excitation probability of the 60 keV state and to improve position resolution. The atomic mass and atomic number significantly influence the excitation probability. Therefore, a deuteron would lead to a higher excitation probability. Additionally, a higher density of isobutane gas could increase the excitation probability by enhancing signal strength.

An increase in excitation probability would still require an improvement in the position resolution of the position wire to accurately identify the peak of interest. The position resolution is compromised due to low-energy tails resulting from straggling in intense elastic scattering events, the presence of contaminants, and a high density of levels, which further complicates the spectrum. The thickness of the target contributes to straggling, leading to broad shoulders in the elastic scattering. Considering a thinner target could help alleviate this issue. Additionally, exploring lower beam energies may enhance the position resolution.

It is important to note that each suggestion presents a new trade-off. Employing gamma spectroscopy may be necessary due to its superior energy resolution. However, particle spectroscopy is more straightforward, while gamma spectroscopy requires several corrections.

In conclusion, this study contributes to isomer-power research by attempting low-energy Coulomb excitation using 12 MeV protons on a ^{155}Gd target at various scattering angles. Data analysis was supported by GOSIA and GEANT4 modeling, which provided a thorough understanding of the project. While LIon achieved its best full width at half maximum (FWHM) for position resolution, the energy resolution and low counting probabilities hindered the extraction of counts from the peak of interest. This extraction is crucial for determining the matrix elements using GOSIA; therefore, the experiment was unsuccessful. Improved position resolution could potentially be attained by using thinner targets and operating at lower beam energies. Furthermore, gamma spectroscopy remains a viable alternative to particle spectroscopy.

Bibliography

[1] C. Wang, C. Yang, and Z. Zheng, "Toward practical high-energy and high-power lithium battery anodes: Present and future," *Advanced Science*, vol. 9, p. 2 105 213, Mar. 2022.

[2] O. L. Ayodele, K. O. Sanusi, and M. T. Kahn, "Nuclear battery: A source of environmentally friendly energy," *Journal of Engineering, Design and Technology*, vol. 17, pp. 172–182, Jan. 2019.

[3] A. K. Jain, B. Maheshwari, and A. Goel, *Nuclear Isomers: A Primer*. Cham: Springer International Publishing, 2021.

[4] M. Rocchini and M. Zielinska, "Low-Energy Coulomb Excitation for the Shell Model," *Physics*, pp. 1237–1253, Dec. 2021.

[5] M. A. Prelas, C. L. Weaver, M. L. Watermann, *et al.*, "A review of nuclear batteries," *Progress in Nuclear Energy*, vol. 75, pp. 117–148, Aug. 2014, ISSN: 01491970. DOI: 10.1016/j.pnucene.2014.04.007. [Online]. Available: https://linkinghub.elsevier.com/retrieve/pii/S0149197014000961 (visited on 09/14/2024).

[6] R. Leonard, "Low-energy coulomb excitation of ^{155}gd," MSc thesis, Australian National University, Nov. 2024, p. 69.

[7] M. Zielińska, L. P. Gaffney, K. Wrzosek-Lipska, *et al.*, "Analysis methods of safe Coulomb-excitation experiments with radioactive ion beams using the GOSIA code," *The European Physical Journal A*, vol. 52, no. 4, p. 99, Apr. 2016, ISSN: 1434-6001, 1434-601X. DOI: 10.1140/epja/i2016-16099-8. [Online]. Available: http://link.springer.com/10.1140/epja/i2016-16099-8 (visited on 10/12/2024).

[8] D. Cline, T. Czosnyka, A. B. Hayes, *et al.*, *Gosia user manual for simulation and analysis of coulomb excitation experiments*, Accessed: 2025-06-16, GOSIA Users Steering Committee, Mar. 2012. [Online]. Available: https://www.pas.rochester.edu/~cline/Gosia/Gosia_Manual_20120309.pdf.

[9] A. B. Hayes, D. Cline, K. J. Moody, *et al.*, "Coulomb excitation of the 242m Am isomer," *Laser Physics*, vol. 17, no. 5, pp. 745–750, May 2007, ISSN: 1054-660X, 1555-6611. DOI: 10.1134/S1054660X07050222. [Online]. Available: http://link.springer.com/10.1134/S1054660X07050222 (visited on 09/30/2024).

[10] S. Agostinelli, J. Allison, K. Amako, *et al.*, "Geant4—a simulation toolkit," *Nuclear Instruments and Methods in Physics Research Section A: Accelerators, Spectrometers, Detectors and Associated Equipment*, vol. 506, no. 3, pp. 250–303, Jul. 2003, ISSN: 01689002. DOI: 10.1016/S0168-9002(03)01368-8. [Online]. Available: https://linkinghub.elsevier.com/retrieve/pii/S0168900203013688 (visited on 10/04/2024).

[11] B. Martin, *Nuclear and Particle Physics: An Introduction*. London: Wiley, 2006.

[12] J. Liley, *Nuclear Physics: Principles and Applications*. Wiley, 2001.

[13] K. S. Krane, *Introductory Nuclear Physics*. New York: Wiley, 1987, ISBN: 978-0471805533.

[14] P. Walker, "Nuclear Isomers," in *Handbook of Nuclear Physics*, Singapore: Springer Nature Singapore, 2023, pp. 487–523, ISBN: 978-981-19-6344-5 978-981-19-6345-2. DOI: 10.1007/978-981-19-6345-2_46. [Online]. Available: https://link.springer.com/10.1007/978-981-19-6345-2_46 (visited on 09/17/2024).

[15] P. Walker and Z. Podolyák, "A century of nuclear isomers," *Physics World*, vol. 34, no. 4, pp. 29–32, Jun. 2021, ISSN: 0953-8585, 2058-7058. DOI: 10.1088/2058-7058/34/04/28. [Online]. Available: https://iopscience.iop.org/article/10.1088/2058-7058/34/04/28 (visited on 09/13/2024).

[16] D. Rhodes, B. A. Brown, J. Henderson, *et al.*, "Exploring the role of high- j configurations in collective observables through the Coulomb excitation of Cd 106," *Physical Review C*, vol. 103, no. 5, p. L051301, May 2021, ISSN: 2469-9985, 2469-9993. DOI: 10.1103/PhysRevC.103.L051301. [Online]. Available: https://link.aps.org/doi/10.1103/PhysRevC.103.L051301 (visited on 10/24/2024).

[17] M. Lewitowicz, B. Blank, J. Daugas, *et al.*, "Nuclear structure studies by means of short-lived isomers at intermediate energies," *Nuclear Physics A*, vol. 682, no. 1-4, pp. 175–182, Feb. 2001, Publisher: Elsevier BV, ISSN: 0375-9474. DOI: 10.1016/s0375-9474(00)00637-0. [Online]. Available: https://linkinghub.elsevier.com/retrieve/pii/S0375947400006370 (visited on 09/17/2024).

[18] R. Bengtsson and H. Sagawa, "NUCLEAR SHAPE ISOMERS," *Atomic Data and Nuclear Data Tables*, no. 10, pp. 149–300, Sep. 2010.

[19] G. D. Dracoulis, "Isomers, nuclear structure and spectroscopy," *Physica Scripta*, vol. T152, p. 014 015, Jan. 2013, ISSN: 0031-8949, 1402-4896. DOI: 10.1088/0031-8949/2013/T152/014015. [Online]. Available: https://iopscience.iop.org/article/10.1088/0031-8949/2013/T152/014015 (visited on 09/24/2024).

[20] C. J. Chiara, J. J. Carroll, M. P. Carpenter, *et al.*, "Isomer depletion as experimental evidence of nuclear excitation by electron capture," *Nature*, vol. 554, no. 7691, pp. 216–218, Feb. 2018, ISSN: 1476-4687. DOI: 10.1038/nature25483.

[21] I. Stefanescu, G. Georgiev, F. Ames, *et al.*, "Coulomb Excitation of Cu 68 , 70 : First Use of Postaccelerated Isomeric Beams," *Physical Review Letters*, vol. 98, no. 12, p. 122 701, Mar. 2007, ISSN: 0031-9007, 1079-7114. DOI: 10.1103/PhysRevLett.98.122701. [Online]. Available: https://link.aps.org/doi/10.1103/PhysRevLett.98.122701 (visited on 10/11/2024).

[22] A. Hill, *Sub-barrier coulomb excitation of* ^{112,116,120}*sn*, https://nssc.berkeley.edu/wp-content/uploads/2022/04/01_Ava-Hill.pptx-1.pdf, Presentation slides, NSSC3 Kickoff & Advisory Board Meeting, Michigan State University. Accessed: 2025-02-13, Apr. 2022.

[23] S. M. Lenzi and D. Cortina-Gil, *The Euroschool on Exotic Beams, Vol. VI* (Lecture Notes in Physics). Cham: Springer International Publishing, 2022, vol. 1005, ISBN: 978-3-031-10750-4 978-3-031-10751-1. DOI: 10.1007/978-3-031-10751-1. [Online]. Available: https://link.springer.com/10.1007/978-3-031-10751-1 (visited on 10/27/2024).

[24] P. F. Brown, C. Baktash, J. O'Brien, *et al.*, "B (E 2) values in Gd 155 , Dy 161 , Dy 163 , Er 167 , and Lu 175," *Physical Review C*, vol. 18, no. 2, pp. 666–670,

Aug. 1978, ISSN: 0556-2813. DOI: 10.1103/PhysRevC.18.666. [Online]. Available: https://link.aps.org/doi/10.1103/PhysRevC.18.666 (visited on 04/23/2025).

[25] E. Clément, M. Zielińska, S. Péru, *et al.*, "Low-energy Coulomb excitation of Sr 96 , 98 beams," *Physical Review C*, vol. 94, no. 5, p. 054 326, Nov. 2016, ISSN: 2469-9985, 2469-9993. DOI: 10.1103/PhysRevC.94.054326. [Online]. Available: https://link.aps.org/doi/10.1103/PhysRevC.94.054326 (visited on 10/27/2024).

[26] M. Goyal, R. Kumar, P. Singh, *et al.*, "Effect of nuclear surface diffuseness on Coulomb excitation and total nuclear reaction cross sections," *Nuclear Physics A*, vol. 992, p. 121 620, Dec. 2019, ISSN: 03759474. DOI: 10.1016/j.nuclphysa.2019.121620. [Online]. Available: https://linkinghub.elsevier.com/retrieve/pii/S0375947419301952 (visited on 10/24/2024).

[27] G. Immè, D. Morelli, M. Aranzulla, *et al.*, "Nuclear track detector characterization for alpha-particle spectroscopy," *Radiation Measurements*, vol. 50, pp. 253–257, Mar. 2013, ISSN: 13504487. DOI: 10.1016/j.radmeas.2012.03.014. [Online]. Available: https://linkinghub.elsevier.com/retrieve/pii/S135044871200090X (visited on 05/30/2025).

[28] M. Pomorski, M. Pfützner, W. Dominik, *et al.*, "Proton spectroscopy of Ni 48 , Fe 46 , and Cr 44," *Physical Review C*, vol. 90, no. 1, p. 014 311, Jul. 2014, ISSN: 0556-2813, 1089-490X. DOI: 10.1103/PhysRevC.90.014311. [Online]. Available: https://link.aps.org/doi/10.1103/PhysRevC.90.014311 (visited on 05/30/2025).

[29] N. Nica, *Adopted levels for ^{155}gd*, https://www.nndc.bnl.gov/ensdf/EnsdfDispatcherServlet, Evaluated Nuclear Structure Data File (ENSDF), NNDC, Brookhaven National Laboratory. Accessed: 2025-06-16, 2019.

[30] P. E. Garrett, M. Zielińska, A. Bergmaier, *et al.*, "Coulomb excitation of Ru 102 with C 12 and O 16," *Physical Review C*, vol. 106, no. 6, p. 064 307, Dec. 2022, ISSN: 2469-9985, 2469-9993. DOI: 10.1103/PhysRevC.106.064307. [Online]. Available: https://link.aps.org/doi/10.1103/PhysRevC.106.064307 (visited on 05/10/2025).

[31] N. P. Heydenburg and G. M. Temmer, "Coulomb Excitation and Cascade Decay of Rotational States in Odd-Mass Nuclei," *Physical Review*, vol. 104, no. 4, pp. 981–989, Nov. 1956, ISSN: 0031-899X. DOI: 10.1103/PhysRev.104.981. [Online]. Available: https://link.aps.org/doi/10.1103/PhysRev.104.981 (visited on 04/23/2025).

[32] U. Kneissl, H. Pitz, and A. Zilges, "Investigation of nuclear structure by resonance fluorescence scattering," *Progress in Particle and Nuclear Physics*, vol. 37, pp. 349–433, 1996, ISSN: 01466410. DOI: 10.1016/0146-6410(96)00055-5. [Online]. Available: https://linkinghub.elsevier.com/retrieve/pii/0146641096000555 (visited on 04/24/2025).

[33] A. Stuchbery, G. Lampard, and H. Bolotin, "Spectroscopy of 155Gd following Coulomb excitation: Signature-independent M1 properties and evidence for octupole correlations," *Nuclear Physics A*, vol. 642, no. 3-4, pp. 361–386, Nov. 1998, ISSN: 03759474. DOI: 10.1016/S0375-9474(98)00540-5. [Online]. Available: https://linkinghub.elsevier.com/retrieve/pii/S0375947498005405 (visited on 02/12/2025).

[34] D. T. Doherty, J. M. Allmond, R. V. F. Janssens, *et al.*, "Triaxiality near the 110Ru ground state from Coulomb excitation," *Physics Letters B*, vol. 766, no. C, pp. 334–338, 2017, ISSN: 0370-2693. DOI: 10.1016/j.physletb.2017.01.031.

[35] A. J. Mitchell, "Investigating high-j single-particle energies in z = 51 nuclei," PhD thesis, University of Manchester, Manchester, Jan. 2012.

[36] T. Ophel and A. Johnston, *The enge spectrograph and focal-plane detector system*, Australian National University (ANU), 1977.

[37] P. P. Calò, F. Ciciriello, S. Petrignani, *et al.*, "SiPM readout electronics," *Nuclear Instruments and Methods in Physics Research Section A: Accelerators, Spectrometers, Detectors and Associated Equipment*, vol. 926, pp. 57–68, May 2019, ISSN: 01689002. DOI: 10.1016/j.nima.2018.09.030. [Online]. Available: https://linkinghub.elsevier.com/retrieve/pii/S0168900218311756 (visited on 04/21/2025).

[38] "Bc400, bc404, bc408, bc412, bc416 — luxium solutions," Luxium Solutions, Tech. Rep., Jun. 2023, Accessed: 2025-05-05. [Online]. Available: https://www.luxiumsolutions.com/sites/default/files/2023-08/146337_Luxium_SGC%20BC400%20404%20408%20412%20416_FIN.pdf.

[39] I. Antcheva, M. Ballintijn, B. Bellenot, *et al.*, "ROOT — A C++ framework for petabyte data storage, statistical analysis and visualization," *Computer Physics Communications*, vol. 180, no. 12, pp. 2499–2512, Dec. 2009, ISSN: 00104655. DOI: 10.1016/j.cpc.2009.08.005. [Online]. Available: https://linkinghub.elsevier.com/retrieve/pii/S0010465509002550 (visited on 10/04/2024).

[40] J. F. Ziegler, J. P. Biersack, and M. D. Ziegler, *Srim – the stopping and range of ions in matter*, https://www.srim.org/, Accessed: 2025-06-16, Apr. 2024.

[41] E. J. N. Wilson, *An Introduction to Particle Accelerators*. Oxford: Proceedings of Science, 2009, ISBN: 978-0198508298.

[42] P. Surendran, A. Shrivastava, A. K. Gupta, *et al.*, "Accelerator mass spectrometry programme and related developments at the BARC–TIFR Pelletron accelerator," *Nuclear Instruments and Methods in Physics Research Section B: Beam Interactions with Materials and Atoms*, vol. 267, no. 7, pp. 1171–1174, Apr. 2009, ISSN: 0168-583X. DOI: 10.1016/j.nimb.2009.01.135. [Online]. Available: https://www.sciencedirect.com/science/article/pii/S0168583X09002109 (visited on 04/21/2025).

[43] E. Wilson and B. J. Holzer, "Accelerators, Colliders and Their Application," in *Particle Physics Reference Library*, S. Myers and H. Schopper, Eds., Cham: Springer International Publishing, 2020, pp. 1–14, ISBN: 978-3-030-34244-9 978-3-030-34245-6. DOI: 10.1007/978-3-030-34245-6_1. [Online]. Available: http://link.springer.com/10.1007/978-3-030-34245-6_1 (visited on 11/15/2024).

[44] L. Lamm, "Accelerator at notre dame," PowerPoint presentation, University of Notre Dame, March 2009, Mar. 2009.

[45] E. Simpson, *Nuclide chart*, https://people.physics.anu.edu.au/~ecs103/chart/, Accessed: 2025-03-28. Australian National University. Putting the joy back into nuclear data., n.d.

[46] *Material composition of gd-155*, https://pubchem.ncbi.nlm.nih.gov/compound/Gadolinium-155, Accessed: 2025-03-28. National Center for Biotechnology Information (2025).

[47] S. Carmichael, P. O'Malley, D. Bardayan, *et al.*, "The Enge Split-Pole Spectrograph at the University of Notre Dame," *EPJ Web of Conferences*, vol. 304, A. Pakou, G. Souliotis, and C. Moustakidis, Eds., p. 02 002, 2024, ISSN: 2100-014X. DOI: 10.1051/epjconf/202430402002. [Online]. Available: https://www.epj-conferences.org/10.1051/epjconf/202430402002 (visited on 10/12/2024).

[48] *Pixie-16 user manual*, Accessed: 2025-03-29, XIA LLC, Dec. 2018. [Online]. Available: https://docs.frib.msu.edu/daq/newsite/pixie16/Pixie16_UserManual.pdf.

[49] *Anu pixie16 data acquisition system user guide*, Accessed: 2025-03-29, Australian National University (ANU), Jul. 2021.

[50] L. A. Riley, I. C. S. Hay, L. T. Baby, *et al.*, "Fe 54 (d , p) Fe 55 and the evolution of single neutron energies in the N = 29 isotones," *Physical Review C*, vol. 106, no. 6, p. 064 308, Dec. 2022, ISSN: 2469-9985, 2469-9993. DOI: 10.1103/PhysRevC.106.064308. [Online]. Available: https://link.aps.org/doi/10.1103/PhysRevC.106.064308 (visited on 06/12/2025).

[51] "Canberra Model 2210 Timing Filter Amplifier Instruction Manual," Canberra Industries, Tech. Rep., 2002.

[52] T. N. Perissinotto, "Investigating two-phonon γ-vibrational states in ^{162}dy," Honours thesis, Australian National University, Oct. 2024.

[53] Grammarly Inc., *Grammarly*, https://www.grammarly.com/, Accessed: 2025-06-15, 2025.